



# CVD diamond applications for particle detection and identification in high-radiation environments

Matevž Červ  
Vienna University of Technology

A thesis submitted for the degree of  
*Doctor of technical sciences*

Geneva 2016



# Contents

<b>1</b>	<b>Introduction</b>	<b>1</b>
1.1	Fundamental research . . . . .	2
1.2	Research institutes . . . . .	3
1.3	The Large Hadron Collider . . . . .	5
1.4	The ATLAS experiment . . . . .	7
1.5	Particle detectors . . . . .	8
<b>2</b>	<b>Diamond detectors for radiation detection</b>	<b>11</b>
2.1	Semiconductor detectors . . . . .	12
2.2	Principles of signal formation in semiconductors . . . . .	14
2.3	Carrier transport in a diamond sensor . . . . .	17
2.4	Radiation-induced current signals . . . . .	19
2.5	Radiation damage . . . . .	24
2.6	Temperature effects . . . . .	26
2.7	Electronics for signal processing . . . . .	26
<b>3</b>	<b>Diamond irradiation study</b>	<b>33</b>
3.1	Measurement setup . . . . .	34
3.2	Charged particle pulses and spectra . . . . .	40
3.3	Radiation limitations . . . . .	42
3.4	Temperature limitations . . . . .	52
3.5	Conclusion . . . . .	59
<b>4</b>	<b>Charge monitoring</b>	
	<i>The ATLAS Diamond Beam Monitor</i>	<b>61</b>
4.1	Luminosity measurements . . . . .	62
4.2	Diamond pixel module . . . . .	63
4.3	Module assembly . . . . .	66
4.4	Performance results . . . . .	67
4.5	Installation and commissioning . . . . .	73
4.6	Operation . . . . .	75
4.7	Conclusion . . . . .	78

## *CONTENTS*

---

### **5 Current monitoring**

<i>Real-time particle identification</i>	<b>79</b>
5.1 Motivation . . . . .	80
5.2 Requirements . . . . .	80
5.3 Device specifications . . . . .	81
5.4 Pulse parameters . . . . .	81
5.5 Applications . . . . .	82
5.6 Description of the firmware . . . . .	83
5.7 Control and data interface . . . . .	89
5.8 Performance results . . . . .	91
5.9 Source calibration . . . . .	95
5.10 Applications in neutron instrumentation . . . . .	106
5.11 Conclusion . . . . .	115
<b>Bibliography</b>	<b>117</b>

# Chapter 1

## Introduction

Curiosity is the driving force behind the development of human civilisation. Over centuries, scientists have discovered new methods for understanding Nature and the fundamental mechanisms governing the Universe, using continually improving research methods and technology to peer ever deeper into the heart of matter.

After the initial discovery of atoms, their underlying structure was soon revealed to be that of a positively charged core surrounded by a cloud of orbiting electrons. The atomic nucleus was subsequently decomposed into protons and neutrons, which themselves were found to consist of three tiny quarks. Studying these minuscule building blocks of visible matter has made it possible to understand more about the intricate complexities of the Universe, and the mechanisms that guide its behaviour and evolution.

Discoveries of this magnitude would not have been possible without the technologies developed to carry out such experiments. On one hand, the energy of the experimental devices has been increasing continually, allowing smaller and smaller distance scales to be probed. On the other hand, the devices used to observe and measure the phenomena created in these experiments have had to be designed with improved precision, speed and durability.

Keeping these factors in mind, the goal of this work was to find “the perfect material”. Diamond proved to be a worthy contender, offering both outstanding electrical and mechanical properties which make it the material of choice for a number of applications in experimental physics. However, much remains to be learned about its behaviour, and this thesis adds a small piece to the shimmering mosaic of diamond research efforts.

The first chapter introduces some of the leading particle physics research institutes, and describes how their research is carried out. The second chapter discusses the properties of diamond detectors used in high energy particle physics experiments. A diamond sensor irradiation study is presented in chapter 3. The conclusions of this study, which define the constraints for the two diamond detector applications, are presented in the final two chapters.

## 1.1. FUNDAMENTAL RESEARCH

---

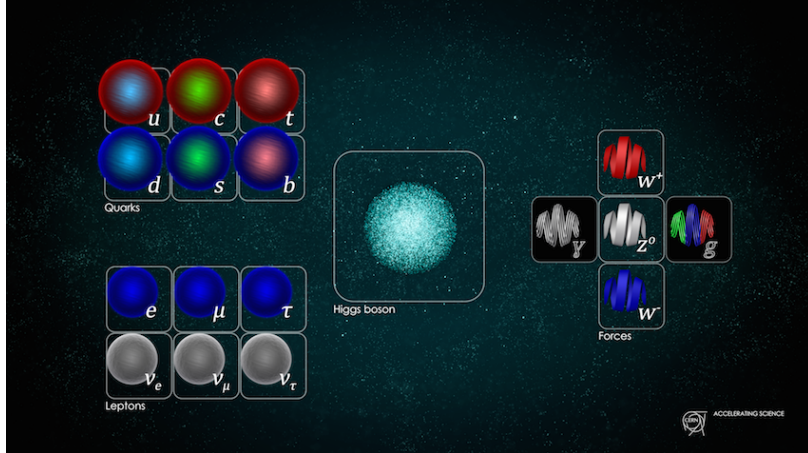


Figure 1.1: The Standard model [2].

### 1.1 Fundamental research

The aim of fundamental research is to define scientific theories and verify them to improve our understanding of the universe. It does not in itself focus on applying this research by developing products and is not meant to create a direct return on investment. Instead, it expands the overall knowledge of the human kind - by making the results freely available to the general public.

Particle physics research peers into the smallest constituents of the universe, dissecting the atoms into quarks and electrons, catching cosmic rays and figuring out what dark matter is made of. Particle physicists want to explain the phenomena surrounding us by studying the fundamental particles and the mechanisms governing their interactions. By understanding this, we would be able to answer difficult questions; How did the universe begin? What is the invisible force (dark matter, dark energy) pushing the galaxies apart from each other? Where does mass come from? Why is there almost no antimatter in the universe? In this effort, scientists have formed several theories. One of them, the Standard Model of particles, is currently the most successful theory to describe the constituents of matter and their interactions.

**The Standard Model (SM)** is a physics theory developed in the 1970's [1]. It was designed to explain the current experimental results. As such, it was also able to predict new discoveries and was a driving force for the scientists to invest time and money in developing new experiments. To date, it is by far the most established and verified physics theory. It explains how the basic building blocks of matter – *fermions* – interact with each other via mediators of interactions called *bosons*. There are two main families of fermions - *quarks* and *leptons*, as shown in figure 1.1. Each group consists of six members divided into three *generations*, the first being the lightest and most stable and the last the heaviest, which are the most unstable. The nature around us is made up of the stable particles – those from the second or third generations can only be found in cosmic rays or produced artificially

using particle accelerators.

Quarks have a spin of 1/2 and a charge of either +2/3 (up, charm, top) or -1/3 (down, strange, bottom) while the leptons have a spin of 1/2 and a charge of either 1 (electron, muon, tau) or 0 (electron neutrino, muon neutrino, tau neutrino). Leptons only exist individually – they do not cluster. Quarks, however, immediately form a cluster of either two (unstable), three (more stable) or five (unstable). Two up and one down quark make up a proton whereas two down and one up quark make up a neutron.

In addition to fermions, each particle has its corresponding antiparticle – a particle with the same mass but the opposite charge. If an antiparticle hits a particle, they annihilate each other, producing energy in form of photons.

Bosons are the carriers of force that mediate weak ( $W^+$ ,  $W^-$  and  $Z$  bosons), strong (gluons) and electromagnetic (photons) interactions. The weak interaction is responsible for the radioactive decay of subatomic particles, thus playing an essential role in nuclear fusion – a process taking place in the stars. The electromagnetic interaction works at a macroscopic level – it allows particles to interact via electric and magnetic fields. The strong interaction is effective at femtometer distances and it governs how quarks interact and bind with each other. An additional boson is the Higgs boson discovered at CERN in 2012 [3]. It is a representation of the Higgs mechanism, which gives rise to the mass (or lack thereof) of all the particles in the Standard Model.

## 1.2 Research institutes

This section gives a short overview of some of the institutes and collaborations carrying out fundamental physics research. These facilities were used for the research carried out for this thesis.

**CERN** (European Centre for Nuclear Research) [4] is the largest particle physics laboratory in the world, straddling the Swiss-French border just outside Geneva. It was established in 1954 to bring the war-torn Europe together by means of fundamental scientific research. Today, its 22 member state countries and several observer states contribute approximately 1 billion CHF annually to fund the research and development. More than 10000 scientists, engineers, technicians, students and others from all around the globe work at CERN on many projects in research fields ranging from particle to nuclear physics. The scope is to probe the fundamental structure of the universe and to understand the mechanisms governing it. Therefore CERN’s main function is to provide the infrastructure for high-energy physics experiments. These are carried out using large machines called particle accelerators. These instruments boost beams of particles to high energies before making them collide with each other or with stationary targets. The resulting collisions are recorded by particle detectors and later analysed by physicists. To carry out research on the smallest constituents of matter, their dynamics and structure, very high energies are needed. This

## 1.2. RESEARCH INSTITUTES

---

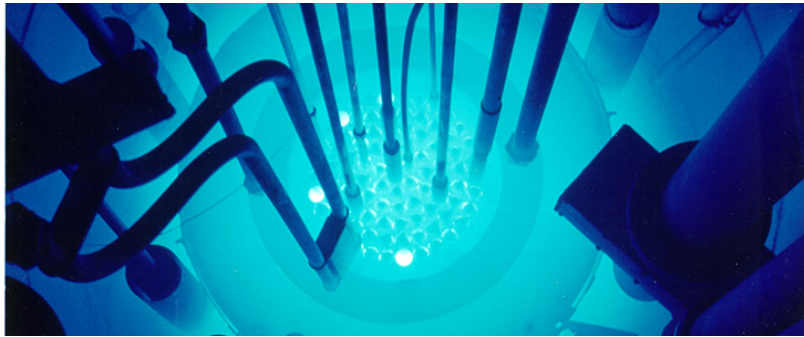


Figure 1.2: The TRIGA MARK II neutron reactor [9].

is why the most powerful accelerators are used for fundamental research. The largest accelerators at CERN are the Proton Synchrotron [5], the Super Proton Synchrotron [6] and the Large Hadron Collider, described in 1.3.

**Atominstytut, Vienna** (ATI) [7], an institute for atomic and subatomic physics, was established in 1958 in Vienna as an inter-university institute. It houses around 200 people involved in a broad range of research fields: quantum, particle, neutron, nuclear, radiation and reactor physics, quantum optics etc. As of 2002 the ATI is part of the University of Technology in Vienna.

Its central facility is *TRIGA MARK II* [8], a neutron reactor used for training, research and isotope production. It is one of 40 such reactors worldwide, produced by the Californian company General Atomic in the early 60's. It is capable of continuous operation at a maximum output power of 250 kW. The reactor core consists of 3 kg of 20 % enriched uranium ( $^{235}\text{U}$ ). The fuel moderator rods are mostly made up of zirconium with low percentage of hydrogen and uranium. Both the core and the rods are immersed in a pool of water as shown in figure 1.2 for the purpose of cooling and radiation protection. The surrounding concrete walls are 2 m wide with an added graphite layer for improved shielding. Four main experimental apertures for neutron beam are placed radially through the walls. All exits are heavily shielded to prevent the people from being exposed to radiation, but still leaving enough space to set up experiments. Apart from the beam apertures, there are several other exits and components, e.g. a thermal column for generation of thermal (low energetic) neutrons.

**n-ToF** (neutron Time-of-Flight) [10] is a scientific collaboration with the aim of studying neutron-nucleus interactions. Over 30 institutes are active members of this collaboration, among them Atominstytut in Vienna. The n-ToF experiment is located at CERN where the experiments are carried out in a 200 m long experimental area. The knowledge stemming from the experimental results can then be applied in various fields ranging from nuclear technology and cancer therapy to astrophysics.

A pulsed beam of highly energetic protons (20 GeV/c) is produced by the Proton Synchrotron (PS) and aimed at a fixed lead spallation target. Each proton hitting the target

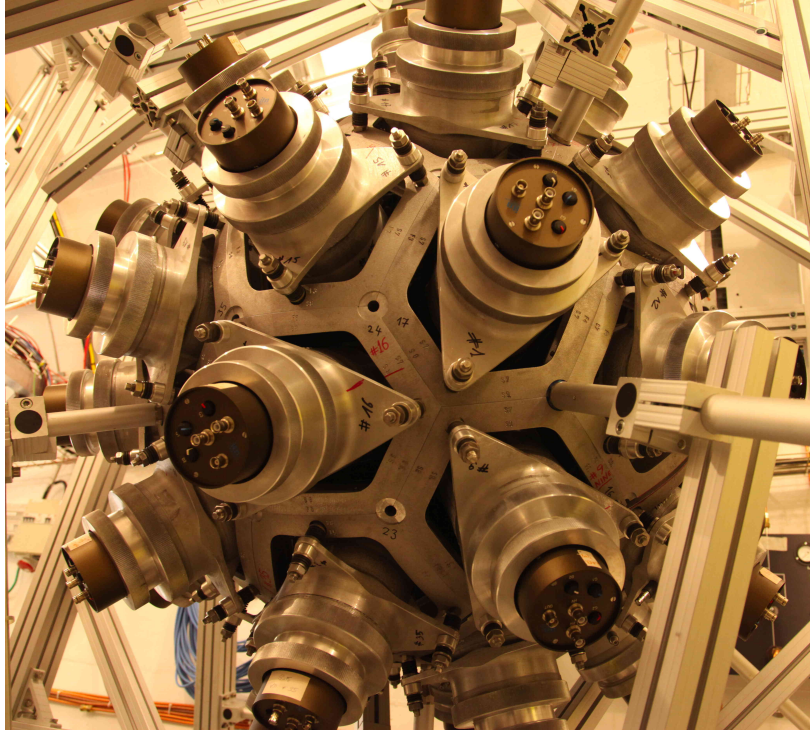


Figure 1.3: The calorimeter in the n-ToF area [11].

produces around 300 neutrons of various energies. Initially highly energetic neutrons are slowed down by the target and by a slab of water placed behind it. This broadens their energy spectrum, which then ranges from meV (thermal neutrons) to GeV (fast neutrons). The neutrons are then sent through a 185 m long evacuated pipe to the experimental area, where they collide with another target or a sample. The radiation created by the collisions is detected by a set of dedicated detectors around the interaction point, as shown in figure 1.3. Having different energies, neutrons travel with different speeds, highly energetic ones reaching the target faster than those with low energies. The analysis of collisions with a precise timing allows for a determination of the interaction probability with the sample material as a function of energy of the incident neutrons.

### 1.3 The Large Hadron Collider

A particle accelerator is a machine that accelerates beams of charged particles such as protons, electrons, ions etc. It generates electric fields that add kinetic energy to the particles, speeding them up. It then uses magnets to retain them within a defined trajectory and inside the evacuated beam pipe. The trajectory can be either linear (linear accelerators or LINACs) or circular (circular or cyclic accelerators). The former accelerate particles in a straight line, therefore the acceleration process only occurs once. The latter can accelerate particles many times while keeping them in orbit, but need a LINAC to pre-accelerate the particles before being injected in the loop.

### 1.3. THE LARGE HADRON COLLIDER

---

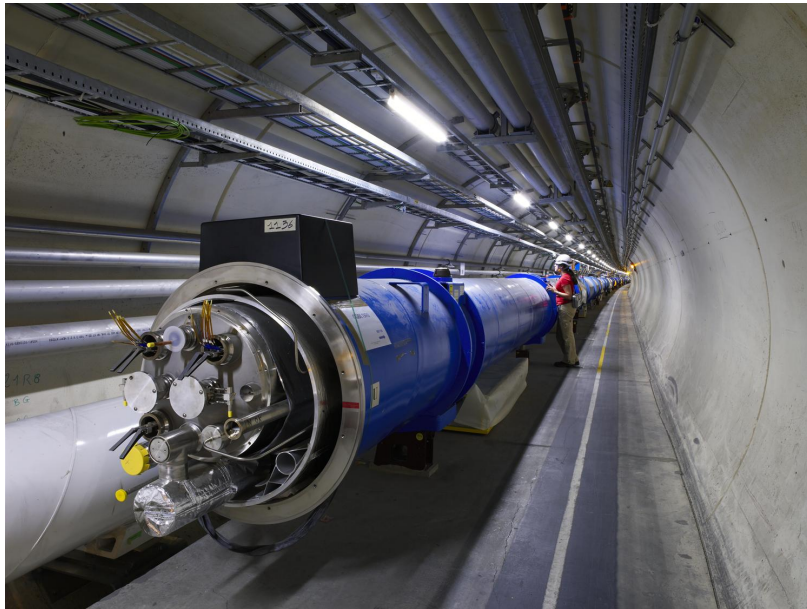


Figure 1.4: The Large Hadron Collider [12].

Particle accelerators are used in numerous fields ranging from fundamental and material research, cancer treatment to industrial applications, such as biomedicine and material processing. Several types of accelerators exist: electrostatic accelerators, LINACs, cyclotrons, synchrocyclotrons, synchrotrons, synchrotron radiation sources and fixed-field alternating gradient accelerators (FFAGs).

The Large Hadron Collider (LHC, figure 1.4) at CERN is the largest particle collider in the world. It was built between 1998 and 2008 and was first successfully started in 2010 and operated until 2013 when it underwent a two-year long upgrade. Its second operational cycle started at the beginning of 2015.

The LHC is a 27 km long circular machine set up in a tunnel deep under the surface, ranging from 50 to 175 m below ground. It accelerates two proton beams to the energy of 6.5 TeV per beam before it makes them collide with each other with the energy of 13 TeV at four different interaction points around its circumference. Hair-thin particle beams are guided inside two evacuated pipes with a  $\sim$ 5 cm radius by means of magnetic field. Coils made up of a superconductive material are wound around the pipes in special patterns. When cooled down to -271 °C using liquid helium, they become superconductive; the resistivity of the material drops significantly, minimising the heat dissipation despite high electric currents. These produce strong magnetic fields which bend the particles and keep them in a circular trajectory.

The protons travel bunched together in groups of  $10^{11}$  per bunch. These bunches are accelerated when traversing the radio-frequency (RF) cavities with the frequency of the electromagnetic field equal to 400 MHz. This oscillating field creates 2.5 ns long buckets – compartments for the bunches. Only one out of ten buckets is filled, so the bunches

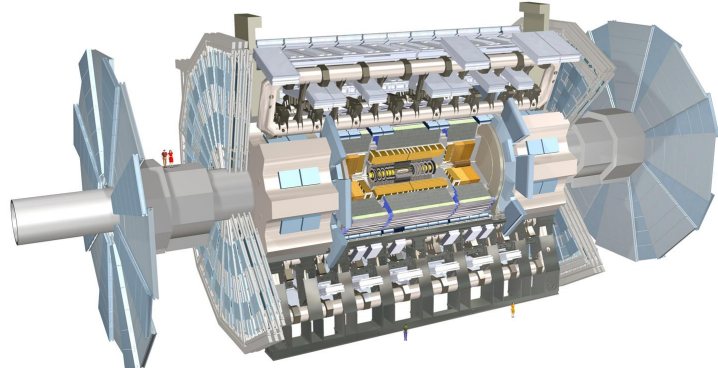


Figure 1.5: The ATLAS Experiment [16].

are spaced at 25 ns. This defines the machine’s clock (40 MHz) as well as the maximum rate of collisions - the bunches travelling in the opposite direction cross at the intersections 40 million times per second. Around 20 collisions occur during every bunch crossing, yielding the maximum collision rate of the order of  $10^9 \text{ s}^{-1}$ . The number of collisions will increase in the following years; the number of particles per bunch will be increased and the transverse spread of the bunches will be decreased. The bunch density will therefore be increased, which will in turn increase the collision probability – the cross-section. The original design number of collisions accumulated over the years of operation is presented in the form of integrated luminosity [13] and is of the order of  $300 \text{ fb}^{-1}$  (inverse femtobarn). After the planned upgrades in 2020, the High-Luminosity LHC [14] will achieve up to  $3000 \text{ fb}^{-1}$ .

## 1.4 The ATLAS experiment

ATLAS (short for A Toroidal Lhc ApparatuS, figure 1.5) [15] is a particle physics experiment at CERN. Its purpose is to verify current theories and to search for new discoveries by observing and analysing high energy proton-proton collisions produced by the LHC. It is the biggest experiment at CERN by dimensions (45 m in length and 26 m in height) and the number of people involved (more than 3000 physicists and engineers). The ATLAS experiment consists of a number of detectors, each designed to measure a specific property of the particles and photons produced during the collision. The closest to the collision point is the Inner Detector (ID), which consists of scintillating elements, a Transition Radiation Tracker and of the several layers of highly spatially segmented semiconductor sensors, which record single points of the incident particles. These points are later reconstructed into particle tracks. In addition, a strong magnetic field of 2 T curves the paths of the charged particles, which in turn allows the ID to identify an individual particle’s charge and momentum. The next two parts are the electromagnetic and tile calorimeter. These

## 1.5. PARTICLE DETECTORS

---

detectors weigh a few thousand tonnes and measure the energy that the particles deposit in the material. The only particles that make it through the calorimeters are neutrinos and muons. The former cannot be detected with the detectors in ATLAS. The latter however are detected by the Muon Spectrometer, a set of large detector plates placed all around the calorimeters. The last is the superconductive magnet which provides the magnetic field to allow the Muon Spectrometer to measure muon momenta. The ID has its own set of magnets that are used for the same purpose. To sum up, the Inner Detector measures the charge and momenta of the particles, the calorimeters measure their energies, the Muon Spectrometer measures muon tracks and momenta and the magnets provide magnetic fields, which curve the trajectories of the charged particles, allowing for identification of particle momenta.

The ATLAS detector has been designed to measure every collision taking place in its core. With 25 ns between collisions, this makes up 40 million collisions per second. The maximum realistic achievable rate of recording is approximately 100 kHz [15]. A recorded collision is referred to as an event. Every event holds information acquired by all the detectors within ATLAS. This amounts to approximately  $\sim 10^6$  channels of data, yielding an event size of approximately 10 MB. Therefore the data rate at the maximum achievable rate is 3 TB/s. To reduce the amount of data stored a special classification system with a complex trigger logic, which is in place to decide which events should be stored and analysed further. It reaches a decision in the order of tens of microseconds after an event. If this is the case, the data acquisition system triggers the readout of the entire detector. This way the recorded event rate is reduced from 100 kHz to  $\sim 500$  Hz.

A complex Trigger and Data Acquisition system (TDAQ) is in place to distribute the clock signal, configure the detectors, perform data acquisition and handle the output data. The data are then stored at the CERN computer centre and distributed across the globe by means of the GRID – a distributed data analysis and data storage system.

## 1.5 Particle detectors

Particle detectors, or radiation detectors, have first come into use at the end of the 19th century. In 1895 Wilhelm Röntgen used a photographic plate onto which he shone X-rays. Soon after, in 1912, Victor F. Hess discovered cosmic rays during a balloon flight. This paved the way for development of particle detectors. A cloud chamber was designed – a chamber filled with a supersaturated vapour of water or alcohol. If a highly energetic particle traversed the chamber, the mixture ionised, creating condensation nuclei. These traces were visible and were photographed. The particle detectors developed later relied on different types of interaction between the incident particles and the detector material, e.g. transition radiation, Cherenkov radiation and ionisation. The bubble chamber invented in 1952 used a superheated transparent liquid – a liquid heated just below its boiling point. A particle ionised the liquid, forming microscopic bubbles along its trajectory. Then followed the spark chamber and the wire chamber where the particle ionised the gas, causing a

spark between two parallel plates at a high potential difference. These are nowadays used in a handful of experiments and may often be seen in museums as showcases. Next were ionisation chambers, which measured the induced current of the free ionised charges moving in an externally applied electric field. Finally in the 1960s, semiconductor detectors were introduced. Their principle of operation is similar to that of an ionisation chamber, with the difference that a semi-conductive material is used as an ionisation medium instead of gas. Nowadays an ensemble of several types of detectors is used as a specialised detector system. Many considerations need to be taken into account when designing such a system: detector geometry, segmentation, event rate, efficiency, readout, support structures, cabling, cooling, cost etc.

Particle detectors can be divided in two groups: tracking detectors and calorimeters. The former are designed to measure particle momentum, charge, origin and direction of flight, with a minimal impact on their flight path or energy with the aim to optimise the spatial resolution. The calorimeters, on the other hand, measure the energy of the particles by stopping them. This means they need to be heavy and dense. A typical physics experiment nowadays consists of a tracking detector enclosed by a calorimeter. This way the energy, charge and momentum can be derived for every particle created in the collision.



## Chapter 2

# Diamond detectors for radiation detection

Diamond has been known for over two millennia, valued for its mechanical properties and its appearance. When the procedures for its synthesis were discovered, diamond made its way to a broad range of industries which exploit its optical and electrical properties. The discovery of the Chemical Vapour Deposition (CVD, described below) as a new synthesis process gave rise to a range of new applications. Purer specimens are used in electronics, high-power switching devices, electrochemical systems, radiation sensors, quantum computing etc. Recently it was found that it also exhibits superconductivity [17]. This thesis focuses on the use of diamond for radiation detection. An example of such a diamond sample is shown in figure 2.1.

Compared to a natural diamond, a CVD diamond used as a particle detector has almost no impurities (foreign atoms like nitrogen or boron). If proper procedures are followed, the diamond lattice can be grown very uniformly. This in turn improves electrical properties of the grown sample. Such a diamond is an almost perfect thermal and electrical insulator. However, its electrical behaviour is similar to that of a semiconductor. For this reason this chapter first introduces semiconductor detectors and then describes the principle of signal formation in semiconductors. Then it focuses on the diamond sensor and its properties.

**Chemical vapour deposition** (CVD) [18] is a process where a material is deposited from a gas onto a substrate, involving chemical reactions. It is often carried out under high pressure and high temperatures. It takes place in enclosed chambers called furnaces with careful regulation of the temperature, pressure and gas mixture. Synthetic diamond is grown at 700–900 °C with a mixture of hydrogen and methane gas. At this temperature the molecules dissociate into carbon and hydrogen atoms. The carbon atoms are the building blocks and are deposited on the surface of the substrate.

Under a carefully controlled pressure and temperature conditions with an added abrasive atomic hydrogen the graphitic bonds break and form into diamond bonds. The speed of the growth can be anywhere between 0.1 and 10 µm per hour. The detector grade samples are grown at a rate of the order of 1 µm per hour. They can grow up to several millimetres

## 2.1. SEMICONDUCTOR DETECTORS

---

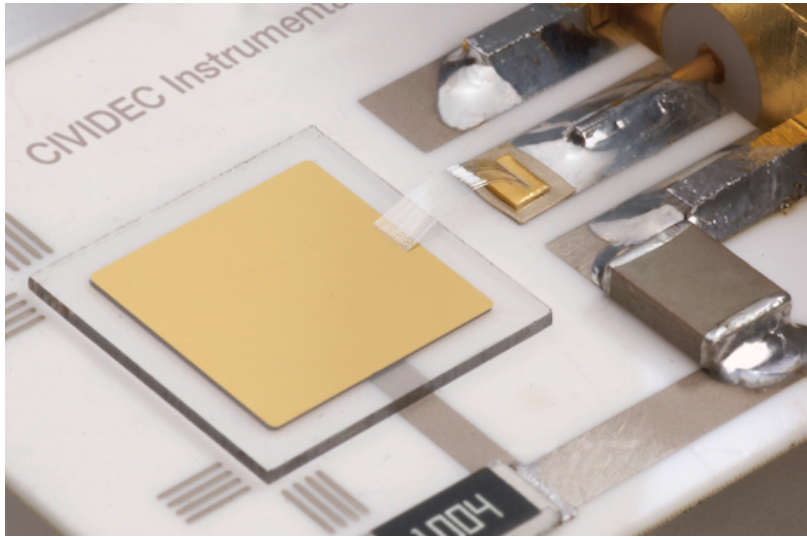


Figure 2.1: A pCVD diamond pad detector [19].

in thickness. The width of the samples, however, depends entirely on the substrate used. Diamond can be deposited on various materials: diamond, silicon, tungsten, quartz glass etc. The substrate material must be able to withstand the high temperatures during the CVD process. The diamond substrate does not need any surface pre-treatment. Carbon atoms form bonds with atoms in the existing crystal structure. This is the homo-epitaxial growth where the newly deposited atoms retain the orientation of the structure in the substrate. Other non-diamond substrates, however, need to be pre-treated, usually by being polished using diamond powder. Some powder particles remain on the surface, acting as seeds for the growth of small crystals or grains. These grains grow and at some point merge with the adjacent ones, making up a compact material. The lower side is later polished away. These diamonds are called *polycrystalline* (pCVD) whereas those grown on a diamond substrate are *single crystal* (sCVD) diamonds. The area of the former can be large - up to  $0.5 \text{ m}^2$  or more compact  $75 \text{ cm}^2$  in the case of detector grade diamonds, which can be further cut into smaller parts. The sCVD diamonds, on the other hand, can currently only achieve sizes up to  $1.5 \text{ cm}^2$ .

### 2.1 Semiconductor detectors

Semiconductor is a class of solids whose electrical conductivity is between that of a conductor and that of an insulator – of the order of  $10^{-5} \Omega^{-1} \text{ cm}^{-1}$ . Semiconductors consist of atoms with four electrons in their valence band, e.g. silicon–Si or germanium–Ge, or as combinations of two or more different materials, e.g. gallium arsenide–GaAs). The atoms in the lattice form valence bonds with adjacent atoms, creating solid crystal structures.

Semiconductor particle detectors are devices that use a semiconductor material to detect radiation. They work on the principle of an ionisation chamber. An incident particle ionises



Figure 2.2: The Insertable B-Layer – a silicon particle tracker installed in the ATLAS experiment in 2014 [21].

the atoms in the crystal lattice. The charges are freed if the deposited energy is higher than the energy band gap, i.e. the energy needed to excite an electron from its steady state to the conductance band. The freed charge carriers start drifting in an externally applied electric field, inducing current on the electrodes. The induced signal is amplified and read out by the electronics in the detector signal chain.

Semiconductor detectors are most widely used for tracking applications, like the Insertable B-Layer shown in figure 2.2 [20], which was installed in ATLAS Experiment in 2014. First, they can be produced in thin layers to minimise the impact on the path of the incident particles. Second, their low sensor capacitance allows for a fast signal response. Third, they are highly efficient and highly resistant to radiation damage. Finally, the industrial processes allow for a fine spatial segmentation, which in turn improves the track resolution of the detector systems.

Semiconductor sensors come in several configurations. The simplest type is a pad – a single plate with two electrodes. Pads are used for particle counting and radiation monitoring. Next is a strip detector, a more finely segmented detector made out of long parallel sensing areas or strips. Normally each strip has its own signal line for readout. Usually the strip detectors are used in pairs – one detector is placed on top of the other at an angle to increase spatial resolution in both axes. The third and the most finely segmented is a pixel detector, consisting of a 2D array of independent sensing areas. In tracking applications, pixel detectors are used where the need for a high detection resolution and granularity requirement is the highest. Due to their high production cost and a high number of signal channels, they can only cover limited areas. Strip detectors can be used to cover larger areas in several consecutive layers.

## 2.2 Principles of signal formation in semiconductors

Particles can interact with the sensor in several ways, e.g. via bremsstrahlung [22], elastic or inelastic scattering or nuclear reactions [23]. Bremsstrahlung is radiation created when a particle is decelerated due to interaction with the electric field of the core of an atom. Elastic scattering is deflection of the particle's trajectory due to the pull from the nucleus without depositing any energy in it. This is in principle an unwanted effect in semiconductors as it deteriorates the spatial resolution of the sensor. Inelastic scattering is the interaction through which an electron in the atom is *ionised*. Nuclear reaction is the direct interaction between the incident particle and the core of the atom. All these effects are competing and are dependent on the particle's mass, momentum etc. The scope of this chapter is to discuss the ionisation mechanism in semiconductors.

The energy of the electrons forming valence bonds between atoms in the crystal lattice is within the *valence band* [24]. To break a bond and excite the electron into a *conduction band*, a sufficient energy has to be applied. The minimal energy required is equal to the energy band gap  $E_g$  of the semiconductor. Typical  $E_g$  values are 0.7 eV in Ge, 1.12 eV in Si and 1.4 eV in GaAs. Diamond with its 5.5 eV band gap is considered an insulator. The separation between the conductive and valence band is referred to as *forbidden gap* where no electron states can exist.

An electron excited into the conduction band leaves behind a positively charged ion with a vacancy – a hole – in its valence band, as shown in figure 2.3a. A free *electron-hole pair* is thus created. The free electron travels through the crystal until it is recombined with another hole. Similarly the positive charge of the hole attracts a bound electron in the vicinity, causing it to break from the current bond and moving to the vacancy, thus leaving behind a newly created hole. The process continues, making it look like the hole is traveling through the material [24].

Both the electron and the hole are referred to as *charge carriers*. Without an externally applied electrical field, they propagate in random directions. Therefore on average there is no overall motion of charge carriers in any particular direction over time.

However, if an external electric field is applied to the crystalline structure, the free electrons and holes drift toward the positive and negative potential, respectively, as shown in figure 2.3b. While drifting, the charges couple with the electrodes, inducing current in the circuit, which is explained by the Shockley–Ramo theorem below. Upon reaching the electrodes the charges stop inducing the current. The equivalent electrical circuit is shown in figure 2.3c.

### 2.2.1 Signal induction by moving charges

The signal induction in a conducting plane by a point-like charge, which couples with an electrode, is derived in [25]. The electrode can in this case be modelled as an infinite conducting plane. When a point charge  $q$  is created (e.g. an electron-hole pair created via ionisation), its electrostatic field lines immediately couple with the electrode, as seen

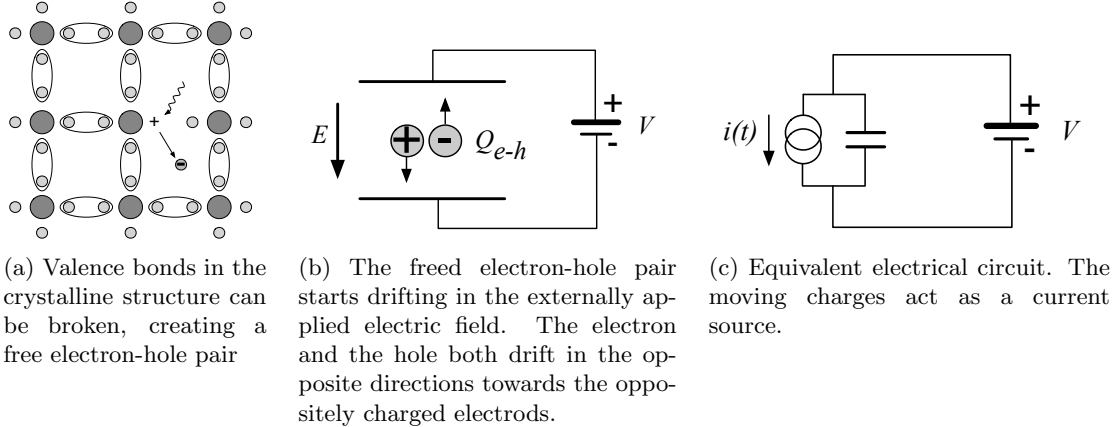


Figure 2.3: In the equivalent electrical circuit diagram the electron-hole creation and drift can be modelled as a current source with a capacitor in parallel.

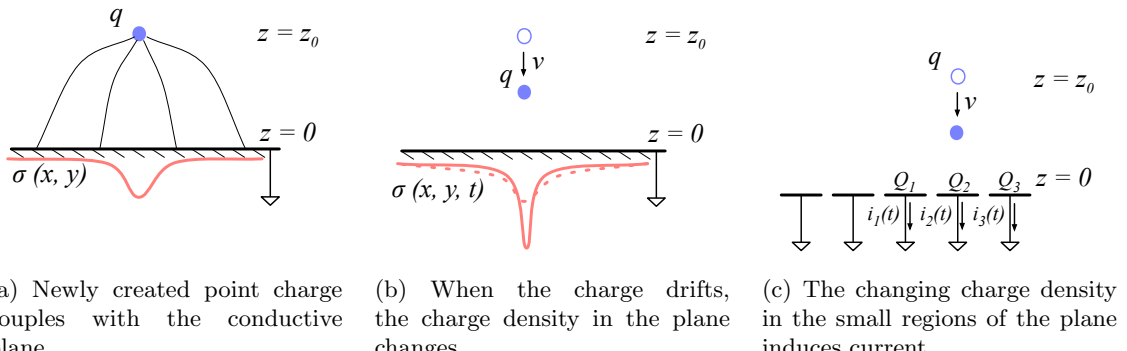


Figure 2.4: A point-like charge inducing current in a conductive plane.

in figure 2.4a. The electric field on the metal surface due to a point-like charge  $q$  at the distance  $z_0$  is

$$E_z(x, y) = \frac{qz_0}{2\pi\epsilon_0(x^2 + y^2 + z_0^2)^{\frac{3}{2}}} \quad E_y = E_z = 0. \quad (2.1)$$

A mirror charge appears on the conducting plane, with a charge density distribution

$$\sigma(x, y) = \epsilon_0 E_z(x, y) = \frac{qz_0}{2\pi(x^2 + y^2 + z_0^2)^{\frac{3}{2}}}. \quad (2.2)$$

The charge density integrated over the entire plane yields a mirror charge  $Q$ , which is an opposite of point charge  $q$ :

$$Q = \int_{-\infty}^{\infty} \int_{-\infty}^{\infty} \sigma(x, y) dx dy = -q. \quad (2.3)$$

The plane is then segmented into infinitely long strips with a width  $w$  whereby each of the strips is grounded, as shown in figure 2.4c. Considering a charge density distribution 2.2, the

## 2.2. PRINCIPLES OF SIGNAL FORMATION IN SEMICONDUCTORS

---

resulting mirror charge on a single strip  $Q_2$  directly below the point charge ( $x = 0, y = 0$ ) yields

$$Q_2(z_0) = \int_{-\infty}^{\infty} \int_{-w/2}^{w/2} \sigma(x, y) dx dy = -\frac{2q}{\pi} \arctan\left(\frac{w}{2z_0}\right) \quad (2.4)$$

If the charge starts moving towards the conducting plane, the mirror charge density distribution also changes, as shown in figure 2.4b. As a result the  $Q_2[z(t)]$  changes with time. The changing charge is in effect an induced electric current  $i_2(t)$ :

$$i_2(t) = -\frac{d}{dt} Q_2[z(t)] = -\frac{\partial Q_2[z(t)]}{\partial z} \frac{\partial z(t)}{\partial t} = \frac{4qw}{\pi[4z(t)^2 + w^2]} v. \quad (2.5)$$

The movement of the point-like charge therefore induces current in the conducting plane. The induced current is linearly dependent on the velocity of the point-like charge.

### 2.2.2 Shockley-Ramo theorem

W. Shockley [26] and S. Ramo [27] independently proposed a theory which explains how a moving point charge induces current in a conductor. The Shockley-Ramo theorem can therefore be used to calculate the instantaneous electric current induced by the charge carrier or a group of charge carriers. It can be used for any number of electrodes. It states that the current  $I_n^{\text{ind}}(t)$  induced on the grounded electrode  $n$  by a point charge  $q$  moving along a trajectory  $\mathbf{x}(t)$  reads

$$I_n^{\text{ind}}(t) = -\frac{dQ_n(t)}{dt} = -\frac{q}{V_w} \nabla \Psi_n[\mathbf{x}(t)] v(t) = -\frac{q}{V_w} \mathbf{E}_n[\mathbf{x}(t)] v(t), \quad (2.6)$$

where  $\mathbf{E}_n(\mathbf{x})$  is the *weighting field* of electrode  $n$  in the case where the charge  $q$  is removed, electrode  $n$  is set to voltage  $V_w = 1$  and all other electrodes are grounded. The weighting field is defined as the spatial differential of the *weighting potential*:  $\mathbf{E}_n(\mathbf{x}) = \nabla \Psi_n(\mathbf{x})$ . In the case of two parallel electrodes, the weighting field is  $E_w = -\frac{d\Psi}{dx} = -1/d$ , where  $d$  is the distance between the electrodes. The resulting induced current is therefore

$$i(t) = \frac{q}{d} v_{\text{drift}}(x, t), \quad (2.7)$$

whereby  $v_{\text{drift}}$  is the drift velocity of the point-like charge and  $d$  is the distance between the electrodes.  $d$  is defined by the dimensions of the sensor. The drift velocity is a function of the externally applied electric field, as defined in section 2.3. If the electric field is set to a constant value, the induced current is directly proportional to the drifting charge. Therefore, by measuring the height of the induced current at a specific point of time the number of moving charges can be deduced.

### 2.2.3 Thermal excitation

Electrons can be thermally excited to the conduction band. The intrinsic concentration of thermally excited electrons  $n_i$  in semiconductors is proportional to[24]

$$n_i \propto \exp\left(-\frac{E_g}{2k_B T}\right) \quad (2.8)$$

wherein  $k_B = 1.381 \times 10^{-23} \text{ m}^2 \text{ kg s}^{-2} \text{ K}^{-1}$  is the Boltzmann constant,  $E_g$  is the energy band gap of the semiconductor and  $T$  is the temperature in K. Due to the small band gap in semiconductors a significant amount of electrons already occupies the conduction band at room temperature due to thermal excitation, according to the probabilistic distribution. To reduce this effect semiconductor sensors are doped with donors and acceptors, forming a diode [24]. The diode is then inversely biased to deplete the material of all free charges. Doped silicon fulfils most of the needs for particle physics requirements and is therefore the most widely used material for particle detection. Diamond with its high energy band gap on the other hand only has a negligible number of thermally excited electrons at room temperature. Therefore a p-n junction is not needed, which simplifies the sensor production.

#### 2.2.4 Space charge

The Poisson equation shows that

$$\frac{d^2\Phi(x)}{dx^2} = \frac{dE(x)}{dx} = \frac{\rho(x)}{\epsilon} \quad (2.9)$$

where  $\rho(x)$  is the space charge distribution,  $E$  is the electrical field and  $\Phi$  is the voltage potential. In an ideal diamond, the externally applied high voltage potential on the two electrodes decreases linearly through the sensor. The electrical field is therefore constant throughout the sensor and the space charge distribution across it equals 0. However, space charge may be introduced in the material either by means of accumulating of charge carriers in the lattice (i.e. charge trapping) or already during sensor production. The space charge can be either permanent or changing – sometimes it is possible to reduce it, as is shown in chapter 3. All in all, it is very important to reduce it because it affects the shape of the electrical signal. Since the drift velocity of the charge carriers is proportional to the electrical field, the charges change their velocity while drifting through the space charge region. Figure 2.5 compares the voltage potential, the electrical field and the space charge for an ideal sensor as well as for that with a uniformly distributed positive space charge.

### 2.3 Carrier transport in a diamond sensor

This section describes the carrier transport phenomena in diamond. This theory provides the basis for discussion about the measurements in chapter 3. Table 5.2 compares the properties of diamond and silicon. Some of these values are revisited and used in the course of this thesis.

### 2.3. CARRIER TRANSPORT IN A DIAMOND SENSOR

---

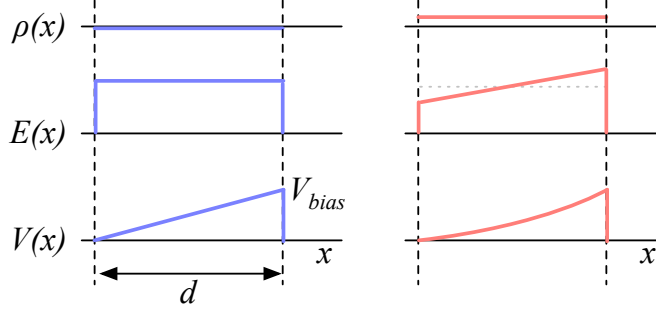


Figure 2.5: Left figure shows a profile of a diamond sensor only with an externally applied electric field. In the figure on the right a uniformly distributed space charge is added in the diamond, contributing to the internal electric field distribution. The induced current signal is proportional to the electrical field.  $d$  is the thickness of the diamond sensor.

Property	Diamond	Silicon
Band gap energy $E_g$ (eV)	5.5	1.12
Electron mobility $\mu_e$ ( $\text{cm}^2 \text{ V}^{-1} \text{ s}^{-1}$ )	1800 [28]	1500 [24]
Hole mobility $\mu_h$ ( $\text{cm}^2 \text{ V}^{-1} \text{ s}^{-1}$ )	2500 [28]	450 [24]
Breakdown field ( $\text{V cm}^{-1}$ )	$10^7$	$3 \times 10^5$
Resistivity ( $\Omega \text{ cm}$ )	$> 10^{11}$	$2.3 \times 10^5$
Intrinsic carrier density ( $\text{cm}^{-3}$ )	$< 10^3$	$1.5 \times 10^{10}$
Mass density ( $\text{g cm}^{-3}$ )	3.52	2.33
Atomic charge	6	14
Dielectric constant $\epsilon$	5.7	11.9
Displacement energy (eV/atom)	43	13 – 20
Energy to create an e-h pair (eV)	13	3.6
Radiation length (cm)	12.2	9.6
Avg. signal created/ $\mu\text{m}$ (e)	36	89

Table 2.1: Comparison diamond – silicon [24, 28].

When the charge carriers are freed in a semiconductor with no concentration gradient and without an externally applied electric field, they scatter in random directions with a thermal velocity  $v_{\text{th}}$  [24]. Their integral movement due to thermal excitation equals zero.

**Diffusion** is caused by the concentration gradient. In its presence the integral movement is in the direction of the lower concentration until an equilibrium is reached. The concentration profile dissolves with time forming a Gaussian distribution with variance  $\sigma(t) = \sqrt{Dt}$  [24].

**Drift** is caused by an externally applied electrical field. In that case the carriers move along the field lines. In a sensor with a high applied field the diffusion contribution is negligible.

**Drift velocity**  $v_{\text{drift}}(E)$  is the speed at which the charge carriers drift through the diamond sensor [24].

**Mobility**  $\mu$  is a proportionality factor between the  $v_{\text{drift}}$  and the electric field  $E$  at low electric fields:  $v_{\text{drift}} = \mu E$ . Its units are in  $\text{cm}^2 \text{V}^{-1} \text{s}^{-1}$ .

**Phonon transport** is the transfer of energy of the moving charges to the lattice.

**Saturation velocity**  $v_{\text{sat}}^e$  is a velocity limit above which the carriers cannot reach. This is due to increasing phonon transport at a high electric field. The  $v_{\text{sat}}^e = v_{\text{sat}}^h = (14.23 \pm 0.12) \times 10^6$  cm/s for both positive and negative charge carriers has been derived from the measurements in [29].

The final equation for  $v_{\text{drift}}$  is therefore [30]

$$v_{\text{drift}}(E) = \mu(E)E = \frac{\mu_0 E}{1 + \frac{\mu_0 E}{v_{\text{sat}}}}. \quad (2.10)$$

It can be retrieved experimentally via the transit time measured with the Transient Current Technique (TCT). This technique enables the measurement of transit time  $t_t$  of the carriers through the sensor with the thickness  $d$ .

$$v_{\text{drift}}(E) = \frac{d}{t_t(E)}. \quad (2.11)$$

The velocities for holes and electrons usually differ. In diamond, the holes travel approximately 30 % faster than electrons at the room temperature [28].

## 2.4 Radiation-induced current signals

When a highly-energetic particle travels through the sensor, it interacts with atoms in the lattice. It ionises the valence electrons, creating electron-hole (e-h) pairs on its way. It can either deposit only a fraction of its energy and exit the sensor on the other side or it can get stopped in the sensor, depositing all of its energy. A special case is when it interacts with the core of the atom in the middle of the sensor by means of a nuclear interaction. All these various types interactions produce different amounts and different spatial distributions of e-h pairs.

The two most frequent types are shown in figure 2.6. The first figure shows the interaction of an incident MIP. The electrons and holes created all along the trajectory of the particle immediately start drifting towards the positive and negative electrode, respectively. At  $t = 0$  all charges drift, contributing to the maximum induced current. Those closest to the electrodes have a very short drift path. They stop inducing current upon reaching the electrode. The resulting current signal is a triangular pulse with a sharp rising edge and a linear falling edge. Gradually all the charge carriers reach the electrode. The accumulated charge  $Q_s$  equals to the sum of the contributions of the positive and negative charge carriers.

The second type of interaction happens when the particle is stopped in the diamond close to the point of entry. Most of its energy is deposited in a small volume close to the electrode. A cloud of charge carriers is created and the charges with the shorter path to the electrode disappear almost instantly. The carriers of the opposite charge, however, start drifting through the sensor to the other electrode. In an ideal diamond sensor, their velocity

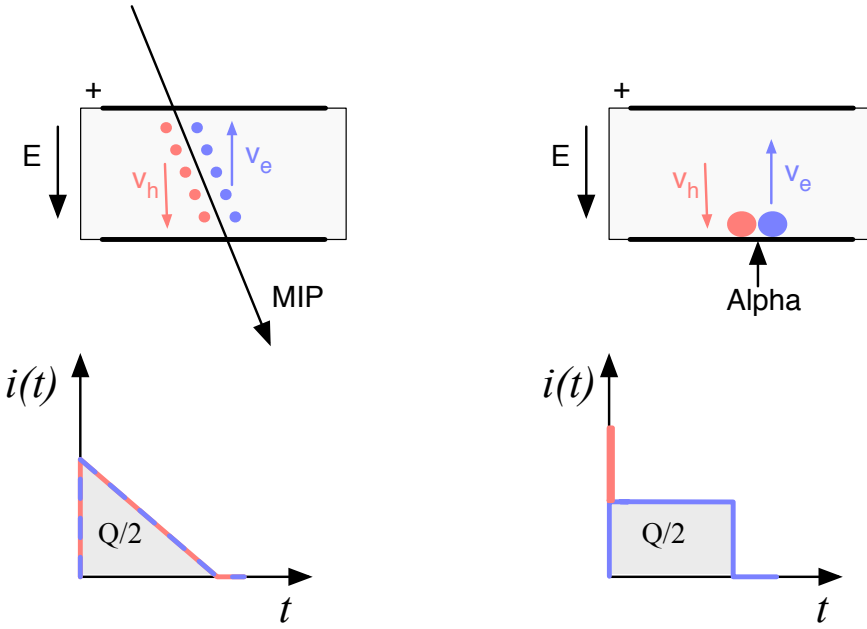


Figure 2.6: Charge carrier drift in diamond for  $\beta/\gamma$  and for  $\alpha$  particles crossing the sensor at  $t = 0$ .

is constant throughout the drift up until they are collected at the opposite electrode. The contribution of the first charge cloud is a peak with a short time. The cloud drifting through the sensor, on the other hand, induces a current signal with a flat top. The resulting signal has a shape of a rectangle, with a spike in the beginning. The accumulated charge  $Q_s$  is equal to a half of the deposited charge by the stopped particle.

The two aforementioned types of interactions have well defined signal responses. Nuclear interactions on the other hand yield various results. The resulting signal shape depends on the decay products of the interaction, which can be  $\alpha$ ,  $\beta$  or  $\gamma$  quanta or other nuclei, inducing a mixed shaped signal.

#### 2.4.1 Mean energy loss

A mean energy loss of a particle traversing the detector as a function of the momentum is given with the Bethe-Bloch equation [31]:

$$-\left\langle \frac{dE}{dx} \right\rangle = \frac{4\pi}{m_e c^2} \cdot \frac{nz^2}{\beta^2} \cdot \left( \frac{e^2}{4\pi\epsilon_0} \right)^2 \cdot \left( \ln \left( \frac{2m_e c^2 \beta^2}{I \cdot (1 - \beta^2)} \right) - \beta^2 \right) \quad (2.12)$$

The resulting function for a muon is shown in figure 2.7. At a momentum of around 300 MeV/c the incident particle deposits the lowest amount of energy. Hence it is referred to as the *minimum ionising particle* or a MIP.

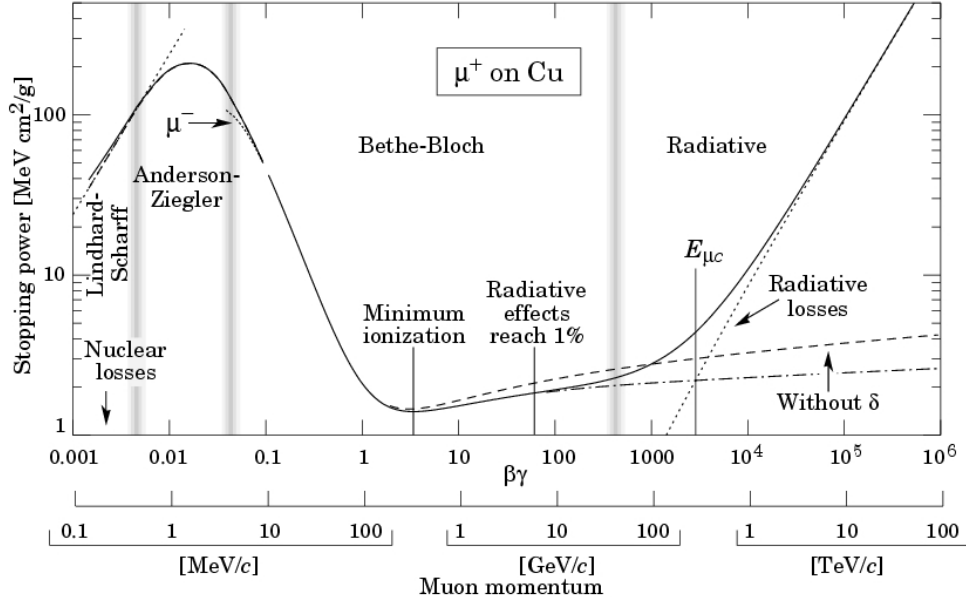


Figure 2.7: Stopping power for muons according to the Bethe-Bloch formula [31].

#### 2.4.2 Signal fluctuation

Two important sensor properties are the magnitude of the signal and the fluctuations of the signal at a given absorbed energy. They determine the relative resolution  $\Delta E/E$ . For semiconductors the signal fluctuations are smaller than the simple statistical standard deviation  $\sigma_Q = \sqrt{N_Q}$ . Here  $N_Q$  is the number of released charge pairs, i.e. the ratio between the total deposited energy  $E_0$  and the average energy deposition  $E_i$  required to produce an electron-hole pair. [32] shows that the standard deviation is  $\sigma_Q = \sqrt{F N_Q}$ , where  $F$  is the Fano factor [32] (0.08 for diamond and 0.115 for silicon [33]). Thus, the standard deviation of the signal charge is smaller than expected,  $\sigma_Q \approx 0.3\sqrt{N_Q}$ . The resulting intrinsic resolution of semiconductor detectors is

$$\Delta E_{\text{FWHM}} = 2.35 \sqrt{F E E_i} \quad (2.13)$$

wherein  $E_i(Si) = 3.6$  eV and  $E_i(Di) = 13$  eV. E.g., for an  $\alpha$  particle with energy  $E_\alpha = 5.5$  MeV the calculated resolution in diamond is equal to  $\Delta E_{\text{FWHM}} = 5.6$  keV. This defines the minimum achievable resolution for energy spectroscopy with semiconductors.

#### 2.4.3 Charge collection

The total measured charge  $Q_i$  is the integral of the induced current:

$$Q_i = \int i_{\text{ind}}(t) dt. \quad (2.14)$$

The expected charge  $Q_0$  can be calculated using the thickness of the sensor  $d$  and the average number of e-h pairs created per  $\mu\text{m}$   $\delta_d$ , which is 36 e-h/ $\mu\text{m}$  for diamond according

## 2.4. RADIATION-INDUCED CURRENT SIGNALS

---

to table 5.2. The expected charge created by a MIP flying through a sensor with a thickness  $d = 500 \mu\text{m}$  perpendicular to the electrodes is

$$Q_{\text{MIP}} = \delta_d \cdot d \cdot q = 18 \times 10^3 \text{ eh} \cdot q = 2.9 \text{ fC} \quad (2.15)$$

where  $q = 1.6 \times 10^{-19} \text{ C}$  is the elementary charge. If a particle stops in the sensor, it deposits all its energy. In this case the number of created e-h pairs is calculated according to equation 2.16 using  $E_{\text{eh}}$ , the energy required to create an e-h pair. For diamond this value is 13, according to table 5.2. For a 5.5 MeV  $\alpha$  particle emitted from an  $^{241}\text{Am}$  source the expected charge is

$$Q_\alpha = \frac{E}{E_{\text{e-h}}} \cdot q = \frac{5.5 \text{ MeV}}{13 \text{ eV}} \cdot q = 4.25 \times 10^5 \text{ eh} \cdot q = 68 \text{ fC}. \quad (2.16)$$

where  $E$  is the energy of the incident particle, which is almost for a factor of 24 larger than expected charge of a MIP. The charge collection efficiency (CCE) is the ratio between the measured and expected charge:

$$\text{CCE} = \frac{Q_i}{Q_0} = \frac{Q_i}{\delta_d \cdot d} \cdot 100\%. \quad (2.17)$$

The charge collection distance (CCD) is a measure of an average path that the charge carriers travel before getting trapped:

$$\text{CCD} = \frac{Q_i}{\delta_d} \quad (2.18)$$

and is usually given in units of  $\mu\text{m}$ .

Carriers that get trapped stop contributing to the overall induced current on the electrodes. The more charges are trapped along their drift path, the more the current induced on the electrodes is decreased. This in turn yields a lower integrated charge. An expected CCE for non-irradiated sCVD diamonds is close to 100 %. For highest quality non-irradiated pCVD diamonds it ranges between 40 % and 60 %. In other words, high-quality pCVD diamonds already have traps introduced by means of grain boundaries, which are created in the growing process. Traps can also be created by damaging the diamond using radiation (discussed in section 2.5). The more the sensor is irradiated, the larger number of traps is introduced in the material and the higher is the probability that the carriers are stopped on the way, reducing in turn the integrated charge. Therefore the CCD and CCE can be used as a means to quantify the detector damage due to radiation.

### 2.4.4 Charge trapping

Various types of lattice defects can be created in diamond, similar to those in silicon [34]. Figure 2.8 shows several examples of lattice damage:

- a) foreign interstitial (e.g. H, Li),
- b, c) foreign substitutional (e.g. N, P, B),

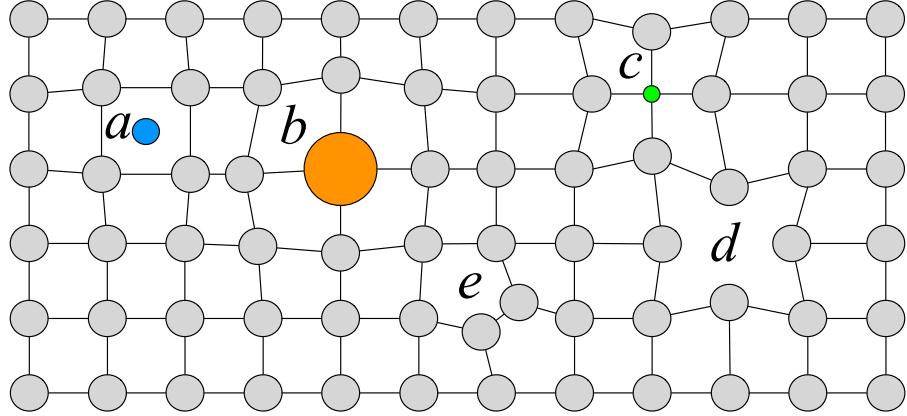


Figure 2.8: Impurities and non-uniformities in the crystal lattice due to radiation damage.

- d) vacancy and
- e) self interstitial.

These non-uniformities form new energy levels in the forbidden gap. These intermediate levels are referred to as charge traps because they can trap moving charge carriers. The energy level of the trapped carriers is reduced from the conduction band to the energy level of the trap. Different types of lattice damage have different energy levels. The carriers trapped in a shallow trap – an energy level close to the conduction band – have a high probability of being thermally excited back into the conduction band whereby they continue drifting towards the electrode. Their activation energy is therefore low. Those trapped in a deep trap close to the middle of the forbidden gap need a much higher activation energy, which in turn increases the average time to their release due to thermal excitation.

The energy band jumping goes the other way, too. The carriers in the valence band may use the intermediate energy levels as “stepping stones” to jump to the conduction band and start drifting in the externally applied electric field. These intermediate energy levels are referred to as the generation centres of leakage current.

The charge carriers that drift through the bulk get stopped in the charge traps with a certain probability. This trapping happens uniformly throughout the diamond. In other words, the number of carriers in the moving charge cloud is gradually reduced. This in turn reduces the induced current. The number of drifting carriers per unit of length follows a decaying exponential function

$$I(t) = I_0 + I(0) \cdot e^{-\frac{t-t_0}{\tau}}, \quad (2.19)$$

where  $I(0)$  is the initial induced current,  $I_0$  is the end current,  $t$  is time,  $t_0$  is temporal displacement of the pulse and  $\tau$  is the decay time constant. This value describes how long it takes before the amplitude of the pulse decreases to 63 % of its initial height.

#### 2.4.4.1 Priming/pumping

Priming or pumping [35] is a process of irradiating the diamond with ionising radiation with a goal to improve the sensor properties. The pumping process strongly reduces the concentration of active carrier trapping centres. This leads to an enhancement of electronic properties of such material. The improved transport properties due to a reduced number of active charge traps give rise to an increased charge collection efficiency. The diamond is usually pumped for a few hours using a strong  $\beta$  source, preferably a  $^{90}\text{Sr}$  source with the activity of at least 50 MBq. The diamond remains in a pumped state from a few minutes to several days, depending on the quality of the material. A direct exposure to light results in an immediate return to an non-pumped state.

## 2.5 Radiation damage

Exposure to ionising radiation degrades sensors by deforming the crystal lattice and introducing charge traps in the material.

Radiation damage varies with the type of radiation and its energy. There are several models existing [36, 37] that try to explain the impact of irradiation and to provide *damage factors* to compare the radiation damage between different particles. The standard way is to convert the damage into *1 MeV neutron equivalent fluence* [38]. Some models have been extensively verified with simulations and with experiments. In these experiments the charge collection in sensors is measured before and after irradiation. This procedure is repeated several times, with a measurement point taken after every irradiation. Then the charge collection for this set of measurements is plotted as a function of the radiation dose received by a specific particle at a specific energy. From this a damage factor  $k_\lambda$  can be extracted. Damage factors have to be measured across a range of energies and types of radiation to properly quantify the damage in the sensors. Finally they are compared to the simulations to validate the theoretical models.

Diamond is an expensive material and the technology is relatively new as compared to silicon. Therefore few institutes are carrying out diamond irradiation studies. To join the efforts, the RD42 collaboration [39] has been formed. It gathers the experimental data from diamond irradiation studies. Unlike with silicon, the experimental results so far show no significant correlation with the NIEL (non-ionising energy loss) model [36], which correlates detector efficiency with the number of lattice displacements. Therefore an alternative model was proposed [37], correlating the diamond efficiency with the number of displacements per atom (DPA) in the material. The idea is that if the recoil energy of an incident particle is higher than the lattice binding energy (42 eV for diamond), the atom is displaced from its original position. The newly formed vacancy acts as a trap for drifting charge carriers. The more displacements that form in the crystal, the higher is the probability that a drifting carrier gets trapped. However, different types of particles interact differently with the material. In addition the mechanisms of interaction at low energies are different to those

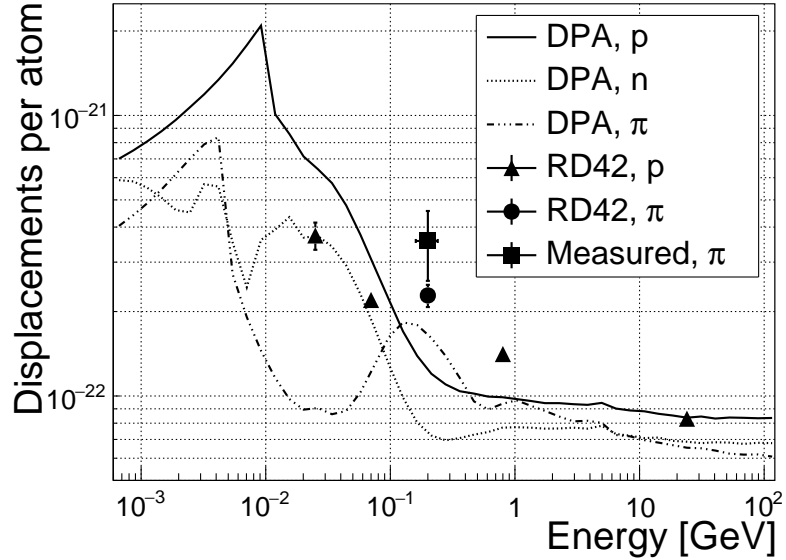


Figure 2.9: Diamond radiation damage - a model based on displacements per atom [37]. The figure shows the DPA as a function of the kinetic energy for protons, neutrons and pions. Added are data points for protons and pions by RD42 [40].

at high energies. To assess the damage for individual particles at a range of energies, simulations need to be run first. The simulation shown in [37] shows the DPA model for a range of energies of proton, pion and neutron irradiation in diamond. Figure 2.9 contains the simulation results as well as the superimposed empirical results of several irradiation studies. According to the figure, a 300 MeV pion beam damages the diamond material twice as much as a 24 GeV proton beam. The data points obtained by RD42 are also added to the figure. They have been normalised to damage by 24 GeV protons. This value has been chosen because radiation damage at this energy and radiation type is well understood at CERN.

#### 2.5.0.1 Irradiation damage factor

The irradiation damage factor  $k_\lambda$  is a means to quantify irradiation damage of a specific type of radiation at a specific energy. Via this factor different types of irradiation can be compared. It is obtained experimentally by measuring the CCD of a number of samples at various irradiation steps and fitting the equation 2.20 to the data.  $\lambda$  is the measured CCD,  $\lambda_0$  is the CCD of a non-irradiated sample and  $\Phi$  the radiation dose. As a reference, the damage factor for 24 GeV protons is set to  $1 \times 10^{-18} \mu\text{m}^{-1} \text{cm}^{-2}$ .

$$\frac{1}{\lambda} = \frac{1}{\lambda_0} + k_\lambda \cdot \Phi \quad (2.20)$$

## 2.6 Temperature effects

The band gap energy in diamond is equal to  $E_g = 5.5$  eV while the average energy to produce an electron-hole pair is  $E_{e-h} = 13$  eV. This means there is excessive energy deposited in the diamond bulk. An incident  $\alpha$ -particle stops within  $\sim 10\text{--}15 \mu\text{m}$  of the bulk, transferring all its energy to the lattice during deceleration. A part of this energy directly ionises the carbon atoms, creating free electron-hole pairs.

The remaining energy, however, is converted into lattice vibrations – phonons [41, 28]. In other words, the lattice within the ionisation volume of approximately  $\sim 15 \mu\text{m} \times \sim 2 \text{ nm}$  [28] is briefly heated up. The hot plasma then cools down to the temperature of the surrounding material by means of heat dissipation, i.e. phonon transport.

The free electron binds with the free hole into a bound state (not recombination) – the exciton [42]. The exciton binding energy is 80 meV, which introduces an energy level within the forbidden gap just under the conduction band. At higher temperatures the lattice provides enough energy to thermally excite the electron from the exciton state back to the conduction band. At lower temperatures, however, the exciton lifetime increases, which means that it takes a longer time for the electrons to get re-excited to the conduction band. The re-excitation lifetime at room temperature is  $\sim 30$  ps, increasing to  $\sim 150 \mu\text{s}$  at 50 K [28]. This means that some of the bound electrons do not even start drifting within the period of  $\sim 10$  ns, which is the expected carrier drift time. When they are finally freed, the current they induce is already hidden in the electronics noise. The effective area of the observed current pulse is therefore smaller than that of a pulse induced by all the carriers drifting at the same time. This in effect reduces the measured collected charge. The longer the time constant, the lower the measured collected charge, as shown in section 3.4.2.1.

### 2.6.0.1 Collected charge as a function of temperature

The area below the current pulse is proportional to the charge collected by the diamond detector. The collected charge is measured as a function of temperature. First, the amplitude values of the averaged pulses at a bias voltage of  $\pm 500$  V and across the temperature range between 4 K and 295 K have to be integrated. Then a calibration factor is used to derive the charge for all data points. The resulting values for electrons and holes are plotted in figures 3.17 and 3.18, respectively.

## 2.7 Electronics for signal processing

This section describes the electronics of a detector, starting with a description of signal amplifiers and then discussing the digitisation and signal processing. All these stages are necessary to extract information from the sensor. First, the signal has to be amplified. Then it is digitised and finally processed in a specially designed processor or a logic unit.

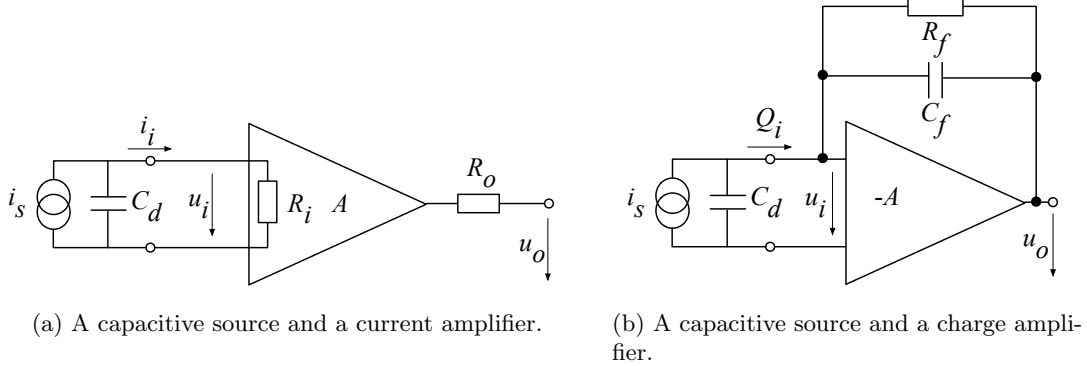


Figure 2.10: Simplified equivalent circuits of a current and charge amplifier.

### 2.7.1 Signal preamplifiers

The signal charge generated in the sensor by a single energetic particle is of the order of a few fC. The range of the induced current for single particles is typically between  $10^{-8}$  A ( $\beta, \gamma$  radiation) and  $3 \times 10^{-7}$  A ( $\alpha$  radiation). Signals as low as these have to be pre-amplified before processing. Depending on the measurement, several types of signal amplifiers can be used. The preamplifiers are designed to minimise electronic noise while maximising gain, thus maximising the signal-to-noise ratio (SNR). In addition, a bandwidth limit must be optimised to minimise the information loss due to signal shape deformation. A critical parameter is the total capacitance, i.e. the sensor capacitance together with the capacitance load of the preamplifier. The SNR improves with a lower capacitance. Several types of amplifiers can be used, all of which affect the measured pulse shape. Two preamplifiers are used most commonly, a current and a charge sensitive amplifier. Both are described below.

#### 2.7.1.1 Current amplifier

Figure 2.10a shows the equivalent circuit of a current source and a current amplifier. An amplifier operates in current mode if the source has a low charge collection time  $t_c$  with respect to the  $R_i C_d$  time constant of the circuit. In this case the sensor capacitance discharges rapidly and the output current  $i_o$  is proportional to the instantaneous current  $i_i$ . The amplifier is providing a voltage gain, so the output signal voltage  $u_o$  is directly proportional to the input voltage  $u_i$ :

$$u_o(t) = A \cdot R_i \cdot i_s(t). \quad (2.21)$$

The detector capacitance  $C_d$  together with the input resistance of the amplifier  $R_i$  defines the time constant of the signal, as shown in figure 2.11. The higher  $C_d$ , the slower is the response of the amplifier. For the case of the diamond sensor, which has the capacitance of the order of 2 pF and the input resistance of 50  $\Omega$ , the resulting time constant is  $\tau = 10^{-10}$  s. This yields the signal rise time  $t_r \sim 2.2\tau = 2.2 \times 10^{-10}$  s.

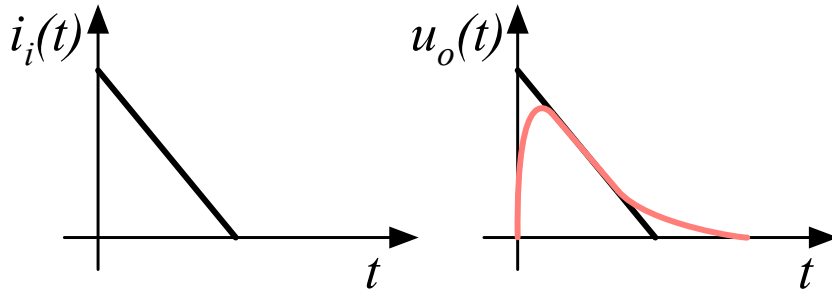


Figure 2.11: Input and output signal of the current amplifier.

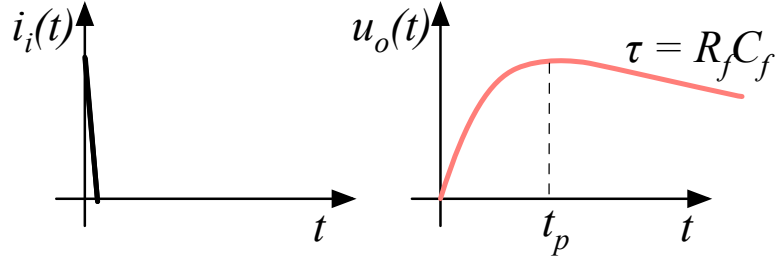


Figure 2.12: Input and output signal of the charge amplifier.

### 2.7.1.2 Charge-sensitive amplifier

In order to measure integrated charge in the sensor, a feedback loop is added to the amplifier, as shown in figure 2.10b. The feedback can be used to control the gain and input resistance, as well as to integrate the input signal. The charge amplifier is in principle an inverting voltage amplifier with a high input resistance.

In an ideal amplifier the output voltage  $u_o$  equals  $-Au_i$ . Therefore the voltage difference across the capacitor  $C_f$  is  $u_f = (A + 1)u_i$  and the charge deposited on the capacitor is  $Q_f = C_f u_f = C_f(A + 1)u_i$ . Since no current can flow into the amplifier, all of the signal current must charge up the feedback capacitance, so  $Q_f = Q_i$ .

In reality, however, charge-sensitive amplifiers respond much slower than is the duration of the current pulse from the sensor. In addition, a resistor is added to the feedback line in parallel to the capacitor. The resistor and capacitor define the decay time constant of the pulse, as shown in figure 2.12. This is necessary to return the signal to its initial state to be ready for a new measurement.

### 2.7.1.3 Analogue electronic noise

The electronic noise determines the ability of a system to distinguish different signal levels. The analogue signal contains ample information about the type and energy of incident radiation, which can quickly be erased or altered if the signal properties change. Therefore the noise contributions to the signal must be well understood to qualify the information the signal is carrying. The important contributions are listed below. Thermal or Johnson–Nyquist noise [43, 44] is the dominant noise contribution in the use case for diamond detector signal amplification and therefore defines the limitations of the detector system. This noise type is generated by the random thermal motion of charge carriers. The frequency range of the thermal noise is from 0 to  $\infty$  with a predominantly uniform distribution. Therefore this is nearly a white noise. The resulting signal amplitude has a Gaussian distribution. The RMS of the open-loop equivalent voltage is defined as

$$u_{\text{RMS}} = \sqrt{4k_B RT \Delta f} \quad (2.22)$$

where  $k_B$  is the Boltzmann constant,  $R$  is the input resistance of the amplifier,  $T$  its temperature and  $\Delta f$  the frequency range. This equation shows that it is possible to reduce the noise RMS by either (1) reducing the frequency range, (2) reducing the resistance or (3) reducing the temperature.

Contributions of shot noise, flicker noise and burst noise and other types are not significant relative to the thermal noise. However, the contributions of external factors can severely deteriorate the signal. This means the noise produced by capacitive or inductive coupling with an external source, which causes interference in the signal. These effects can be reduced by shielding the electronics and avoiding ground loops.

### 2.7.2 Analogue-to-digital converters

An analogue-to-digital converter (ADC) is a device that converts the analogue electrical signal on the input to its digital representation - a series of digital values. This involves a quantisation – *sampling* of the signal at a defined sampling period, resulting in a sequence of samples at a discrete time period and with discrete amplitude values. The resolution of the ADC is the number of output levels the ADC can quantise to and is expressed in bits. For instance, an ADC with a resolution equal to  $n = 8$  bit has a dynamic range of  $N = 2^n = 256$  steps. The resulting voltage resolution  $Q_{\text{ADC}}$  at the input voltage range of  $V_{\text{ADC}} = \pm 50$  mV is then

$$Q_{\text{ADC}} = \frac{V_{\text{ADC}}}{2^n} = \frac{100 \text{ mV}}{2^8 \text{ bit}} = 0.39 \text{ mV/bit.} \quad (2.23)$$

With a sampling period of  $t_s = 1$  ns the sampling rate is  $f_s = 1$  GS/s (gigasample per second).

**Quantisation error and quantisation noise** (or a round-off error) is a contribution to the overall measurement error due to digitisation (rounding). The quantisation error is defined as a difference between the actual analog value and the closest digitised representation

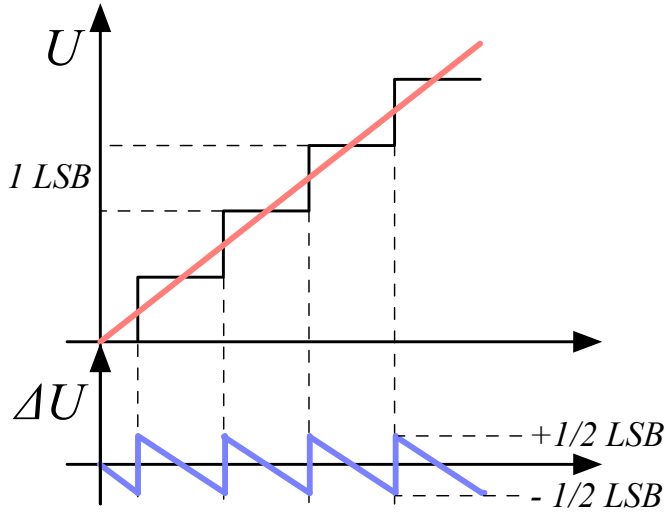


Figure 2.13: Input signal digitisation and quantisation error.

of this value, therefore by the least significant bit (LSB), as seen in figure 2.13. The input signal amplitude is typically much larger than than the voltage resolution. In this case the quantisation error is not directly correlated with the signal and has an approximately uniform distribution. The probability density function  $P(x)$  therefore has a rectangular shape bounded by  $(-\frac{1}{2}\text{LSB}, \frac{1}{2}\text{LSB})$ :

$$P(x) = \begin{cases} \frac{1}{\text{LSB}}, & -\frac{1}{2}\text{LSB} \leq x \leq \frac{1}{2}\text{LSB} \\ 0, & \text{otherwise.} \end{cases} \quad (2.24)$$

$$(2.25)$$

The height equal to  $\frac{1}{\text{LSB}}$  preserves the integrated probability of 1. The variance of the distribution is

$$\sigma^2 = \int P(x)(x - \mu)^2 dx. \quad (2.26)$$

The population mean is  $\mu = 0$ , therefore

$$\sigma^2 = \int_{-\frac{1}{2}\text{LSB}}^{\frac{1}{2}\text{LSB}} \frac{1}{\text{LSB}} x^2 dx = \frac{x^3}{3\text{LSB}} \Big|_{-\frac{1}{2}\text{LSB}}^{\frac{1}{2}\text{LSB}} = \frac{\text{LSB}^2}{12}. \quad (2.27)$$

The RMS of the quantisation noise is defined as the square root of the variance:

$$\Delta Q_{\text{ADC}} = \sqrt{\sigma^2} = \frac{1}{\sqrt{12}} \text{LSB} \sim 0.289 \text{ LSB}. \quad (2.28)$$

For the example above the quantisation error equals  $\Delta Q_{\text{ADC}} = 0.11 \text{ mV}$ . The error depends strongly on the linearity of the ADC, but this is out of scope of this document as the devices used have ADCs with a very good linearity.

### 2.7.3 Digital signal processing

The digitised signal can be processed to extract useful information. Therefore after the signal amplification and digitisation the signal is routed in a device which handles the digital analysis. The signal can either be processed immediately (in real time) or it can be saved to a data storage for analysis at a later stage (offline). The devices carrying out the processing can be multipurpose (e.g. Field Programmable Gate Arrays) or dedicated (e.g. Application-Specific Integrated Circuits).

**Field Programmable Gate Array** (FPGA) is an integrated circuit designed to be re-programmable and reconfigured after manufacturing. It consists of a set of logic gates that can be interconnected in numerous combinations to carry out a set of logic operations. Many such logic operations can take place in parallel, making the FPGA a powerful tool for signal processing. FPGAs are often used during system development or in systems in which the requirements might change with time. They can be reprogrammed in the order of seconds. In addition, the logic design only needs minor changes when migrating to a newer version of the FPGA chip of the same vendor. The FPGAs also offer faster time-to-market with comparison to application-specific solutions, which have to be developed. On the other hand, the price per part can be significantly higher than for the application-specific solutions. Also, their other major disadvantages are a high power consumption and a relatively low speed as compared to more application-specific solutions. However, today's solutions are capable of clock speeds higher than 500 MHz. Together with the integrated digital signal processing blocks, embedded processors and other modules, they are already very powerful and versatile. All in all, FPGAs are a good choice for prototyping and limited production, for projects with limited requirements for speed and complexity.

**Application-Specific Integrated Circuit** (ASIC) is an integrated circuit designed for a specific use. The design cannot be modified after chip production, as is the case with FPGAs. On the other hand, the ASICs can be optimised to perform a required operation at a high speed and at a low power consumption. In addition, due to the specific design the size of the chip can be much smaller. ASICs can be designed as hybrid chips, containing both a digital and an analog part. Finally, ASICs can be designed to withstand much higher irradiation doses than FPGAs and can therefore be used in harsh environments like in space or in particle colliders.

To update the chip, the design has to be submitted to a foundry, which produces the new chips with a turnover time of 4–6 weeks. The costs of a submission are high, but the price per part can be reduced significantly with a high volume. To sum up, ASICs are used for high volume designs with well defined requirements where some stringent constraints in terms of power consumption and speed have to be met.

## 2.7. ELECTRONICS FOR SIGNAL PROCESSING

---

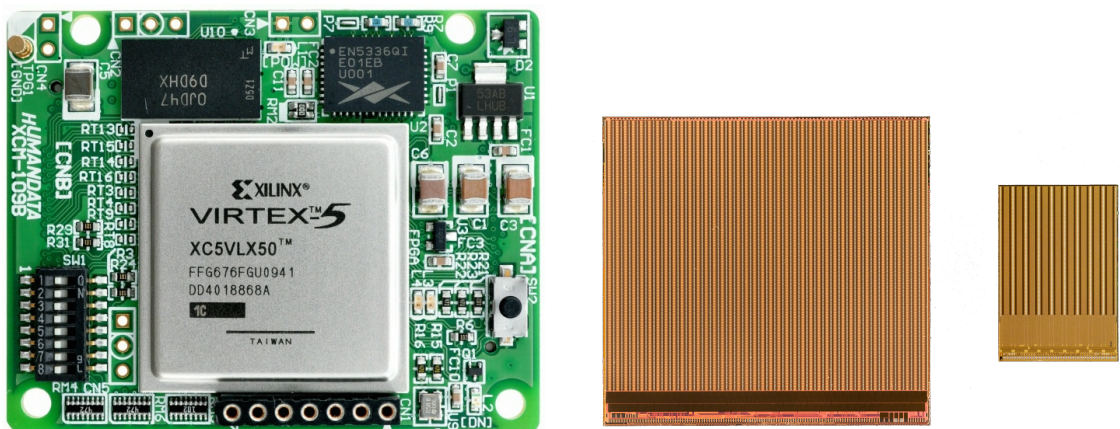


Figure 2.14: An example of a Xilinx Virtex 5 FPGA [45] and an FE-I4 and FE-I3 ASIC chip [46].

## Chapter 3

# Diamond irradiation study

The aim of the study in this chapter is to find the operational limitations of diamond detectors for spectroscopy and tracking applications. The chapter contains the measurement results of data taken with diamond sensors. First the measurement setup is described in section 3.1. Then the measured particle spectra are shown in 3.2. This is followed by a study of effects of the irradiation damage on the electrical signal of the diamond detector. The last section shows the results of the measurements of irradiated diamond samples at cryogenic temperatures. The studies compare the experimentally acquired data with the theory from the previous chapter and define limitations of the diamond detectors in terms of radiation and temperature.

Diamond sensors are mainly used for two types of measurements: particle counting and spectroscopy. The first type of measurements depends on the sensor efficiency – its ability to detect all or at least a known percentage of incident particles. The energy of the particles is not so important; what bears the information is the rate and the spatial distribution. Here the particles do not necessarily stop in the bulk, but rather continue their way. In spectroscopy, on the other hand, the particles stop within the sensor, depositing all their energy. This energy is then measured by collecting the freed charge carriers. The goal of the experiments described in this chapter is to:

1. Quantify the efficiency of the sCVD diamond in counting mode,
2. Quantify the degradation of the efficiency as a function of the received radiation dose,
3. Quantify the macroscopic effects on charge carrier behaviour as a function of the received radiation dose and
4. Define limitations for use in spectroscopy.

The results discussed here show that there are several limitations for using diamond as a radiation detector. All of them need to be taken into account when designing a new measurement device. The irradiation study allows for an estimation of the lifetime of the detector and a prediction of the longterm signal degradation as a function of the received radiation dose. The result of the study is a correction factor, which can be applied during data analysis to ensure that the analysis results are stable despite the detector degradation.

### 3.1. MEASUREMENT SETUP

---

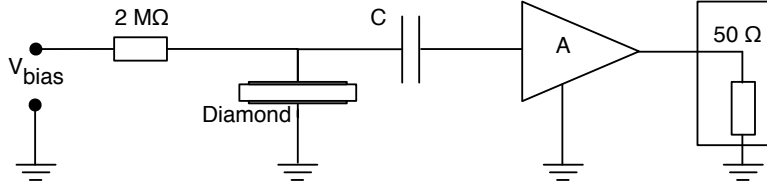


Figure 3.1: Diagram of a diamond detector readout chain.

## 3.1 Measurement setup

The first step of designing a measurement setup is to define the measurement conditions, such as the temperature, the type of radiation and its flux. The second step is to ensure that the setup is insensitive to external electromagnetic interferences and that it minimises electrical noise in the system. The setup needs to be calibrated before use.

Shielding has to be applied wherever possible. For instance, aluminium foil can be wrapped around the exposed parts of the system to shield them from external radio-frequency (RF) interferences. In addition, the sensors have to be covered to prevent the exposure to light. The incident photons may deposit enough energy to increase the leakage current of the detector, which produces unwanted results.

The measurements using diamond that are explained in these chapters have been carried out using several measurement setups, but they are all similar in terms of the electrical signal chain. The measurement chain consists of three main parts: a diamond sensor, a signal preamplifier and a readout device, as seen in figure 3.1. The signals propagating along the analogue chain are fast – in the GHz bandwidth range – and with low amplitudes – of the order of tens of  $\mu\text{V}$ . This gives rise to the importance of RF shielding. Also, the connection between the carrier and the preamplifier has to be as short as possible to avoid capacitive signal losses in the transmission line. Finally, the system needs to be grounded properly.

### 3.1.1 Preamplifiers

Two preamplifiers are used for the measurements, one sensitive to charge and the other to current. *CIVIDEC Cx* (figure 3.2a) is a charge sensitive amplifier. Its high SNR is achieved due to a low equivalent noise charge of  $300 \text{ e}^-$  with an additional  $30 \text{ e}^-$  per each pF of the sensor capacitance. A reported gain of  $\sim 12 \text{ mV/fC}$  makes it a good choice for spectroscopic measurements with diamond sensors. *CIVIDEC C2* (figure 3.2b) is a fast current preamplifier with a 2 GHz bandwidth limit. It is used for TCT measurements because of its fast response and a good SNR. Both are embedded in an RF-tight aluminium box to reduce the noise pickup. Both have an AC coupled input and an output with a  $50 \Omega$  termination.

A 2 GHz bandwidth limit defines the minimum rising time equal to  $t_r \simeq \frac{0.34}{BW} = \frac{0.34}{2 \times 10^9} = 170 \text{ ps}$ , therefore the system with a CIVIDEC C2 amplifier is capable of measuring pulses

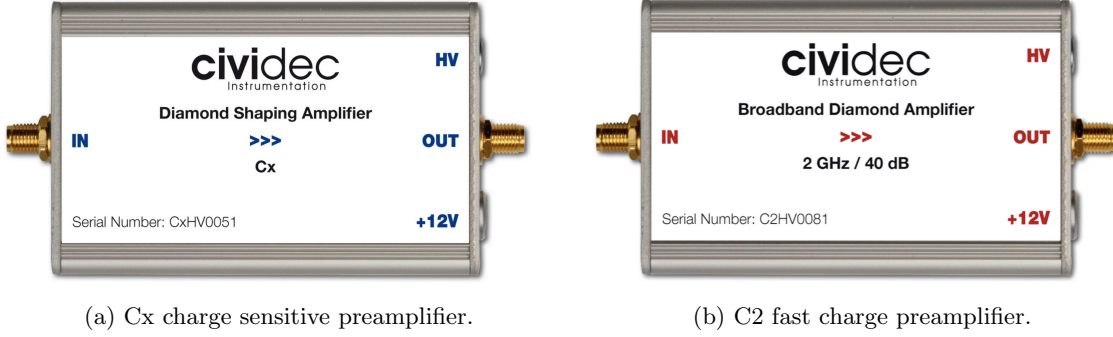


Figure 3.2: Amplifiers used for the charge and current measurements.

with a minimum  $\text{FWHM} \simeq 170 \text{ ps}$ . The initial peak in the  $\alpha$  pulse has a lower FWHM; for example, if a charge carrier travelling through the bulk takes  $t_1 \sim 6 \text{ ns}$  to reach the electrode on the opposite side ( $d_1 \sim 500 \mu\text{m}$ ), the carrier with the opposite charge and a shorter path to the closer electrode – max.  $d_2 \sim 10 \mu\text{m}$  – only takes  $t_2 \sim \frac{d_2}{d_1} t_1 = 120 \text{ ps}$ . A drift time this short induces a current pulse that is too narrow for the system to observe.

### 3.1.1.1 Calibration

The amplifiers have to be calibrated before use to determine their gain. Both are calibrated using a square signal generator with a known amplitude step of  $U_{\text{in}} = (252 \pm 5) \text{ mV}$ . A 2 GHz oscilloscope with a 10 GS/s sampling rate is used to carry out the calibration.

**Cx charge sensitive amplifier** calibration necessitates an injection of a well known charge. Therefore the signal from a pulse generator is routed through a capacitor with a calibration capacitance  $C_{\text{cal}} = (0.717 \pm 0.014) \text{ pF}$  and then to the input of the amplifier. The pulse area behind the capacitor is  $a_{\text{cal}} = (5.0 \pm 0.5) \text{ pVs}$ , with the signal amplitude on the output amounting to  $U_{\text{Cx}} = (1.95 \pm 0.05) \text{ V}$ . The input voltage step combined with the calibration capacitance yields a calibration charge

$$Q_{\text{cal}} = C_{\text{cal}} \cdot U_{\text{in}} = (181 \pm 5) \text{ fC}. \quad (3.1)$$

The gain of the Cx amplifier when comparing the integrated input charge to the output amplitude is

$$A_{\text{Cx}}^Q = \frac{U_{\text{Cx}}}{Q_{\text{cal}}} = (9.3 \pm 0.4) \text{ mV/fC} \quad (3.2)$$

whereas the factor between the area of the input current pulse and the output amplitude is

$$A_{\text{Cx}}^a = \frac{U_{\text{Cx}}}{a_{\text{cal}}} = (390 \pm 40) \text{ mV/pVs}. \quad (3.3)$$

The area-based amplification factor  $A_{\text{Cx}}^a$  can be used as an estimate for the integrated charge of a current pulse. However, it has a higher uncertainty ( $\sim 10 \%$ ) than the amplitude-based factor  $A_{\text{Cx}}^Q$  ( $\sim 4 \%$ ) due to the measurement limitations of the oscilloscope.

### 3.1. MEASUREMENT SETUP

---

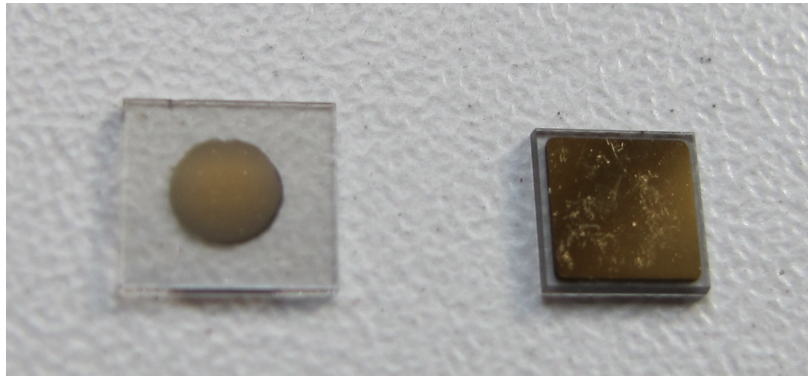


Figure 3.3: Two scCVD diamond samples: A IIa 1scdhq (left) and an E6 S37 (right).

**C2 current amplifier** calibration only requires the measurement of the amplitude gain. To keep the output signal amplitude within the  $\pm 1$  V linear range of the amplifier, the input signal amplitude has to be minimised. The signal from the generator is therefore routed through a 36 dB attenuator to decrease its amplitude to  $U_{\text{inAtt}} = (3.95 \pm 0.05)$  mV. Two amplifiers with different gains have been measured, because both are used for the measurements. The output of the first amplifier amounts to  $U_{\text{C2-1}} = (860 \pm 5)$  mV. This yields the amplification gain

$$A_{\text{C2-1}} = \frac{U_{\text{inAtt}}}{U_{\text{C2-1}}} = (217 \pm 3). \quad (3.4)$$

The second amplifier has the output equal to  $U_{\text{C2-2}} = (632 \pm 5)$  mV with the resulting gain of  $A_{\text{C2-2}} = (152 \pm 3)$ .

#### 3.1.2 Diamond samples

Detector-grade diamonds are very difficult to produce. The major challenge is to ensure a high enough purity of the lattice. The sensor samples used for these studies have been acquired from Element Six (E6) [47]. They all have the same standard dimensions. sCVD diamonds with dimensions  $4.7 \times 4.7$  mm $^2$  are already sufficiently large for most of the beam monitoring applications and still affordable. One sample with dimensions of  $5.6 \times 5.3$  mm $^2$  produced by IIa Singapore [48] has also been characterised at CERN [49]. The target thickness for all samples is 500  $\mu\text{m}$ . Diamonds this thick yield a high enough signal-to-noise ratio for MIPs to be measured by the available electronics. Table 3.1 shows all the samples used for this study. Two of them are measured before and after irradiation and then compared. Irradiation doses for damaging the material need to be high – above  $10^{12}$  particles per cm $^2$  to be able to observe a significant change in behaviour of a diamond sensor.

Name	Type	Producer	Dimensions [mm <sup>2</sup> ]	Thickness [μm]	Electrode	Irradiated
S37	sCVD	E6	4.7 × 4.7	548	Cr/Au	no
S50	sCVD	E6	4.7 × 4.7	537	Cr/Au	no
S52	sCVD	DDL	4.7 × 4.7	515	DLC/Pt/Au	$3.63 \times 10^{14} \frac{\pi}{cm^2}$
S79	sCVD	E6	4.7 × 4.7	529	Cr/Au	$1 \times 10^{14} \frac{\pi}{cm^2}$
ELSC	sCVD	E6	4.7 × 4.7	491	Cr/Au	no
1scdhq	sCVD	IIa	5.6 × 5.3	460	Cr/Au	no

Table 3.1: Diamond sensor samples used.

The diamond samples have quoted impurity densities of  $\leq 2 \times 10^{14} \text{ cm}^{-3}$  and nitrogen incorporation of  $\leq 10^{-9}$ . The electrodes were added by various companies and institutes. For instance, S52 was metallised by a company DDL (now defunct) while the Physics Department of the University of Firenze, Italy metallised the S79. There are also several techniques for producing the electrodes. The DDL contacts consist of three layers: DLC (diamond-like carbon)/Pt/Au with 4/10/200 nm thicknesses, respectively. The metallisation for S79, on the other hand, is made up of Cr/Au with a total thickness of  $\sim 400$  nm. The area coverage also differs from sample to sample. Diamonds must not be metallised until the very edge as the proximity of contacts with a high potential may lead to sparking. However, the areas not covered by the metallisation are less efficient because the fringe fields at the edges are not as strong as in between the electrodes. This effectively reduces the sensitive area of the sensors. In the diamonds used here the effective area is anywhere from 9 mm<sup>2</sup> to 18 mm<sup>2</sup>. The leakage current is below 1 nA, but increases for the irradiated samples. The capacitance is of the order of (2.0±0.3) pF.

### 3.1.3 Readout devices

Electrical signals in diamond detectors are in the GHz frequency range. To preserve the information in the signals, the readout device with a high bandwidth limit must be used. For instance, a 250 MHz limit is enough for the spectroscopic measurements with the Cx charge amplifier, but might be insufficient for the current measurements with the C2 amplifier.

Two devices are used take data shown in this chapter. The first choice is a 2 GHz LeCroy WaveRunner 204MXi-A. This specific model has a sufficiently high bandwidth limit for the fast current preamplifier signals. It offers a reliable solution for analogue signal readout of limited amounts of data. However, its slow acquisition speed is a bottleneck in a test beam experiment. Its initial 100 Hz readout rate decreases to a mere 20 Hz within 20 minutes, because every single trigger is saved as a separate file and the Windows operating system is not capable of handling 10000+ files in a single directory easily. This is why it has been exchanged with a DRS4 [50], an analogue readout device developed by PSI, Switzerland. This compact device is capable of recording up to four waveforms at a time at a steady rate of up to 500 Hz. Its 700 MHz bandwidth limitation is sufficient for the signal from the charge amplifier.

### 3.1.4 Setup for the $\beta$ detection efficiency study

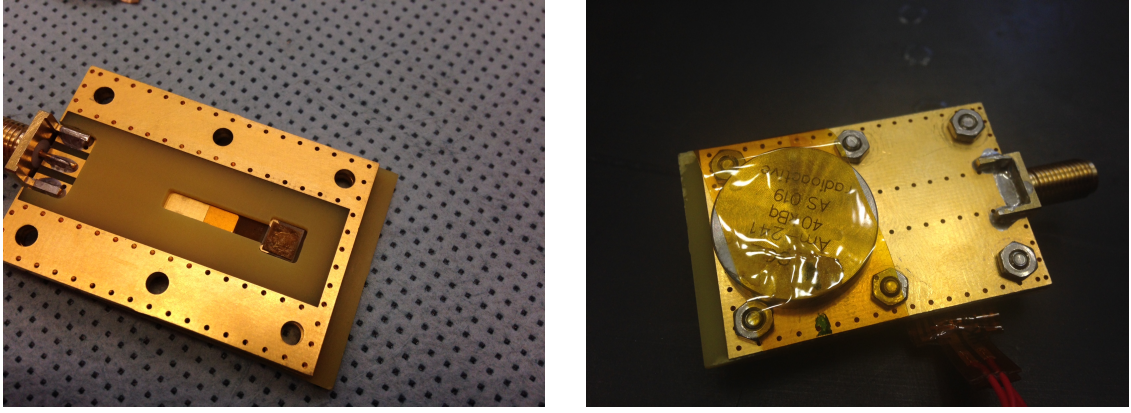
The efficiency study of the diamond sensors has been carried out at CERN in the North Hall test beam facility. There a straight high-energy particle beam of 120 GeV  $\pi$  is provided to the users to calibrate their detectors. The beam has a transverse spread of  $\sigma = 10$  mm in both axes. The particle rate is of the order of  $10^4 \pi \text{ cm}^{-2} \text{ s}^{-1}$ . A diamond sensor embedded in a printed circuit board (PCB) carrier has been placed in the beam spot perpendicular to the beam and connected via an SMA connector directly to a charge amplifier. The amplified signal is read out using a LeCroy oscilloscope and a DRS4 analogue readout system. A computer is used as a controller and data storage for the readout device. A beam telescope is used as a reference detector. It is a device that helps to cross-check the measurements of the devices under test (DUTs) and to carry out spatially resolved studies on the DUTs. It consists of several pixellated sensor planes placed in series, which can track a particle's trajectory with a precision of a few  $\mu\text{m}$ . The sensor planes are positioned in front of the DUT and behind it. Then the beam telescope acts as a trigger system – it triggers the readout of both the telescope data and DUT data when both the planes in front and behind the DUT record a hit by an incident particle. A particle detected by all the planes within the DUT window and the DUT itself counts towards its efficiency whereas a hit missed by the DUT means that the DUT is not 100 % efficient. To discard the hits that miss the DUT completely, a region of interest (ROI) can be chosen in the beam telescope planes. The equation for calculating the sensor efficiency is therefore

$$\epsilon = \frac{N_{\text{DUT}} \wedge N_{\text{telescope}}}{N_{\text{telescope}}} \quad (3.5)$$

for an ROI smaller than the sensitive region of the diamond.

### 3.1.5 Room temperature $\alpha$ -TCT setup

This TCT study is a follow-up of an extensive diamond TCT study at cryogenic temperatures [28]. The room-temperature TCT measurements have been carried out in the laboratory. The setup consists of a diamond sensor embedded in a PCB carrier, a current amplifier and an oscilloscope. To measure  $\alpha$  particles, their energy loss during their trajectory has to be minimised. Therefore the diamond is placed inside a vacuum chamber. The chamber is a steel tube with a diameter of 5 cm. On one side it is connected to a vacuum pump via a steel hose. A feedthrough with an SMA connector is placed on the other side. A CIVIDEC C2 current amplifier is connected directly onto the feedthrough. The amplified output is connected to the oscilloscope via an SMA cable. An  $^{241}\text{Am}$  source with a diameter of 2 cm and a height of 0.5 cm is fixed onto the sensor carrier (figure 3.4a, figure 3.4b). Then the carrier is inserted in the chamber and fixed in place using an air-tight clamp. The pump can then be switched on. It is capable of providing the inside pressure as low as  $10^{-4}$  mbar after approximately one hour of operation.



(a) PCB carrier with an embedded diamond sample. (b) Radioactive source over the carrier.

Figure 3.4: Positioning of the  $\alpha$ -source on top of the sensor carrier.

### 3.1.6 Cryogenic $\alpha$ -TCT setup

The experiment at cryogenic temperatures has been carried out at the Central Cryogenic Laboratory at CERN. The room-temperature TCT setup has to be modified to allow for measurements at temperatures as low as 2 K. It consists of three parts:

1. a cryostat – a thermally insulated cylinder containing liquid helium,
2. an inlet – an air-tight mechanical tube with valves and feedthroughs at the top that is lowered in the liquid helium and
3. the diamond sample embedded in a PCB carrier with a fitted temperature sensor, a heater and cables leading to the feedthroughs.

The setup is described in detail in [28].

When the diamond sample is placed in the PCB carrier and the  $^{241}\text{Am}$  source is in place, the inlet is sealed and lowered in the empty cryostat. Then the inside volume of the inlet is evacuated down to  $10^{-5}$  mbar while the liquid helium is flowing into the cryostat. To improve the thermal contact between the diamond and the coolant, a small amount of helium gas is added inside the evacuated inlet, setting the vacuum to around  $10^{-3}$  mbar. This value changes with time, because the gas condenses on the walls of the inlet, reducing the number of floating particles. For this reason the helium gas has to be added on an irregular basis. Every addition causes a significant undershoot of the sample temperature, which has to be corrected for using a heater placed on the back of the PCB carrier. Also, the added gas deteriorates the vacuum inside the inlet. Furthermore, at approximately 60 K the helium gas has to be evacuated from the inlet to avoid a potential explosion due to the expansion of the gas with temperature.

When the sample is cooled to 4.2 K, the minimum temperature achievable by means of liquid helium without over-pressurising it, the measurements can begin. A temperature

### 3.2. CHARGED PARTICLE PULSES AND SPECTRA

---

sensor placed on the back of the PCB carrier is used to measure the temperature of the sample. After every temperature data point, the current through the heater placed in the PCB next to the diamond sample is increased, increasing the sample. The initial temperature time constant of the order of tenths of seconds at low temperatures increases with temperature. Even more so when helium is evacuated from the inlet at 60 K, removing the thermal bridge between the wall of the inlet and the diamond sample. At the room temperature (RT), the time constant is already of the order of minutes.

## 3.2 Charged particle pulses and spectra

In previous chapter the ionisation profiles for different types of radiation were discussed.  $\beta$  radiation induces a triangular electric pulse whereas  $\alpha$  radiation induces a rectangular one. However, their amplitude, width and rise/fall time depend heavily on the type of interaction with the diamond, the purity of the diamond and the bandwidth of the amplifier and the oscilloscope. This section shows the signal pulses of  $\alpha$ ,  $\beta$  and  $\gamma$  radiation with their respective energy distributions for the case of a diamond detector.

Figure 3.5 shows a set of pulses and an averaged waveform for 5.5 MeV  $\alpha$ , 2.3 MeV  $\beta$  and 1.3 MeV  $\gamma$  radiation using an  $^{241}\text{Am}$ , a  $^{90}\text{Sr}$  and a  $^{60}\text{Co}$  source, respectively. The particles are measured with the non-irradiated sCVD diamond S37.  $\alpha$  particles always produce the same signal pulse, but with a high noise RMS. The averaging suppresses the noise while retaining most the information. It does, however, smear the rising and falling edge, increasing the rising and falling time. The  $t_r$  is now of the order of 0.5 ns. Both  $\beta$  and  $\gamma$  pulses look similar - triangular and with a wide range of amplitudes. Here the pulse count is low, so the pulses with a high amplitude are not recorded. A trigger would need to be set very high to “catch” them with the oscilloscope.

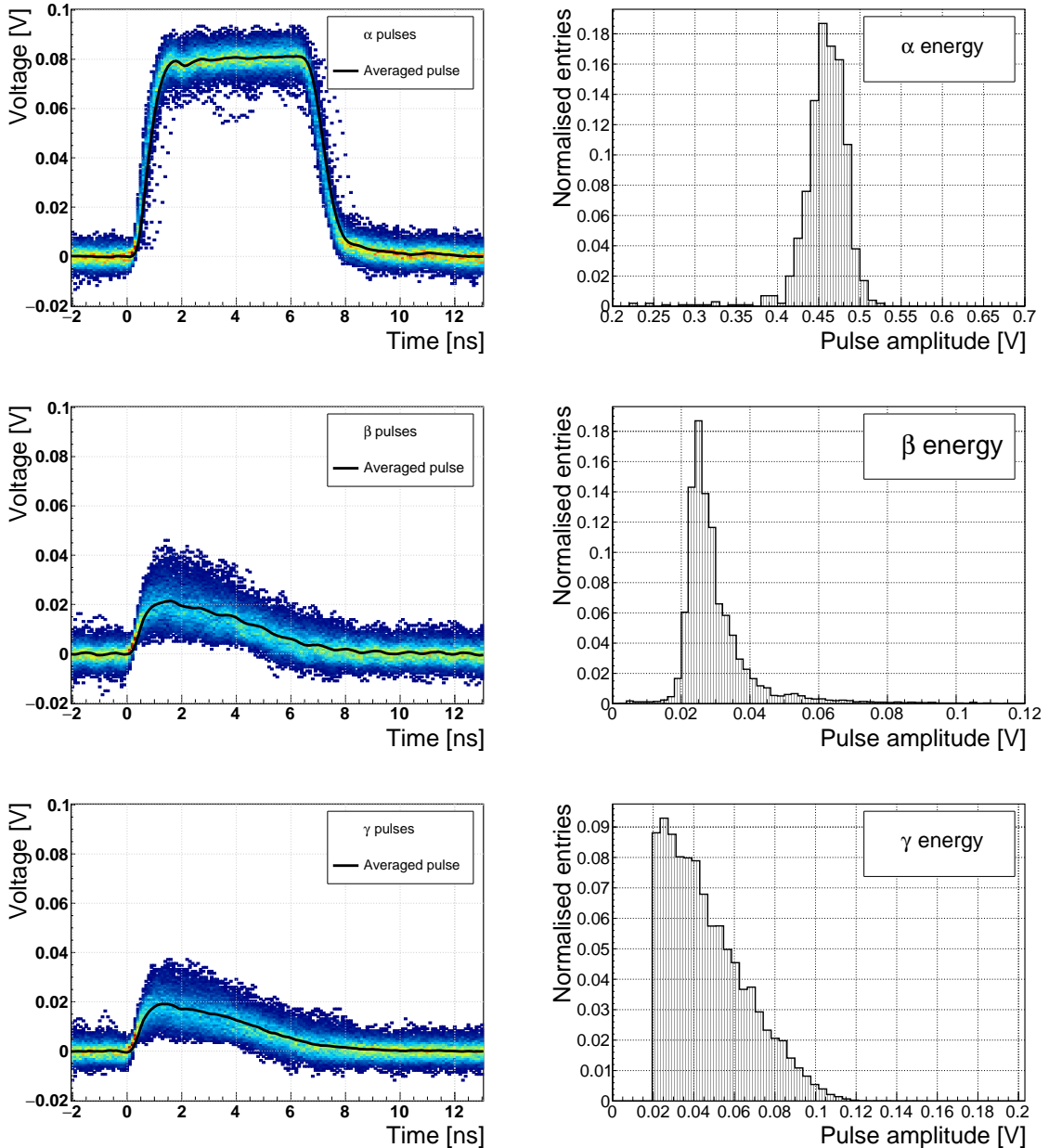


Figure 3.5: Superimposed and averaged pulses (left figures, current amplifier) and distributions of deposited energy (right figures, charge amplifier) for three types of radiation. Note the scale on the X axis of the distributions.

### 3.3 Radiation limitations

This section quantifies the decrease in charge collection efficiency as well as the effects on long-term measurement stability in irradiated sCVD diamonds.

#### 3.3.1 Irradiation study

This subsection contains a study of the effects of 300 MeV pion ( $\pi$ ) irradiation on the charge collection efficiency of sCVD diamond detectors. To carry out this study, two diamond samples were irradiated to doses of  $1 \times 10^{14} \pi \text{ cm}^{-2}$  (S79) and to  $3.63 \times 10^{14} \pi \text{ cm}^{-2}$  (S52). A test beam campaign was carried out to observe the charge collection efficiency at different bias voltage settings. The efficiency values acquired are used to determine the effective drop in efficiency as a function of the received radiation dose. This is to test if the collected charge  $Q$  is inversely proportional to the received dose  $\Phi$ . A procedure defined by a collaboration researching diamond behaviour RD42 has been applied to the measured values to extract the damage factor described in 2.5.

The following subsection contains measurements and results of a long-term stability study using  $\alpha$  and  $\beta$  particles. In particular, the charge collection efficiency with  $\beta$  and  $\alpha$  radiation as a function of time is measured. To investigate this effect on the scale of charge carriers, the change of TCT (transient current technique) pulses with time is observed. Finally, a procedure that improves the pulse shape and with it the charge collection is proposed.

##### 3.3.1.1 Irradiation with a 300 MeV $\pi$ beam

The samples were irradiated at the Paul Scherrer Institute (PSI) [51] by means of a beam of pions with an energy of 300 MeV (kinetic energy 191.31 MeV) and with a flux of up to  $1.5 \times 10^{14} \pi \text{ cm}^{-2}$  per day. The system has a 10 % uncertainty on the beam energy. Looking at the pion damage curve in figure 2.9,  $\pi_{300 \text{ MeV}}$  point (191 MeV kinetic energy) sits on a steep section of the DPA curve. This means that a deviation in beam energy can have a significant effect on the damage in the sensor. In addition, their quoted uncertainty on the measurement of the delivered dose is  $\pm 20\%$ .

Two diamond samples, S52 and S79, were put in the  $\pi_{300 \text{ MeV}}$  beam in the 2014 PSI irradiation campaign; S52 to  $(1 \pm 0.21) \times 10^{14} \pi \text{ cm}^{-2}$  and S79 to  $(3.63 \pm 0.77) \times 10^{14} \pi \text{ cm}^{-2}$ . During the process, the gold electrodes got slightly activated, but the activation decayed in two weeks.

##### 3.3.1.2 300 MeV $\pi$ radiation damage factor

Three diamonds – non-irradiated S37 and irradiated S52 and S79 – were tested in a  $\pi_{120 \text{ GeV}}$  test beam in the SPS North Experimental Area at CERN [52] before and after irradiation. The goal was to estimate the charge collection efficiency and charge collection distance as a function of irradiation dose. The samples were primed (pumped) prior to data taking using

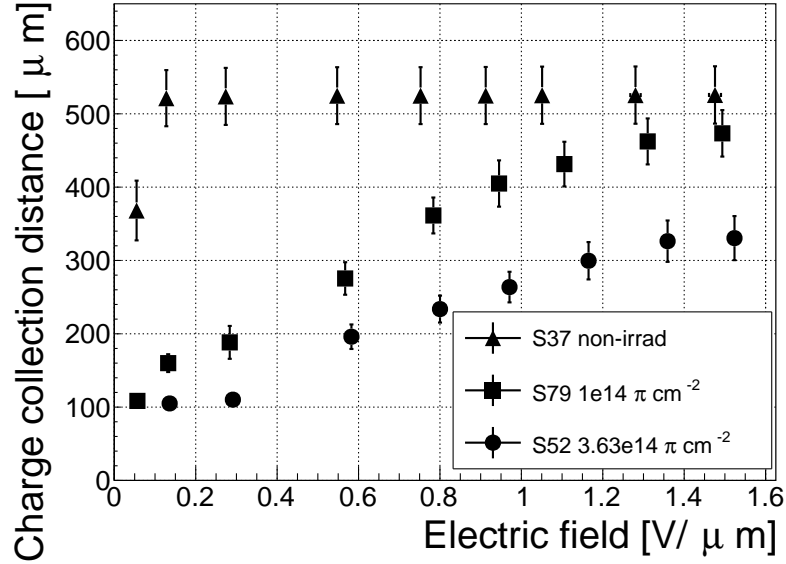


Figure 3.6: The figure shows the CCD for S37, S79 and S52 at a range of bias voltage settings.

a  $^{90}\text{Sr}$  radioactive source. The data were then taken at a range of bias voltages ranging from 30 V to 900 V, yielding between  $0.06 \text{ V}/\mu\text{m}$  and  $1.8 \text{ V}/\mu\text{m}$  electrical field in the bulk. Every data point contained approximately  $5 \times 10^4$  measured particles. The charge deposited by the particles was measured using a CIVIDEC Cx charge preamplifier.

As expected, the integrated amplitude spectrum is a Landau distribution. Its most probable value (MPV) is used to calculate the most probable collected charge  $Q_i$ :

$$Q_i [\text{e}^-] = \frac{1}{1.6 \times 10^{-19}} Q_i [\text{C}] = 6241 \cdot Q_i [\text{fC}] = 6241 \cdot \frac{\text{MPV} [\text{mV}]}{A [\frac{\text{mV}}{\text{fC}}]}, \quad (3.6)$$

where  $A = 9.3 \text{ mV/fC}$  is the preamplifier gain factor and  $1 \text{ e}^- = 1.6 \times 10^{-19} \text{ C}$ .

The CCD for the three measured samples at a bias voltages ranging from  $0.2\text{--}1.6 \text{ V } \mu\text{m}^{-1}$  calculated using equation 2.18 is shown in figure 3.6. S37 exhibits a full collection distance already at  $0.4 \text{ V } \mu\text{m}^{-1}$  whereas the irradiated samples have a more gentle increase of CCD with increasing bias voltage. It is evident that at  $1 \text{ V } \mu\text{m}^{-1}$  the maximum CCD has not been reached in the case of S79 and S52. Nevertheless, to compare the measured data point with those provided by RD42, the CCD at  $1 \text{ V } \mu\text{m}^{-1}$  has to be taken.

The data points with the maximum CCD obtained in the test beam measurements are plotted against received radiation dose in figure 3.7. Equation 2.20 is fitted to the data points and a damage factor  $k_\lambda = (4.4 \pm 1.2) \times 10^{-18} \mu\text{m}^{-1} \text{ cm}^{-2}$  is obtained. The value is for a factor of two higher than the damage factor obtained by RD42. This could be due to an insufficient priming time ahead of the measurement. In addition, the diamond samples have not been polished and re-metallised after irradiation, as is the case for the RD42. Also, with only two samples measured, the statistical uncertainty is high. Nevertheless, it can be

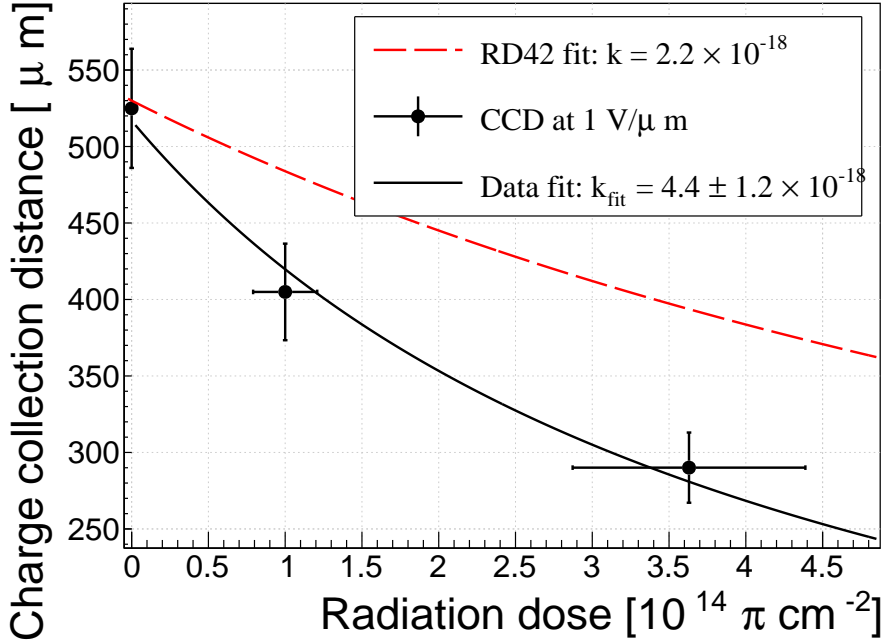


Figure 3.7: The charge collection distance at  $1 \text{ V}/\mu\text{m}$  bias voltage for the three diamond samples is plotted as a function of the received radiation dose. It is compared to the RD42 data for pion irradiation. The data points are about 15–25 % lower than expected from the RD42 data [40].

concluded that the 300 MeV pions damage the diamond bulk significantly more than the 24 GeV protons.

### 3.3.2 Long-term measurement stability

An important requirement for particle detectors is a stable performance over long periods of time. For instance, the charge collection for a defined radiation type and quantity must not change over time or has to change in a predicted way. The stability of diamond detectors depends on many factors, e.g. material purity, polishing process, electrode material, irradiation damage etc. The aim is to study the behaviour of diamond under controlled conditions, with the goal to understand its limitations. One of these limitations is the received radiation dose as it can affect the long-term stability of the sensor during operation.

The three diamond samples (S37, S79 and S52) have been exposed to two different types of ionising radiation for a longer period to see if their behaviour changes over time. Two parameters have been observed in particular:

1. Charge collection of  $\beta$  particles and
2. Charge collection and ionisation profile of  $\alpha$  particles.

### 3.3.2.1 $\beta$ long-term stability

The diamond samples have undergone a long-term stability test at room temperature using  $\beta$  radiation. This has been done using a  $^{90}\text{Sr}$  source emitting  $\sim 2.28$  MeV electrons at a rate of approximately  $10^4 \text{ e}^- \text{ cm}^{-2}$ . To simulate the initial conditions in HEP experiments, the sensors must not be primed before starting the measurements. The measurement setup consists of a diamond sample (S37, S52 or S79) with the CIVIDEC Cx spectroscopic amplifier, a silicon diode with a CIVIDEC C6 amplifier for triggering and a  $^{90}\text{Sr}$  source on top. A particle emitted by the source traverses the sensor bulk and hits the silicon diode, triggering the analogue signal readout. The source is left on the top for the course of the experiment. The measurements, however, are taken at discrete times. For every data point, approximately  $10^4$  triggers have to be recorded. The offline analysis of the recorded signal pulse amplitudes yields a Landau distribution for every data point. The current charge collection relative to the initial charge collection for every sample is plotted as a function of the received  $\beta$  dose in figure 3.8. It shows that, for the irradiated samples, the charge collection efficiency improves when the diamond sensor is primed with a  $\beta$  source. The effect is negligible for the non-irradiated high-quality S37. Both relative increases are significant – 22 % for S79 and 55 % for S52. At a received dose of approximately  $4 \times 10^6$  particles the charge collection is stabilised. At that point S79 achieves close to a full efficiency (in absolute values – not shown) whereas S52 reaches approximately 50 %.

The  $\sim 2.28$  MeV electrons emitted by this source are not MIPs; their charge deposition is higher than that of an electron MIP, according to the Bethe-Bloch distribution [53]. Nevertheless, for the purpose of these measurements this energy is adequate since only the relative change in charge collection is of interest.

To sum up, diamond provides a stable measurement of the  $\beta$  radiation detection after reaching a stable state. Even if damaged by radiation, it reaches a stable charge collection at a received dose of  $\sim 4 \times 10^6$  MIPs. Its efficiency decreases with a high irradiation dose. However, the decrease can be accounted for if the damage factor and the rate and energy of the particles are known.  $\gamma$  radiation has a similar impact on the diamond as the  $\beta$ . The incident photons, if they interact with the diamond, prime the bulk, increasing the charge collection efficiency. The difference, however, is that the interaction probability (cross-section) is lower for gammas [54, 55].

### 3.3.2.2 $\alpha$ long-term stability

This part discusses the stability of irradiated diamond sensors during  $\alpha$  measurements. An  $^{241}\text{Am}$  source has been used, emitting  $\alpha$  particles with a mean energy of 5.5 MeV.

To test the stability of the diamond during  $\alpha$  measurements, the samples have been biased at +500 V and exposed to up to 8000  $\alpha$  hits while measuring their charge collection efficiency using the CIVIDEC Cx spectroscopic amplifier. The charge collected at every measurement point  $Q(\Phi)$  is compared to collected charge of the first measurement  $Q(0)$ . The resulting ratio  $\frac{Q(\Phi)}{Q(0)}$  for all samples is shown in figure 3.9. Each measurement point is

### 3.3. RADIATION LIMITATIONS

---

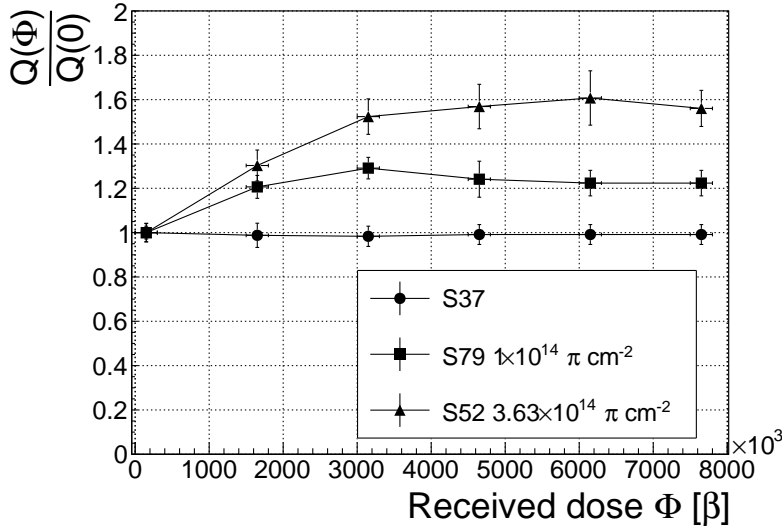


Figure 3.8: Relative increase of charge collection over time due to priming with the  $^{90}\text{Sr}$  radioactive source. The charge collection for the non-irradiated S37 stays constant. The bias voltage for this measurement is  $1 \text{ V}/\mu\text{m}$ .

an average of 30 consecutive  $\alpha$  hits. The observations are the following:

- $Q(\Phi)$  for the non-irradiated S37 is stable as compared to  $Q(0)$  over the course of the measurement.
- The initial efficiency of the irradiated S52 and S79 starts decreasing already at a low  $\alpha$  count.
- The charge collection efficiency of the unprimed irradiated samples drops much faster than after priming.
- The particle count rate decreases with decreased efficiency, which is clearly seen in the unprimed S52 data where the data points at a low efficiency are much further apart.

The absolute values are not shown here because only the relative drop is of interest in the scope of the long-term stability tests.

$\alpha$  affect the irradiated diamond differently than when subjected to  $\beta$  radiation. This can be due to several contributions:

**Quantity of deposited energy.** The deposited energy on its path produces 24 times more e-h pairs than that of a MIP, according to equations 2.16 and 2.15. Such a difference may affect the charge collection efficiency due to saturation.

**A point-like charge carrier creation.** The energy of an  $\alpha$  particle is deposited in a small volume –  $14 \mu\text{m}$  in depth and  $\sim 20 \text{ nm}$  radially [28]. A dense distribution of charge carriers might affect their behaviour at the start of the drift.

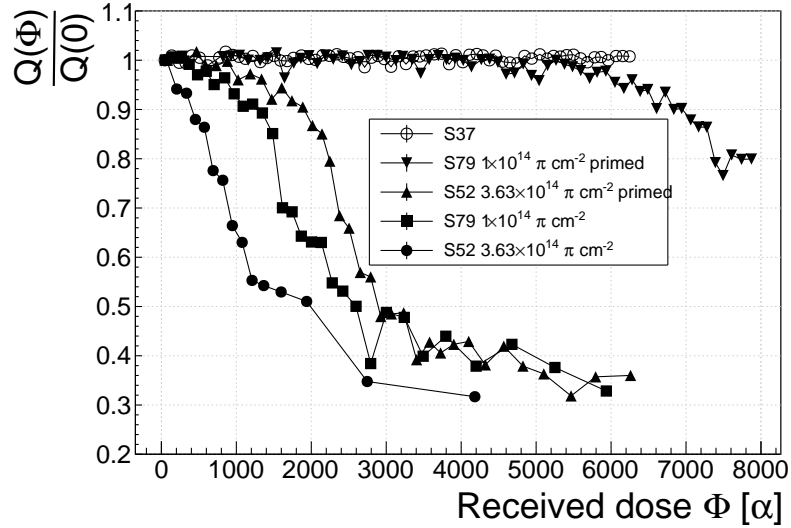


Figure 3.9: A relative drop in charge collection efficiency as a function of the received  $\alpha$  dose for non-irradiated and irradiated diamond samples.

**Single-polarity charge carriers.** Carriers of only one polarity drift through the sensor while those of the opposite polarity almost instantly reach the adjacent electrode. Therefore the charges only one polarity get trapped along the drift path, contributing to a single-polarity space-charge build-up.

To investigate this sudden drop in efficiency, the current pulse shapes using a CIVIDEC C2 current amplifier have to be observed, as shown in figure 3.10. The shape of the pulse holds more information about the charge carrier properties in the sensor than solely the value of the integrated charge. This time only the primed S79 sample has been tested. Both the hole and the electron collection are observed to determine whether they behave differently or not.

The first observation of the raw acquired data in figures 3.10 is that the initially stable pulses start deteriorating; several different shapes start appearing gradually, some still very similar to those from the beginning while the others with almost zero amplitude.

A more dedicated analysis of the first observation has been carried out as follows: at the beginning of the test when the diamond is still operating stably, 60 pulses are recorded. An average pulse is calculated. This is a reference pulse for the subsequent measurement points. Then an RMS of the individual pulses  $\sigma_n$  with respect to the reference pulse is calculated and the resulting RMS values are summed together into  $\sigma_{\text{ref}}$ :

$$\sigma_{\text{ref}} = \sum_{n=1}^{60} \sigma_n. \quad (3.7)$$

All the subsequent data points also consist of a set of 60 pulses. At every data point the summation of the RMS values of the individual pulses with respect to the initial averaged

### 3.3. RADIATION LIMITATIONS

---

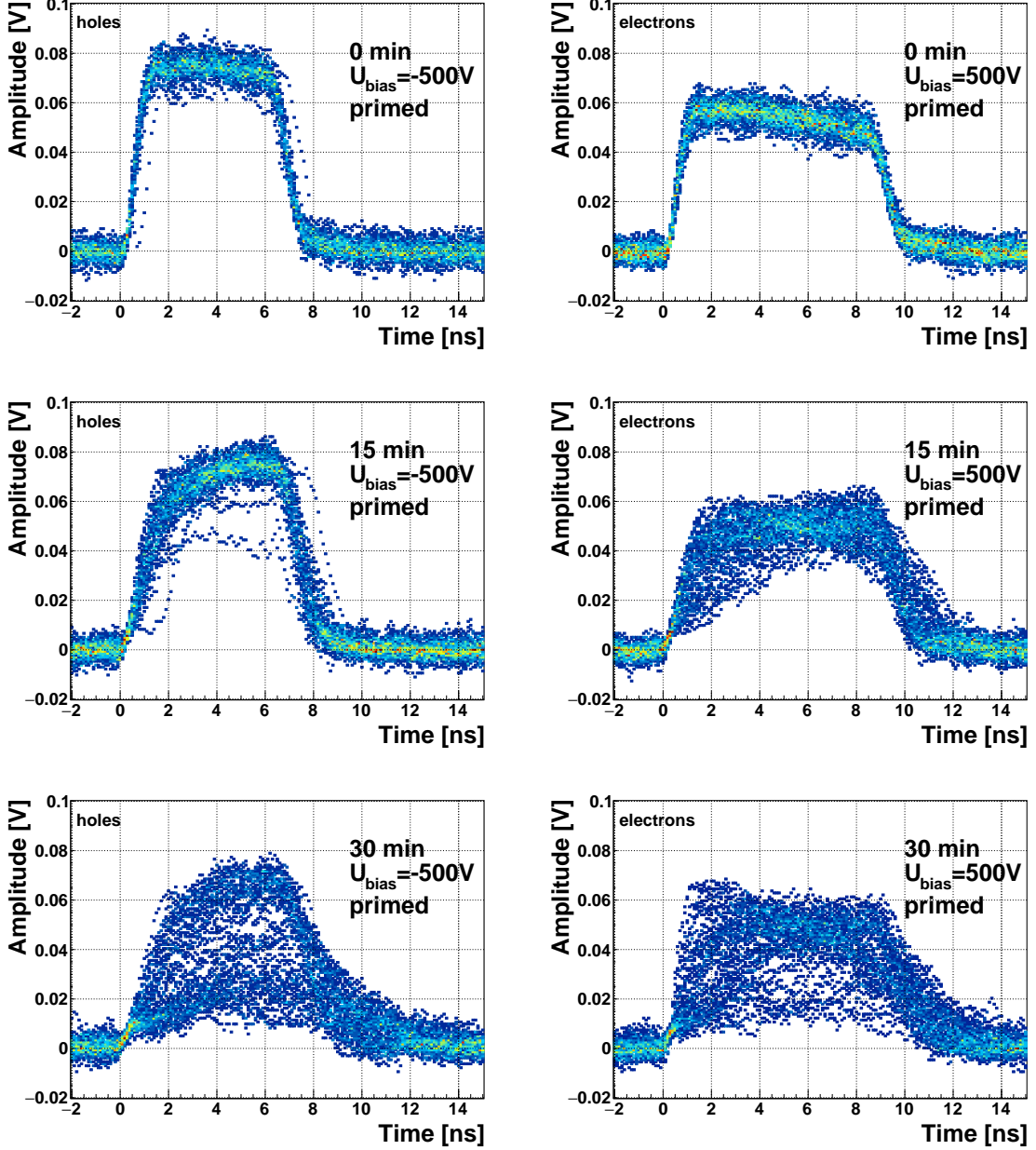


Figure 3.10: The signal of the irradiated and primed S79 deteriorates with time for both polarities. Every plot contains 60 superimposed pulses.

pulse  $\sigma$  is calculated according to equation 3.7. The ratio between the initial  $\sigma_{\text{ref}}$  and discrete values  $\sigma$  gives a measure of the change of the pulse shape with respect to the reference pulse at the start of the measurement. Therefore the initial value is 1 and it decreases if the RMS values of subsequent data points are higher. Figure 3.11 shows the ratio  $\frac{\sigma_{\text{ref}}}{\sigma(\alpha \text{ dose})}$ . From the data obtained it can be concluded that the initial pulse shape quickly starts deteriorating. In fact, the deterioration of the shape follows an approximate exponential decay function, which can be fitted to the data. The resulting decay constants

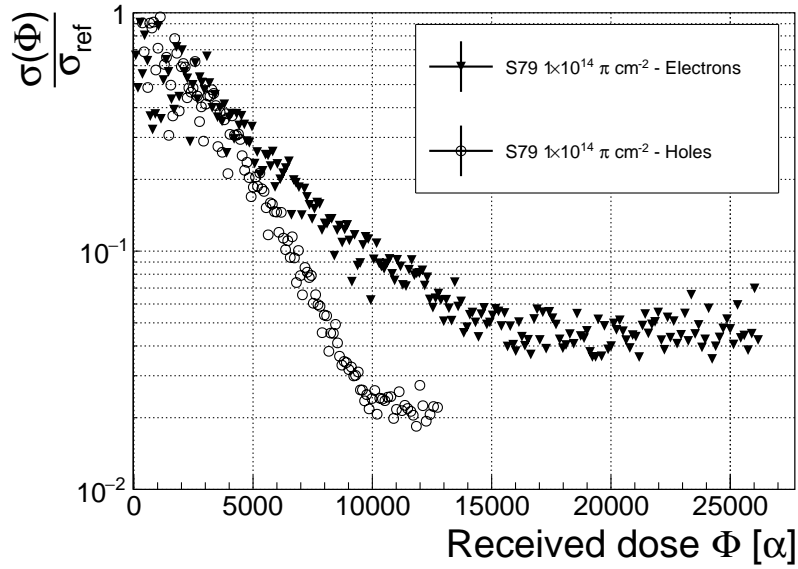


Figure 3.11: Deterioration of the pulse shapes with time.

for electrons and holes are  $\tau_e = (4400 \pm 150) \alpha^{-1}$  and  $\tau_h = (3300 \pm 140) \alpha^{-1}$ . The electrons retain the initial shape for longer. The deteriorated shapes also seem to be for a factor of 2 better than those of the holes.

**Discussion** One hypothesis is that this behaviour is caused by space-charge build-up. Charge carriers get stopped in the charge traps in the bulk for a long time, building up regions of space-charge. The built up space-charge affects the electric field. The field in turn affects the drifting charge carriers, slowing them down or speeding them up, depending on the field gradient. Since the movement of the carriers is inducing the electric current, the field gradient can be observed in the current signal.

The fact that the signal shapes vary significantly might be due to a very non-uniform electric field, which is created by the three competing processes discussed above. The charge carriers are created in a small volume whereby some immediately get trapped, some recombine to form excitons ?? and others start drifting. The remaining charge carriers drift towards their respective electrodes. Both are trapped on their way, causing the space-charge build-up of one polarity on the first 14  $\mu\text{m}$  and of the other polarity all along the sensor thickness. A resulting electric field is very non-uniform, which explains the unstable current pulses.

**Restoring the pulse shapes** Finally, an effort has been made to find a way for the pulse shapes to return to their initial state. Five methods are listed:

1. No source, with bias voltage,
2. No source, without bias voltage,
3. Priming with  $\gamma$  at a rate of  $400 \text{ s}^{-1}\text{cm}^{-1}$  without bias voltage,

### 3.3. RADIATION LIMITATIONS

---

4. Priming with  $\beta$  at a rate of  $1000 \text{ s}^{-1}\text{cm}^{-1}$  with bias voltage and
5. Priming with  $\beta$  at a rate of  $1000 \text{ s}^{-1}\text{cm}^{-1}$  without bias voltage.

Before starting each method, the diamond sample S79 is first primed using a  $^{90}\text{Sr}$  source for approximately one hour. Then the bias voltage is switched on and an  $^{241}\text{Am}$  source is put on top. The pulses produced by the incident  $\alpha$  particles have a proper rectangular pulse at the beginning, but then start changing – first gradually and later increasingly more in an erratic way, as described in the text above. After approximately 30 minutes, one of the methods is tested. When a “healing” procedure is started, a set of 60 pulses is taken at irregular points of time to observe the change in the pulse shape and to assess the quality of the “healing” procedure. Then the bias voltage is switched off and the sample is primed again to reset its state before starting with the next run.

The results depicted in figure 3.12 show that the methods (3) and (5) improve the shape, method (2) helps slowly, (1) does not show any change with time and (4) at first improves, but then significantly degrades the shape. The effect observed in method (4) has already been described in [56]. The “healing” process therefore depends on the rate of radiation, the bias voltage and the time of exposure. The ionising radiation creates free charges, which quickly recombine close to the place of generation. It is likely that they also release the charges trapped during the measurement, reducing the overall effect of the space-charge. The traps get filled with both flavours of carriers, thus they are neutralised. The pulse shape gradually returns to its initial state.

Procedure	Source	Type of radiation	Bias voltage	Effectiveness
1	/	/	ON	no
2	/	/	/	slow
3	$^{60}\text{Co}$	$\gamma$	/	YES
4	$^{90}\text{Sr}$	$\beta$	ON	no
5	$^{90}\text{Sr}$	$\beta$	/	YES

Table 3.2: Effectiveness of healing procedures.

**Summary** The shape of the pulses caused by  $\alpha$  radiation changes with time for irradiated samples. The shape of the pulses gets distorted and becomes erratic. The charge collection decreases and its spread increases. The signal shapes are probably affected by a non-uniform electric field, which is caused by the build-up of space charge. The signal degradation happens even faster for non-primed diamonds. To “heal” the diamond – to bring the pulse shapes back to their initial shape – the sample must be primed using a  $\beta$  or a  $\gamma$  source for several minutes without bias voltage. Switching to the inverse polarity for a few seconds helps a bit, but in a long run distorts the signal, preventing it from returning to the initial shape.

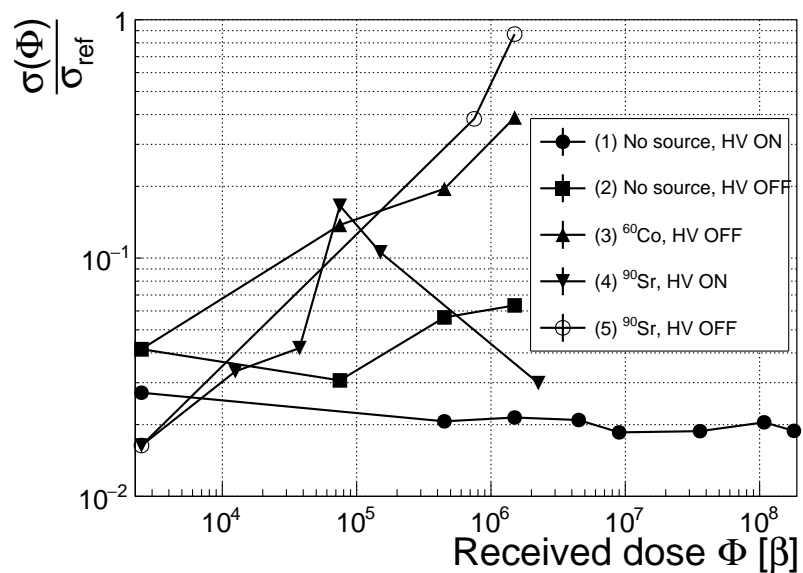


Figure 3.12: Comparison of the five procedures for the “healing” process for an irradiated diamond that had been exposed to  $\alpha$  radiation with a rate of  $10^1 \text{ s}^{-1}$ , with the bias voltage switched on, for at least 30 minutes.

### 3.4. TEMPERATURE LIMITATIONS

---

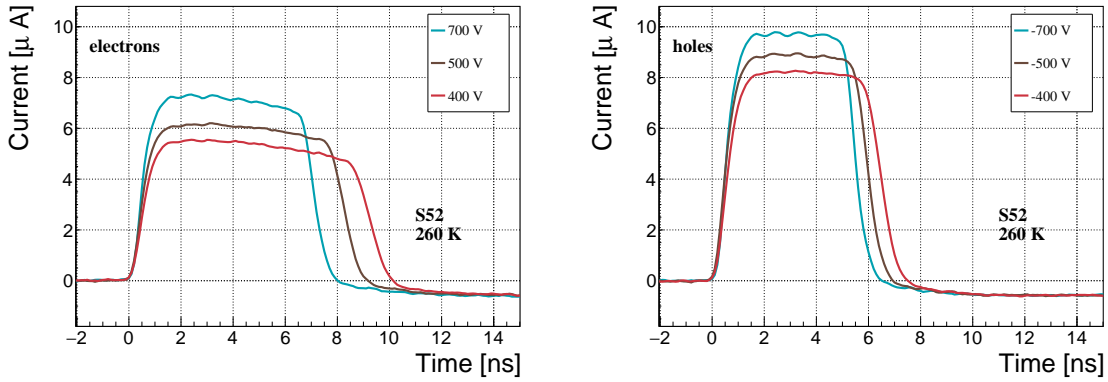


Figure 3.13: Varied bias voltage at a fixed temperature.

## 3.4 Temperature limitations

A test has been carried out to evaluate the effect of temperature changes on the output signal of the diamond sensors. A cryostat filled with liquid helium is used to cool down the sensor during the measurement process. The current signal response to  $\alpha$ -particles is measured at 18 temperature points between 4 K and 295 K. At every temperature point a set of 300 pulses is recorded at various bias voltages. The resulting data show that the charge collection is stable from RT down to 150 K where it starts decreasing. It stabilises again at about one third of the initial value at 75 K. This behaviour was first measured and discussed by H. Jansen [28].

### 3.4.1 Temperature-variant $\alpha$ -TCT before irradiation

Three sCVD diamond samples have been tested at a range of temperatures using the  $\alpha$ -TCT technique. At each temperature point, the bias voltage is set to several positive and negative values. A set of 300 pulses is recorded at every data point and averaged offline. The resulting averaged pulses of sample S37 at the 260 K temperature point and a bias voltage of  $\pm 700$  V,  $\pm 500$  V and  $\pm 400$  V are shown in figure 3.13. The pulses induced by holes as charge carriers are shorter than those induced by electrons, which means that holes travel faster in diamond. The area of the pulse, however, is the same for both polarities, which corresponds to the fact that the same amount of charges is drifting in both cases.

Figure 3.14 shows pulses at a bias voltage set to  $\pm 500$  V across the range of temperatures between 4 K and 295 K. Several conclusions can be drawn by observing their shape. First, the pulse shapes change with decreasing temperature. The pulse time gets shorter and higher, hinting at the faster carrier drift velocity  $v_{\text{drift}}$ . Second, between 150 K and 75 K there is a significant change in shape - the time constant of the rising edge increases significantly and the pulse area decreases. From 75 K down to 4 K there is no significant change. Last, the top of the pulse at the S52 is not flat, which means that a portion of the drifting charge is lost along the way. This is due to charge trapping, likely by means of

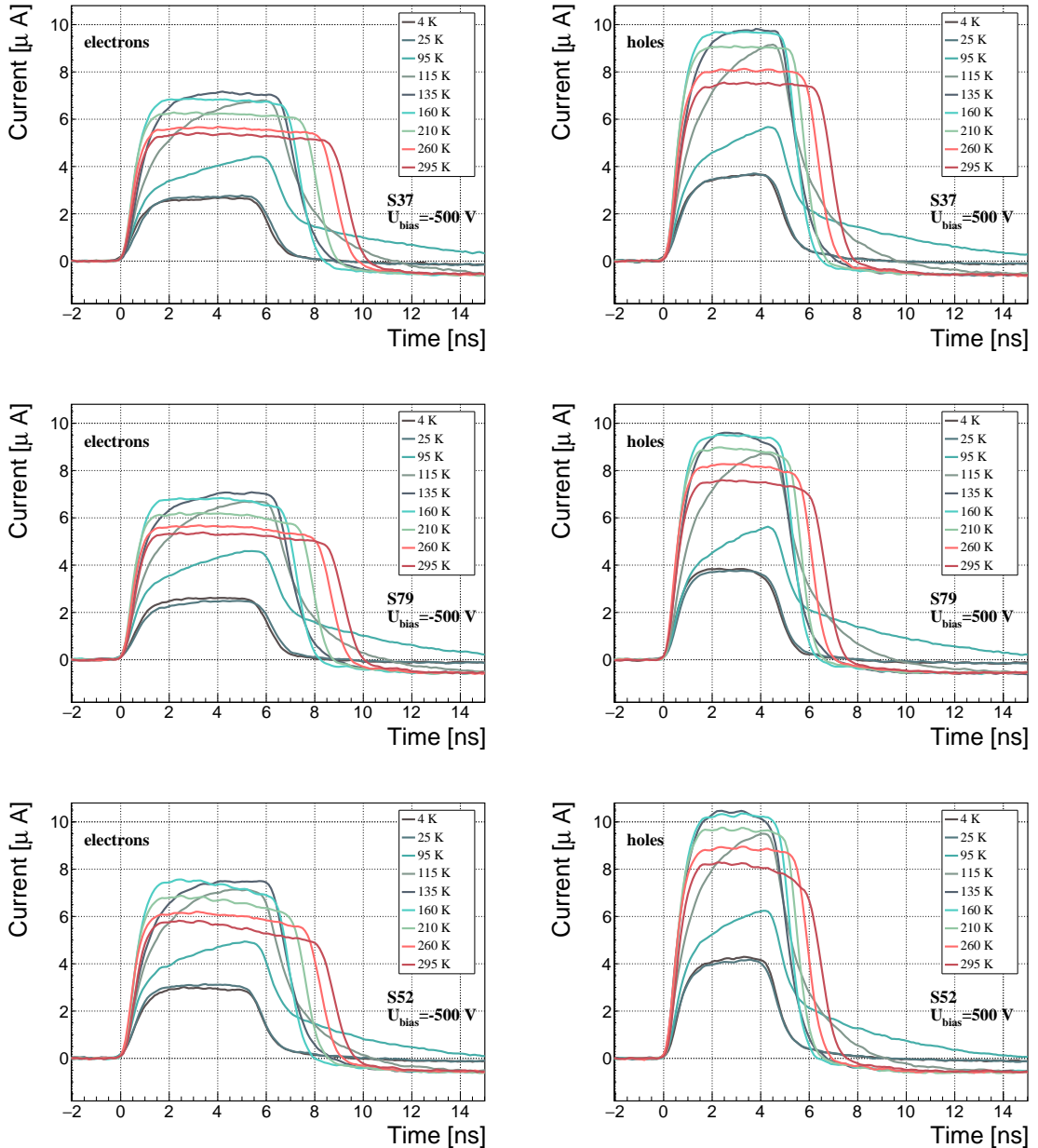


Figure 3.14: Several data points between 4 K and 295 K at a bias voltage of  $\pm 500$  V. The tilted top of the pulse on the bottom left figure is due to built-up space charge.

### 3.4. TEMPERATURE LIMITATIONS

---

crystal defects or impurities.

#### 3.4.2 Temperature-variant $\alpha$ -TCT after irradiation

The irradiated S79 and S52 have been re-tested in the cryostat after irradiation. The aim is to observe how their pulse shapes change with decreasing temperature, in particular the decaying top of the pulses, as shown in figure 3.15. The decay time gives information on trapping of charge carriers while travelling through the diamond bulk. A variation of the decay time constant as a function of temperature might help to reveal the type and depth of the charge traps. To observe these effects or lack thereof, a number of requirements have to be met. First, the diamond samples are intentionally not primed prior to the experiment because priming would improve the pulse shapes and possibly change the decay time constant of the signal. Second, keeping in mind that the pulse shape of irradiated diamonds changes with time, the duration of the measurement of an individual data point has to be short – of the order of 30 seconds. Last, the sequence of the bias voltage settings is important, the reason for which is explained below.

Unfortunately it is not possible to avoid temporal pulse changes. For instance, one measurement point takes approximately one minute. After the measurement, the bias voltage polarity is swapped for a few seconds to bring the diamond back into its initial state. But a few seconds with respect to a minute are not enough, but due to time constraints this cannot be avoided. Therefore when the bias voltage is set to the next value, there is still some residual effect of the previous measurement. Similar to the effects of polarisation, this effect is also decreasing the pulse height. This can be observed in figure 3.15, which shows the resulting pulses of S52 for bias voltages of  $\pm 200$  V,  $\pm 300$  V,  $\pm 400$  V and  $\pm 500$  V at 230 K and 260 K. In this case the measurement sequence is: 230K (200 V, 300 V, 400 V, 500 V, -500 V, -400 V, -300 V), 260 K (-200 V, -300 V, -400 V, -500 V, 500 V, 400 V, 300 V). The changes in pulse shapes for holes at 230 K and 260 K cannot be attributed to the temperature change. Instead, the explanation could lie in diamond “polarisation”. This means that, when exposed to an electric field with  $\alpha$  measurements ongoing, an internal electric field of inverse polarity builds up in the diamond, which effectively reduces the overall electric field. This internal field does not dissipate when the external bias voltage is switched off. The diamond becomes “polarised”. When switching the polarity of the external bias voltage, the internal and external electric field point in the same direction at the beginning, increasing the overall electric field and with it the pulse height. In figure 3.15 this happens when switching from 500 V (figure 3.15a) to -500 V (figure 3.15b) at 230 K. The built up polarisation contributes to the pulse having a sharp rising edge and a high amplitude. This effect decays during the next two voltage points. There would be a handful of ways to avoid this polarisation effect in the data:

1. After every data point invert the bias voltage and leave it to return to a neutral state for the same amount of time,

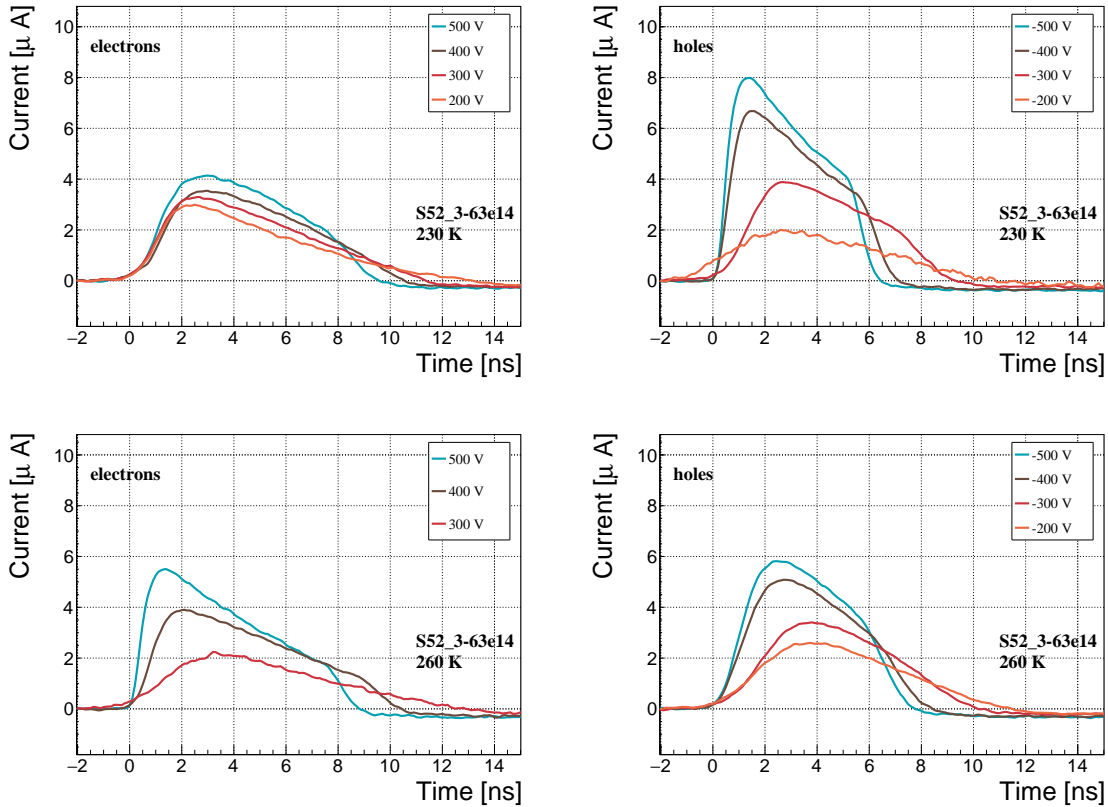


Figure 3.15: Varied bias voltage at a fixed temperature for an irradiated sample.

2. Make a hysteresis of data points, going from minimum negative to maximum positive bias several times,
3. Reduce the measurement time at every bias voltage setting.

Unfortunately, options (1) and (2) are very time consuming and would increase the overall experiment time to over one day. The third option would worsen the resulting averaged pulses. In the end an alternative option has been chosen: alternating the starting bias voltage and the sequence at every temperature point. With this option, a meaningful systematic error in analysing the pulse shapes can be attained.

Figure 3.16 shows the irradiated S52 and S79 as well as the non-irradiated S37 for comparison, all at a bias voltage of  $\pm 500$  V and at several temperature points between 4 K and 295 K. It is evident that the radiation damage affects the shape of the pulses across all temperatures.

### 3.4.2.1 Collected charge as a function of temperature

The collected charge as a function of temperature for electrons and holes is plotted in figures 3.17 and 3.18, respectively. In the framework of this thesis the focus is on the effect in the irradiated devices. The new contribution are the data points for the irradiated

### 3.4. TEMPERATURE LIMITATIONS

---

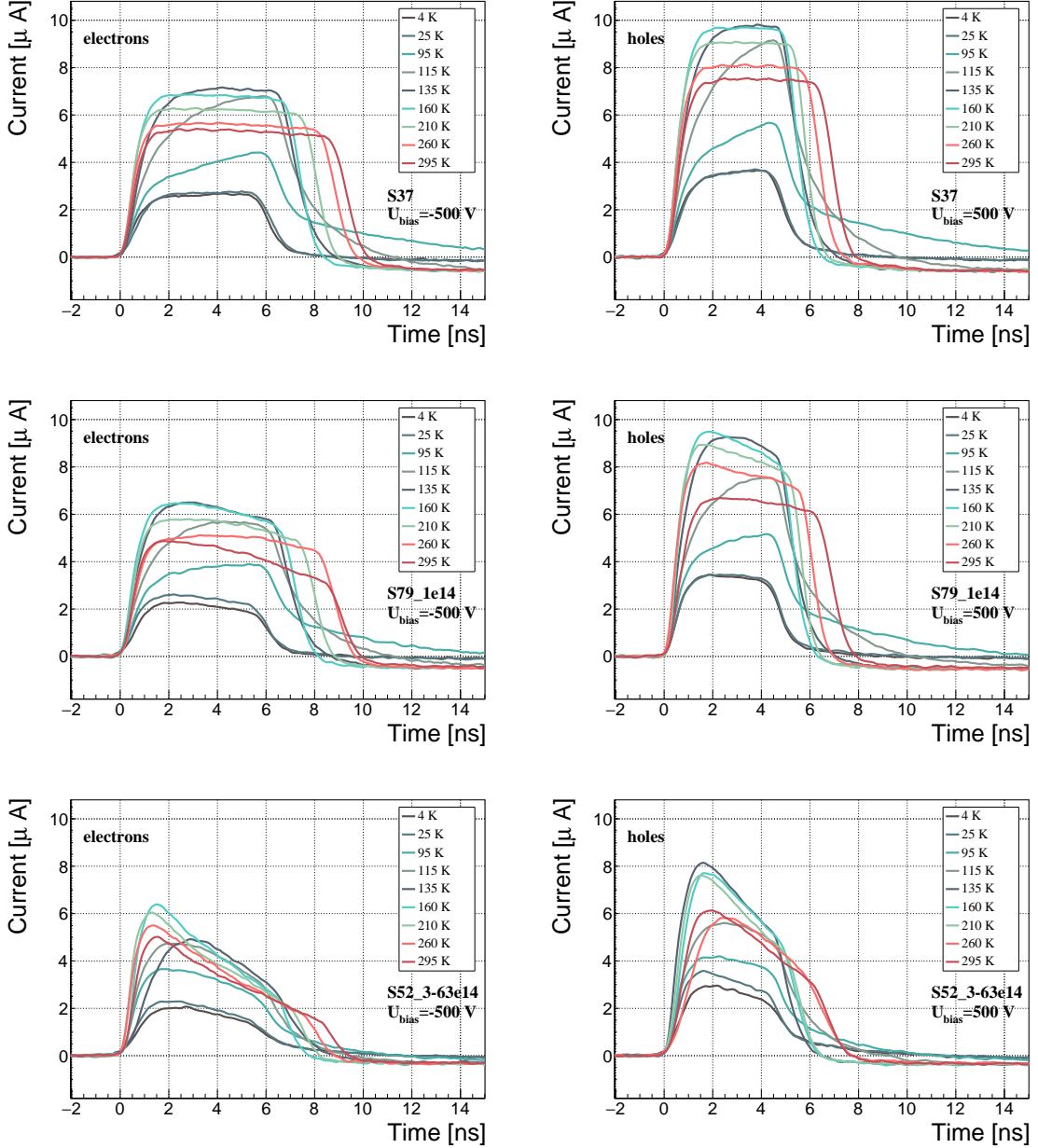


Figure 3.16: After irradiation: several data points between 4 K and 295 K at a bias voltage of  $\pm 500 \text{ V}$ .

samples. The focus is on the temperature range between 4–75 K and 150–295 K whereby the effect of the re-excitation of bound electrons and holes is not prevailing. The values for all samples are fairly stable in the range between 4 K and 75 K and between 150 K and 295 K. However, in the values for the irradiated S52 some excursions can be observed. This is due to the sequence of the measurement steps, which results in a hysteresis effect explained in the preceding text.

The collected charge drops significantly from 150 K down to 75 K. In the non-irradiated

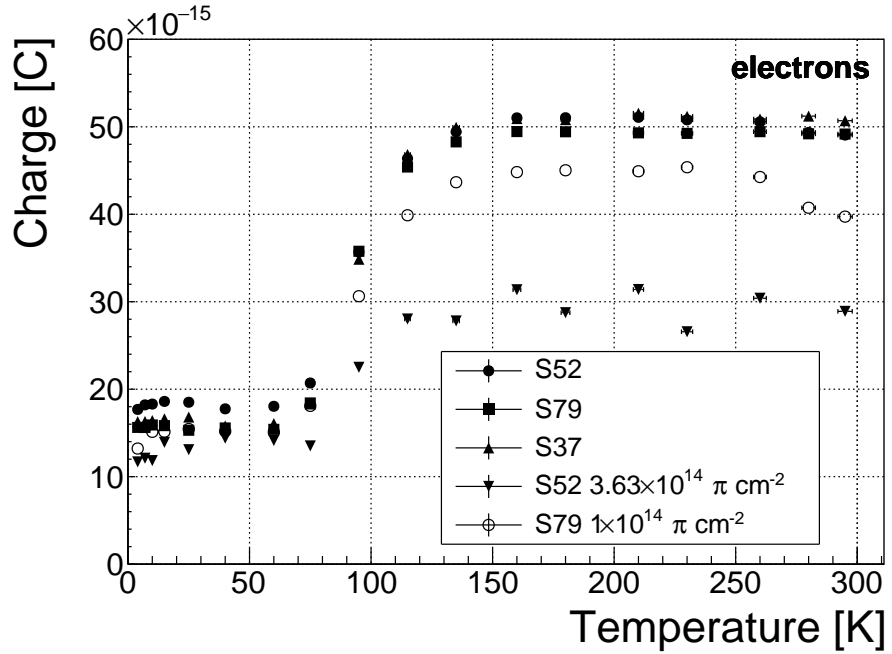


Figure 3.17: Collected charge for electrons as a function of temperature.

samples the values in the lower temperature range are approximately 30 % of those in the high range. For the irradiated samples this difference is lower: 35 % for S79 and 50 % for S52.

An interesting detail in figure 3.17 is that the ratio between the values for non-irradiated samples and their irradiated counterparts at the lower temperature range is different than at the higher range. In other words, the charge loss due to irradiation damage is lower for temperatures between 4 K and 75 K than for temperatures between 150 K and 295 K. The irradiated S52 collects 78 % of the initial charge in the low temperature range, but only 59 % of the initial charge for the high range. The values for S79 for these two temperature ranges are 100 % and 90 %, meaning that the drop in charge collection efficiency after irradiation to  $1 \times 10^{14} \pi \text{ cm}^{-2}$  is negligible for temperatures below 75 K.

### 3.4.2.2 Charge trapping

A decaying exponential function from equation 2.19 has been fitted to the decaying top of the averaged pulses at a bias voltages of  $\pm 400 \text{ V}$  and  $\pm 500 \text{ V}$  across all temperatures excluding the transitional range between 75 K and 150 K. The resulting decay time constants  $\tau$  for an individual temperature point are not equal, which stems from the fact that the pulses change with time due to “polarisation”. This counts as a systematic error. Therefore the fitted  $\tau$  for  $\pm 400 \text{ V}$  and  $\pm 500 \text{ V}$  are averaged into one value representing the measurement at that temperature point. Figure 3.19 shows the fitted  $\tau$  for the five samples between 4 K and 295 K. In principle the time constants should be infinite for an ideal and non-irradiated sample. Here a slightly tilted top of the pulse due to space-charge is already successfully

### 3.4. TEMPERATURE LIMITATIONS

---

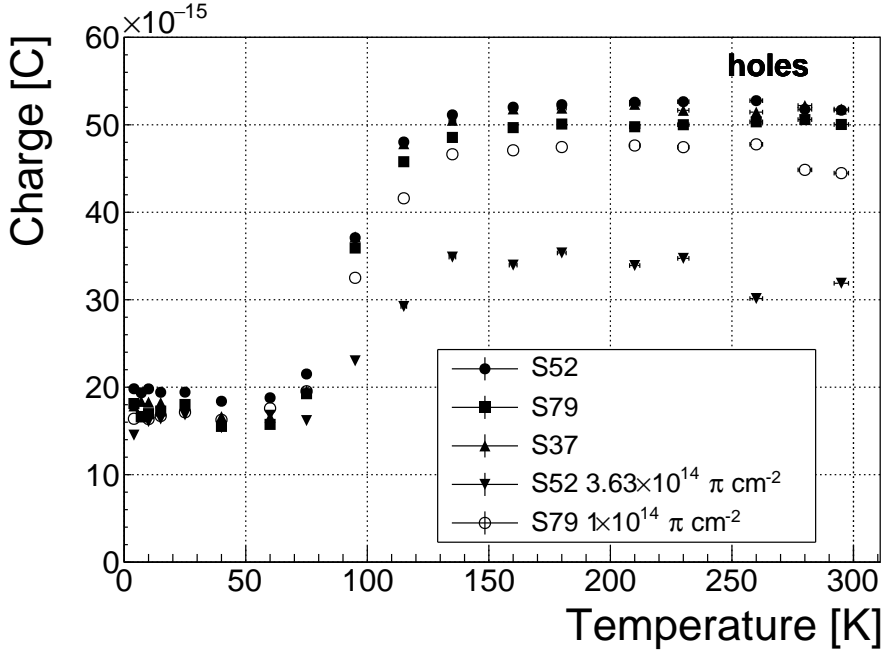


Figure 3.18: Collected charge for holes as a function of temperature.

fitted with an exponential function (a pitfall in the automatic analysis), resulting in a  $\tau$  of the order of  $(200 \pm 20) \times 10^{-9}$  s. Consequently the fitting method is not adequate for non-irradiated samples.

For the irradiated samples the fit becomes increasingly more meaningful. As seen in figure 3.19, the fitted values of the irradiated samples are fairly stable across all temperatures. There is a slight increase in the decay time constant of the S52 from  $(6.0 \pm 0.5) \times 10^{-9}$  s above 150 K to  $(8.5 \pm 0.9) \times 10^{-9}$  s below 75 K. On the other hand, this step is not observable in the S79 data. With only one sample exhibiting this behaviour, the effect is not significant enough. Judging by the data acquired, the samples would need to be irradiated to doses above  $1 \times 10^{14} \pi \text{ cm}^{-2}$  to quantify this effect in detail. So far this effect is not regarded as significant for the scope of this thesis. Building on this assumption, the conclusion is that the signal decay time constant for irradiated sCVD diamond is constant across the temperature range between 4 K and 295 K, excluding the transitional range between 75 K and 150 K where it cannot be quantified properly.

Considering the discussion above, all the values can be averaged into one decay constant. Figure 3.20 shows these values for all samples as a function of the received  $\pi_{300}$  MeV radiation dose. To estimate the charge carrier lifetime with respect to the radiation dose received, a similar model is used than that in section 3.5. This model states that the charge carrier lifetime is linearly decreasing with increasing radiation dose:

$$\frac{1}{\tau} = \frac{1}{\tau_0} + \kappa_\tau \cdot \Phi \quad (3.8)$$

$$\tau = \frac{\tau_0}{\kappa_\tau \tau_0 \Phi + 1} \quad (3.9)$$

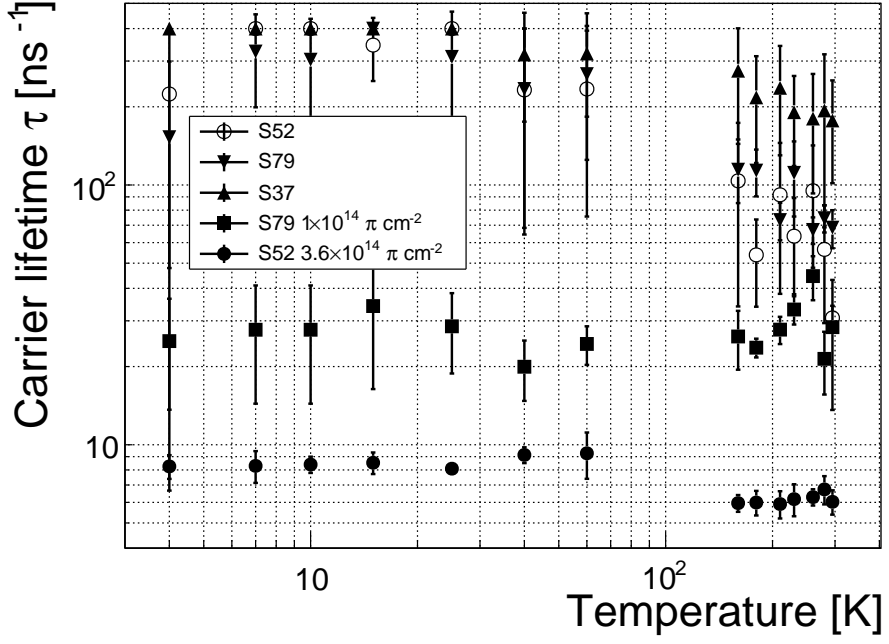


Figure 3.19: This figure shows the charge carrier lifetime as a function of temperature. The data points between 75 K and 150 K are omitted. The fit function only works well on signals with a well pronounced decaying top.

where  $\tau_0$  is the lifetime for a non-irradiated sample (real lifetime, therefore of the order of 400 ns),  $\tau$  is the lifetime of an irradiated sample,  $\Phi$  is the received radiation dose and  $\kappa_\tau$  the lifetime degradation factor. For these data the fitted factor is equal to  $\kappa_\tau = (3.5 \pm 0.8) \times 10^{-16} \text{ s cm}^2 \pi_{300 \text{ MeV}}^{-1}$ . Using this factor, the steepness of the decay in the pulse shape as a function radiation dose can be estimated. This is highly useful information when designing a system where the current pulse shape is an important factor.

### 3.5 Conclusion

This chapter gives an overview of the capabilities and limitations of diamond as a particle detector. Two effects on diamond are studied – radiation and temperature.

Two sCVD diamond detectors were irradiated with 300 MeV pions. They were tested alongside a non-irradiated sample to observe the changes in the ability to detect  $\alpha$ ,  $\beta$  and  $\gamma$  radiation. Their charge collection efficiency was measured in a test beam facility. The results were compared to the results from the RD42 collaboration and a DPA model. A radiation damage factor  $k_\lambda = (4.4 \pm 1.2) \times 10^{-18} \mu\text{m}^{-1} \text{ cm}^{-2}$  was obtained for  $\pi_{300 \text{ MeV}}$  particles. The data point was not in agreement with the data provided by RD42 nor with the model. However, the irradiation process and the low number of tested samples hold a relatively high statistical uncertainty. In addition, there was no diamond surface treatment done in between the measurements, as is the case in the study conducted by RD42. The results obtained in the course of these measurements are going to be fed into the existing

### 3.5. CONCLUSION

---

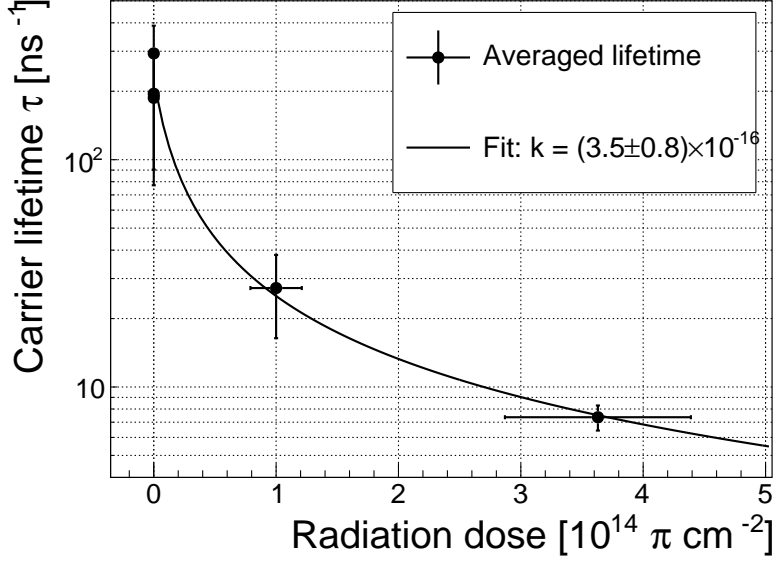


Figure 3.20: This figure shows the carrier lifetime averaged over all temperatures and plotted as a function of the  $\pi$  irradiation dose.

pool of data in the RD42 collaboration.

The next step was to test the long-term capabilities for  $\alpha$  detection. The shape of the ionisation profile was investigated to determine the behaviour of the charge carriers in the irradiated diamond. An exponential decay was observed in the pulses of irradiated samples, proving that there are charge traps in the bulk that were created during irradiation. Then a long-term stability test was carried out. The results show that the irradiated diamond detectors do not provide a stable and reliable long-term measurement of  $\alpha$  particles. This might be due to a space-charge build-up in the bulk, which changes the electric field, affecting the charge carriers. A procedure to improve the pulse shape using  $\beta$  and  $\gamma$  radiation was proposed.

Finally, the diamond sensors were cooled down to temperatures between 4 K and 295 K. Their response to  $\alpha$  particles was observed. The results of the non-irradiated and irradiated samples were compared. The effect of reduction for the number of drifting charges due to exciton recombination was observed in both sets of data. The second set had a superimposed effect of charge trapping during the drift, which was represented by an exponential decay in the signal. The decay time constant did not change with temperature. Therefore all temperature points for individual samples were averaged and the decay time constants were plotted against the received radiation dose. A lifetime degradation factor  $\kappa_\tau = (3.5 \pm 0.8) \times 10^{-16} \text{ s cm}^2 \pi_{300 \text{ MeV}}^{-1}$  for non-primed diamonds was defined.

## Chapter 4

# Charge monitoring

### *The ATLAS Diamond Beam Monitor*

Particle detectors in high energy physics experiments need to meet very stringent specifications, depending on the functionality and their position in the experiment. In particular, the detectors close to the collision point are subject to high levels of radiation. In addition, they need to operate with a high spatial and temporal segmentation to be able to precisely measure trajectories of hundreds of particles in very short time. In addition, they need to be highly efficient. In terms of the structure, their active sensing material has to be thin so as not to cause the particles to scatter or get stopped, which would worsen the measurements. This also means that they have to have a low heat dissipation so that the cooling system dimensions can be minimised. Finally, they need to be able to have a stable operation for several years without a required intervention, because they are buried deep under tonnes of material and electronics.

The material of choice for the inner detector layers in the HEP experiments is silicon. It can withstand high doses of radiation, it is highly efficient (of the order of  $\sim 99.9\%$ ) and relatively low cost due to using existing industrial processes for its production. Its downside is that, with increasing irradiation levels, it needs to be cooled to increasingly low temperatures to ensure a stable operation. This is not the case with diamond. In addition, diamond has a lower radiation damage factor, which means it can operate in a radiation-heavy environment for a longer period.

The ATLAS Diamond Beam Monitor (the DBM) [57] is a novel high energy charged particle detector. Its function is to measure luminosity and beam background in the ATLAS experiment. Given its position in a region with a high radiation dose, diamond was chosen as the sensing material. The monitor's pCVD diamond sensors are instrumented with pixellated FE-I4 front-end chips. The pCVD diamond sensor material was chosen to ensure the durability of the sensors in a radiation-hard environment and the size of its active area. The DBM is not the first diamond detector used in HEP, but it is the largest pixellated detector installed thus far, as shown in figure 4.1. It was designed as an upgrade to the existing luminosity monitor called the Beam Conditions Monitor (BCM) [58] con-

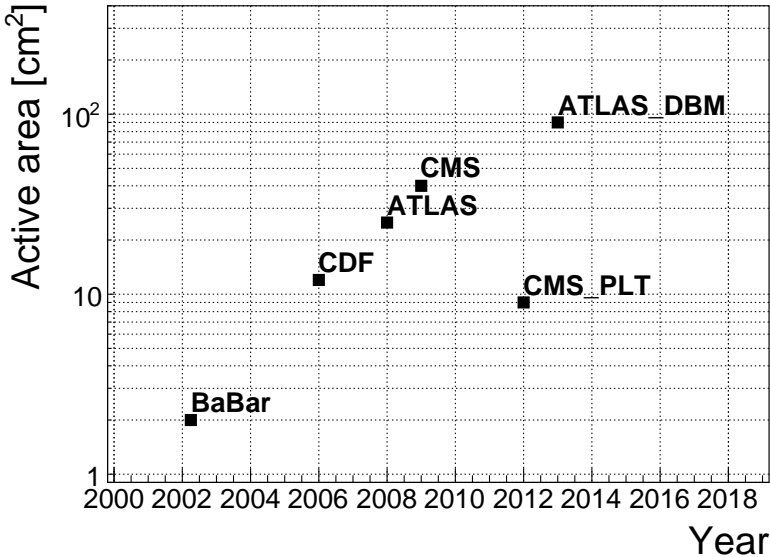


Figure 4.1: Diamond detectors installed in high-energy physics experiments in the last decade, sorted by the active sensor area. The first four detectors from the left are radiation monitors whereas the right two are pixel trackers.

sisting of eight diamond pad detectors. The BCM is able to perform precise time-of-flight (ToF) measurements. The DBM complements the BCM’s features by implementing tracking capability. Its pixelated front-end electronics significantly increase the spatial resolution of the system. Furthermore, the DBM is able to distinguish particle tracks originating in the collision region from the background hits. This capability is a result of its projective geometry pointing towards the interaction region. This chapter first describes the principles of luminosity measurements. It then explains how the DBM carries out this task. Finally, some results from the commissioning and from the real collisions are presented.

When a particle traverses a sensor plane, a hit is recorded in the corresponding pixel. Thus, a precise spatial and timing information of the hit is extracted. With three or more sensors stacked behind each other, it is also possible to define the particle’s trajectory. This is the case with the DBM. Its projective geometry allows the particles to be tracked if they traverse the sensor planes. The DBM relates the luminosity to the number of particle tracks that originate from the collision region of the ATLAS experiment. Particles that hit the DBM from other directions are rejected as background radiation.

## 4.1 Luminosity measurements

Luminosity is one of the most important parameters of a particle collider. It is a measurement of the rate of particle collisions that are produced by two particle beams. It can be described as a function of the beam parameters, such as: the number of colliding bunch pairs, the revolution frequency, the number of particles in each bunch and the transverse bunch dimensions. The first four parameters are well defined. However, the transverse

bunch dimensions have to be determined experimentally during calibration measurements. The ATLAS experiment uses the *van der Meer scan* [59] during low-luminosity runs to calibrate the luminosity detectors. This scan is performed by displacing one beam in a given direction and measuring the rate of interactions as a function of the displacement. The transverse charge density of the bunches can be estimated on the basis of the interaction rate. The calibrated luminosity detectors can then operate during high-luminosity runs.

One approach to luminosity monitoring is to count the number of particles produced by the collisions. The luminosity is then proportional to the number of detected particles. A detector has to be capable of distinguishing individual particles that fly from the interaction point through the active sensor area. If the detector has at least three layers, it can reconstruct the particles' tracks, which in turn yields more information on their trajectory. This is one reason why detectors with a high timing- and spatial segmentation are more suitable for these applications. The second reason is that, with a high spatial segmentation, the detector does not saturate even at high particle fluencies.

## 4.2 Diamond pixel module

The two most important parts of the diamond pixel module are the sensor, which translates the incident ionising radiation into charge carriers as explained in chapter 2, and the pixelated front-end chip, which collects the ionised charge with a high spatial segmentation, processes the recorded data and sends them to the readout system. This section describes these two parts of the module and their interconnection.

### 4.2.1 Sensors

The DBM modules are instrumented with two types of sensors – pCVD diamond and silicon. The silicon sensors are used as a fallback solution because there were not enough high-quality diamond sensors available during the construction phase. In addition, a comparative study of irradiation damage between silicon and diamond can be made with such a hybrid system.

**Diamond sensors** The target material for this application is pCVD diamond. The reason for this is that the active area of an individual sensor must be approximately  $4\text{ cm}^2$ , which is too large for the sCVD diamond. pCVD material is also a bit cheaper, which makes a detector with a large active area more feasible to build. The material is provided by three companies: DDL, E6 and II-IV and it is grown in 15 cm wafers, as seen in figure 4.2. The target thickness of the wafers is 500  $\mu\text{m}$ . The minimum required charge collection efficiency is 40 % ( $\text{CCD} \geq 200\text{ }\mu\text{m}$ ) to ensure that the MPV of the collected charge for MIPs is still well above the noise of the electronics even after heavy irradiation. They need to be operated at bias voltages between 600–1000 V. On one side there is a single gold electrode applied across the entire surface. On the other side a pixellated metallisation is added.

**Silicon sensors** are standard  $n^+ - in - n$  planar sensors with a 200  $\mu\text{m}$  thickness and were fabricated at CiS [60], a company from Erfurt, Germany. They are designed to have nearly

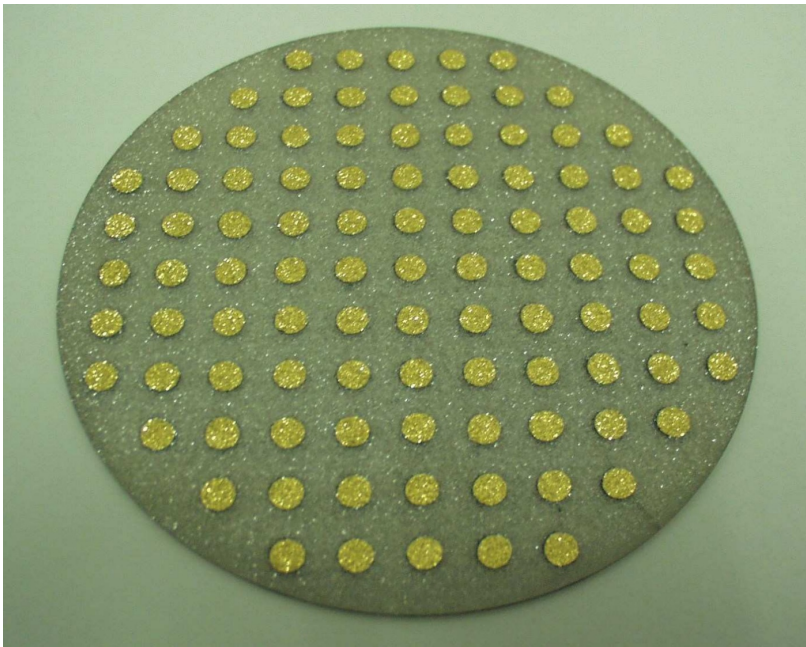


Figure 4.2: A pCVD wafer. The golden dots on the surface are the electrodes that are applied during the qualification test. The wafer is measured across the surface to find the regions with the highest efficiency.

a 100 % efficiency when not irradiated. One side is segmented into pixels. Guard rings at the edges of the sensor provide a controlled drop in potential, reducing the possibility of shorts at maximum design bias voltages of the order of 1000 V.

#### 4.2.2 Front-end electronics

The FE-I4 (front-end version four) [61] is an ASIC pixel chip designed specifically for the ATLAS pixel detector upgrade. It is built as a successor to the current pixel chip FE-I3, surpassing it in size of the active area ( $6\times$  larger) as well as the number of channels/pixels ( $10\times$  more). 336 such FE-I4 modules are used in the newly installed pixel layer called the Insertable B-Layer (IBL) [62]. The DBM is also instrumented with these chips. The FE-I4's integrated circuit contains readout circuitry for 26880 pixels arranged in 80 columns on a 250  $\mu\text{m}$  pitch and 336 rows on a 50  $\mu\text{m}$  pitch. The size of the active area is therefore  $20.0\times16.8 \text{ mm}^2$ . This fine granularity allows for a high-precision particle tracking. The chip operates at 40 MHz with a 25 ns acquisition window, which corresponds to the spacing of the particle bunches in the LHC. It is hence able to correlate hits/tracks to their corresponding bunch. Furthermore, each pixel is capable of measuring the deposited charge of a detected particle by using the Time-over-Threshold (ToT) method. Finally, the FEI4 has been designed to withstand a radiation dose up to 300 MGy. This ensures a longterm stability in the radiation hard forward region of the ATLAS experiment.

Each pixel is designed as a separate entity. Its electrical chain is shown in figure 4.4. The bump-bond pad – the connection to the outside of the chip – is the input of the

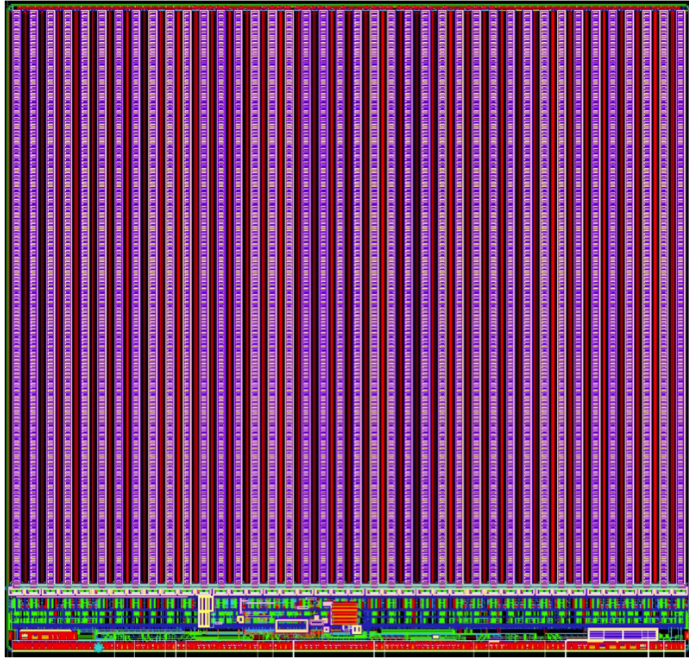


Figure 4.3: FE-I4 layout, top-down view. The pink area are pixels grouped into columns, the green area below is the common logic and the red strip at the bottom are the wire bond pads.

electrical chain, connected to a free-running amplification stage with adjustable shaping using a 4-bit register at the feedback branch. The analog amplifier is designed to collect negative charge, therefore electrons. The output is routed through a discriminator with an adjustable threshold. This value in effect defines the level at which the circuit detects a hit. In addition, there is a counter of the clock cycles (25 ns sampling) during which the signal is above the discriminator threshold. The value of the counter is proportional to the collected charge. The logic gates at the end of the chain are used to enable/disable the pixel and to issue a so-called HitOr flag – this signal is set whenever at least one of the pixels was hit and is used as a trigger for the readout. The output of the chain – HitOut – is routed into the logic of the chip where it is buffered and sent out to the readout system. The module receives all its commands from the system via a 40 MHz LVDS line. The commands are either settings for the pixel registers or triggers that start the data readout. The data are sent via an LVDS line at up to 320 Mbit/s, but by default at 160 Mbit/s, four times faster than the clock of the device. This allows the chip to clear out its buffers before new data are recorded, thus avoiding dead time and data pile-up. The FE-I4 has been successfully tested for trigger rates of up to 300 kHz, depending on the occupancy per trigger.

The DBM uses pCVD diamond with  $d_C = 500 \mu\text{m}$  thickness and silicon with  $d_{Si} = 200 \mu\text{m}$  thickness as a sensor material. The resulting most probable value (MPV) of the deposited charge for a minimum ionising particle (MIP) is calculated with the formula  $Q_S = d \cdot E_{e-h}$  and equals 18000 electrons and 17800 electrons, respectively, at a full charge collection efficiency. Unfortunately this is not the case with the pCVD material, whereby

### 4.3. MODULE ASSEMBLY

---

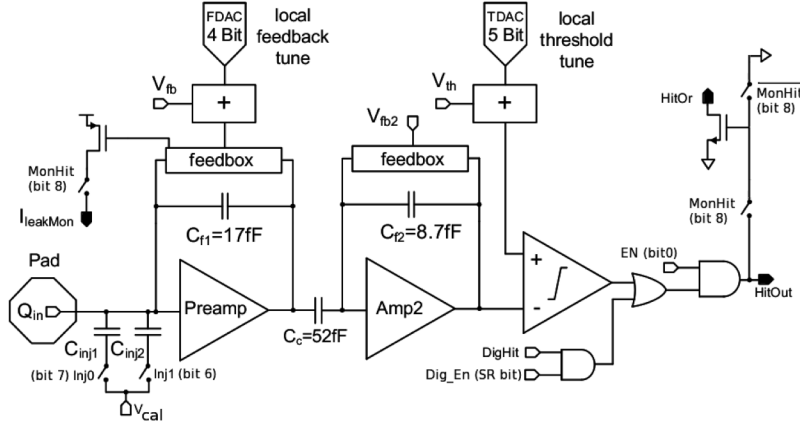


Figure 4.4: Schematic of an analog pixel. Courtesy of the FE-I4 collaboration.

the expected charge collection efficiency is of the order of 50 % – around 9000 e. This value further decreases with received irradiation dose. Therefore in order to detect the particles depositing energy on the far left side of the landau spectrum, the threshold has to be set to a significantly lower value. On the other hand, if the threshold set too low, it also detects the electronic noise and generates false hits. Typical noise amplitudes are in the range of 120–200 e. A safe threshold range is approximately five times above this value. The target for the DBM is to set the threshold to 800 e.

The analog amplifier is implemented in two stages to get a fast rise time at a low noise and a low power consumption. The output signal of the analog amplifier has a triangular shape with a fast rise time and a long decay. The shape can be adjusted by tuning the amplifier feedback loop. Its length is proportional to the collected charge, but it needs to be calibrated first. This is done by means of two injection capacitors,  $C_{\text{inj}1}$  and  $C_{\text{inj}2}$ , seen in figure 4.4 with well defined capacitances. First, the charge  $Q_{\text{cal}} = V_{\text{cal}} \cdot (C_{\text{inj}1} + C_{\text{inj}2})$  is injected into the analog chain. Then the length of the output pulse is measured and finally the feedback value is changed to either lengthen or shorten the pulse in order to get to the required duration  $t_{\text{cal}}$ . The typical values are  $Q_{\text{cal}} = 5000 - 16000$  e at the time  $t_{\text{cal}} = 5 - 10$  ToT. The target values depend on the sensor, the type of a radioactive source and the application. Therefore the initial threshold  $Th$  at 1 ToT and the calibrated value  $Q_{\text{cal}}$  at  $t_{\text{cal}}$  ToT give us a linear scale of collected charge with respect to time over threshold. However, in practice this relation is nonlinear for lower thresholds, but since the goal of the measurements is to track the particles rather than to measure their deposited energy precisely, this is sufficient.

## 4.3 Module assembly

Parts for the detector arrived separately and were assembled into modules at CERN’s DSF lab after being checked for production faults. The assembled modules underwent a series of quality control (QC) and burn-in tests to determine their quality, efficiency and long-term

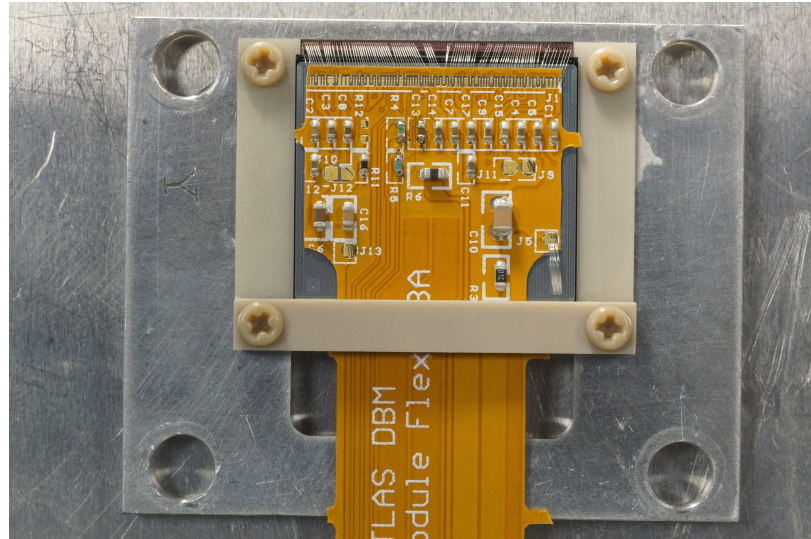


Figure 4.5: DBM module, top-down view. Visible is the flexible PCB with signal and power connections, the silicon sensor and a part of the FE-I4. Wire bonds from the PCB to the FE-I4 and to the sensor are also visible.

stability.

A DBM single-chip module consists of a hybrid pixel module, a flexible PCB and the supporting mechanics (a ceramic plate and an aluminium plate). The chip arrives already bump-bonded to the sensor, be it diamond or silicon. First it is glued to the ceramic plate on one side and to the PCB on the other using Araldite 2011 or Staystik 672/472. Staystik is re-workable and has a very high thermal conductivity. The latter is important because the FE-I4 chips tend to heat up significantly and need a good heat sink. The problem is that it has a curing temperature of 160/170 °C. This temperature may cause some unwanted stress build-up between the FE-I4 and the diamond sensor due to different coefficients of thermal expansion, pulling them apart. This would disconnect the pixels, yielding large regions of the module insensitive to radiation. Araldite 2011 on the other hand can be cured at lower temperatures – down to RT – but it has a lower heat conductivity. In the end Araldite is used as a safer option. However, due to the longer curing, the entire assembly process using Araldite is extended to two working days. After curing, the module is wire-bonded and attached to the aluminium plate using screws made up of a radiation-resistant PEEK plastic. They have to be tightened with a great care, because their screw head is only 0.2–0.6 mm away from the sensor edge – the sensor displacement tolerance during gluing is of the order of 0.5 mm. Finally, the module is put in an aluminium carrier which protects it from mechanical damage or electrostatic discharges. Figure 4.5 shows an assembled module.

#### 4.4 Performance results

This section gives an overview of the performance results of the DBM modules achieved during the QC and the test beam campaign. The source tests were performed to check

## 4.4. PERFORMANCE RESULTS

---

for disconnected regions in the sensors and to measure the diamond's efficiency. Only the modules with minimal disconnected regions and maximum efficiency were chosen for installation.

### 4.4.1 Source test results

The modules are tested in the lab using an Reconfiguration Cluster Element readout system [63] and a moving stage with two degrees of freedom. They are placed onto the stage and connected to the readout system and the power supplies. After ensuring the low- and high voltage connectivity they are checked for the signal connectivity. If everything is operational, a series of automated tests is run. Each of these tests calibrates a certain value within a pixel, whether it is the signal threshold or the value for integrated charge. These are tuned in a way that the response to a predefined calibration signal is uniform for all pixels across the sensor. This procedure is referred to as *tuning*.

When the modules are tuned, they are tested using a  $^{90}\text{Sr}$  radioactive source. Two characteristics of each module are checked: 1) operation of all pixels and 2) sensor efficiency.

#### 4.4.1.1 Pixel connectivity

The first test is carried out to determine the number of disconnected pixels in the matrix. This is an important step in the DBM QC procedure, because it turns out that a significant portion of the flip-chipped diamond sensors exhibited very poor connectivity. The disconnected regions on the faulty modules ranged anywhere from 0.5–80 % of the overall active surface. In two cases the sensor was even completely detached from the chip. Therefore the pixel connectivity turns out to be the most important qualification factor in the QC procedure. Unfortunately the only way to check it at the moment is to fully assemble a module and test it using a radioactive source. If the module turns out to be of poor quality, it is disassembled and sent for rework. The turnover time of this operation is of the order of one month, which affected the DBM installation schedule significantly. In the end the modules with less than 3 % disconnected pixels have been accepted.

The test for disconnected regions is carried out by moving the module under the source in X and Y direction so that the exposure over the entire plane is uniform. The resulting occupancy map reveals pixels that are not electrically coupled to the sensor via bump bonds. The occupancy scans are shown in figures 4.6a and 4.6b. The silicon module has a very uniform occupancy plot. So much so that the features of the overlaying flexible PCB can be observed. The rectangular shadows are the passive components whereas the lines are the traces in the PCB. Furthermore, a circular-shaped edge of the PCB can be seen on the bottom right side of the plot. These darker areas are such because fewer electrons can penetrate the material with a high density. In the case of the diamond, the features of the PCB can be observed as well, but are much less distinguishable as the plot is much more granulated – less uniform. This high variance in the diamond's detection ability is due to the grain boundaries in the pCVD material which trap the drifting charges, rendering some

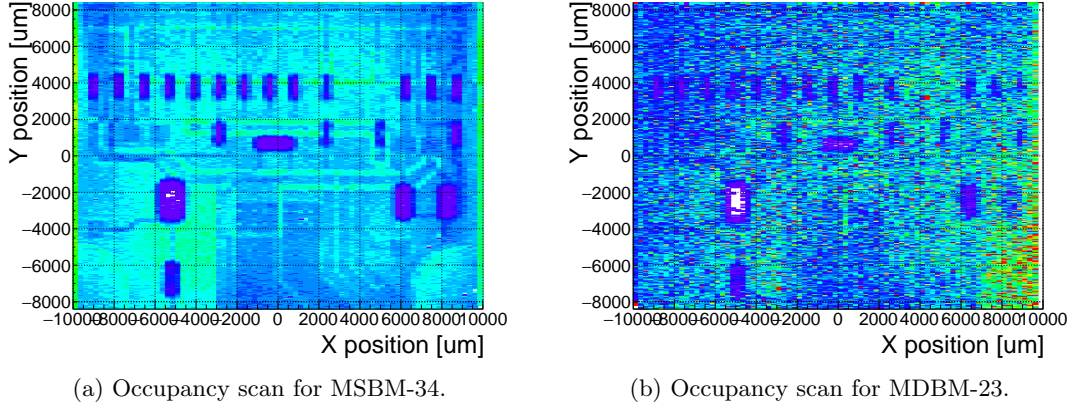


Figure 4.6: Occupancy scans for the silicon (left) and diamond sensor (right) to check for disconnected regions. Shadows of the electronic components are clearly visible because fewer electrons were able to traverse through such a higher amount of material.

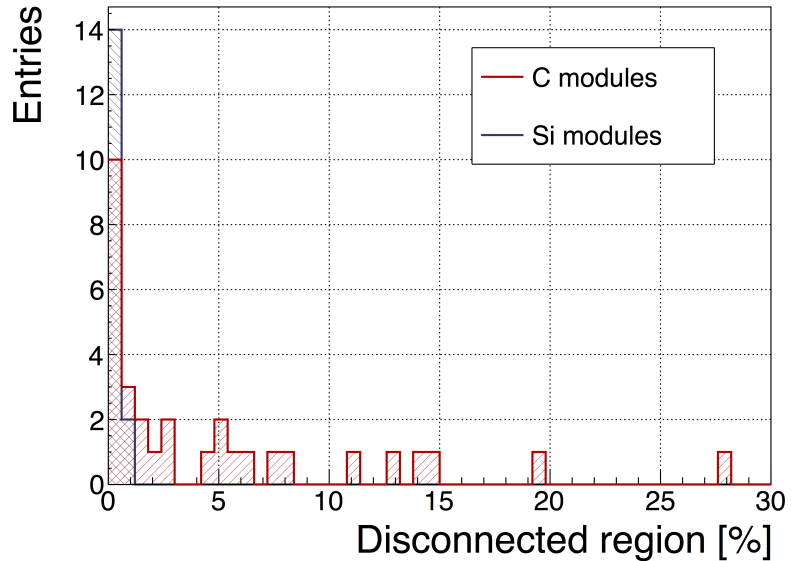


Figure 4.7: Disconnected regions for all modules derived from the occupancy scans.

regions significantly less efficient.

Figure 4.7 shows the distribution of disconnected regions across all tested modules. Silicon modules were performing as expected, with a minimum number of disconnected pixels.

#### 4.4.1.2 Pseudo-efficiency

Only the modules that passed the pixel connectivity test undergo the second test stage in which the sensor's efficiency is estimated. A scintillator is placed underneath the module and is used as a trigger. A particle that crosses the DBM module and hits the scintillator, triggers the module readout. In the end, the number of triggers is compared to the number

#### 4.4. PERFORMANCE RESULTS

---

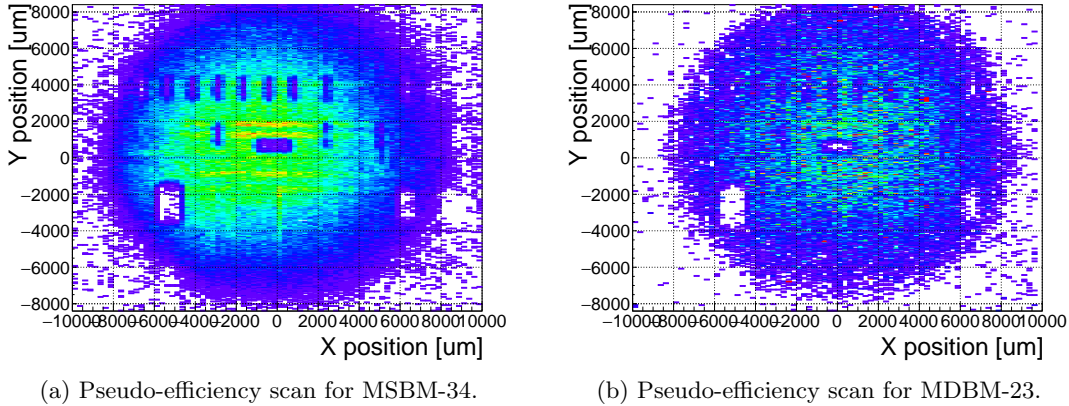


Figure 4.8: Pseudo-efficiency scans for the silicon (left) and diamond sensor (right) to estimate the efficiency of the sensors.

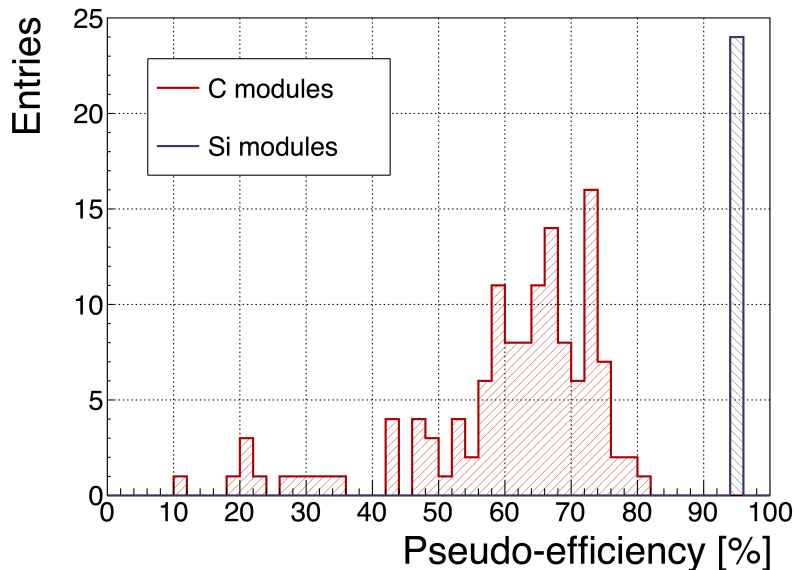


Figure 4.9: Pseudo-efficiencies for all modules at various threshold and voltage settings.

of hits/clusters recorded by the module. These are shown in figures 4.8a and 4.8b.

However, the resulting ratio is only an estimate of the sensor's detection efficiency. This is because the  $\beta$  particles scatter around the setup and sometimes hit the scintillator from other directions without traversing the module, producing empty triggers. Therefore the real sensor efficiency can only be measured in a high energy particle beam and using a beam telescope as a reference detector to measure the particle trajectories. Nonetheless, this *pseudo-efficiency* gives a rough estimate of the sensor's quality.

Figure 4.9 shows the distribution of pseudo-efficiencies for all modules that went through the QC. The majority of the silicon modules yield the pseudo-efficiency of  $(94.3 \pm 0.2) \%$ . Silicon sensors being 99.99 % efficient, this value is underestimated by about 5 %. The measured pseudo-efficiency of the diamond modules is  $(65 \pm 7) \%$ , with outliers down to

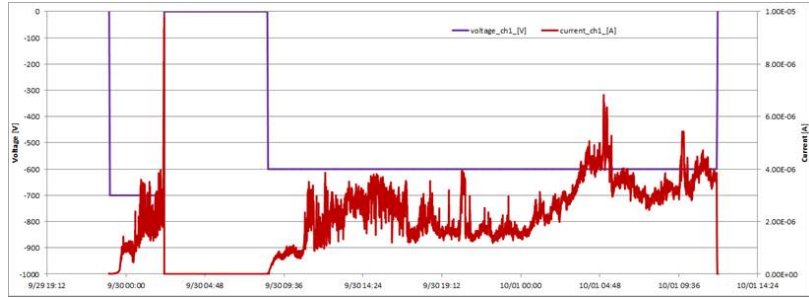


Figure 4.10: Erratic current in a DBM diamond module.

10 %. The value depends on the diamond quality, the set threshold and the applied bias voltage. The latter two settings are varied to check the behaviour of the modules under various conditions.

#### 4.4.2 Erratic current

A very important parameter for qualifying a module is the erratic current [64] in the sensor. This term describes the leakage current in a pCVD diamond that becomes unstable. It can develop gradually or can be triggered with a  $\beta$  source. Spikes appear in the otherwise stable leakage current. They can be up to three orders of magnitude higher than the base current. Sometimes the current also suddenly increases for a few orders of magnitude and stays at that level (e.g. from the initial 1 nA to 3  $\mu$ A). An example of such behaviour is shown in figure 4.10.

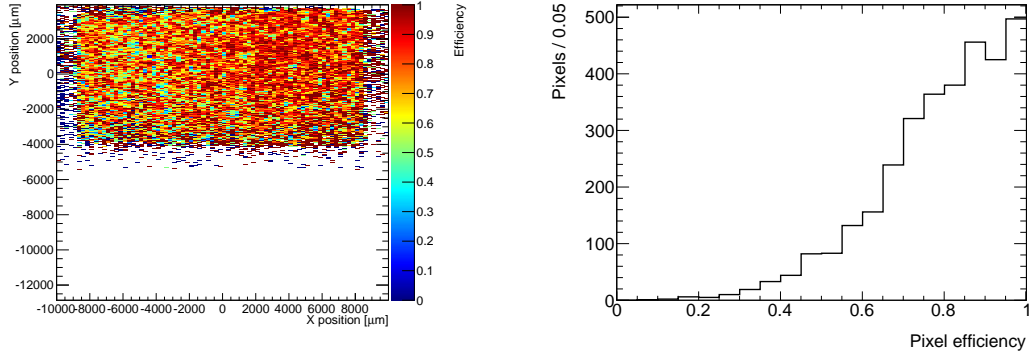
The amplitude differs in magnitude from sensor to sensor. This effect is still not fully explained, but the hypothesis is that the charges find a conductive channel along the grain boundaries, causing discharges. These discharges are picked up by the pixel amplifiers in the FE-I4. A single discharge can trigger a group of up to  $\sim$ 500 pixels, resulting in a *blob* on the detector occupancy map. Sometimes the conductive channel stays in a conductive state, making one or more pixels always to fire. These pixels saturate the bandwidth of the readout channel, so they have to be masked out during measurements.

#### 4.4.3 Test beam results

The first two assembled prototype DBM modules, MDBM-01 and MDBM-03, were tested at DESY, Hamburg, in a test beam facility. The aim of the measurements was to measure their efficiency, the spatial distribution of the efficiency and the effect of the beam on the disconnected regions. A silicon module MSBM-02 was measured to crosscheck the measurements. Since the silicon module is almost 100 % efficient, it was used as an “anchor” – the efficiency of the diamond module was measured relative to that of the silicon module. Two beam telescopes were used as reference systems: Kartel telescope [65] built by JSI institute from Ljubljana, and EUDET Aconite [66]. Both are instrumented with six Mimosa26 pixel planes and capable of tracking particles with a 2  $\mu$ m pointing resolution.

#### 4.4. PERFORMANCE RESULTS

---



(a) This figure shows an efficiency map of ad DBM pVCD diamond module. Each bin corresponds to a single pixel. The triggering scintillator of the Kartel telescope is smaller than the DUT. Hence, the recorded hits can only be seen in the top half of the sensor.

(b) A pixel efficiency distribution from the run in figure (a).

Figure 4.11: An efficiency study of a prototype DBM diamond module in a test beam. The statistics are low ( $\sim 10$  hits/pixel) as the data were collected during a short run.

The test beam prototypes did not meet the acceptance criteria for production DBM modules in the following areas: first, the stated CCDs were slightly below 200  $\mu\text{m}$ , which would be the DBM minimum. Secondly, the applied bias voltages ranged from 1–2 V/ $\mu\text{m}$ . In addition, the threshold cut could only be set to 1500 electrons, which is higher than the DBM minimum (1000 e). Nonetheless, the resulting module efficiencies were still in the range 70–85 %.

To analyse the test beam data, Judith software framework [65] was used. Judith is capable of synchronising data streams from several detector systems only connected via a trigger system, reconstructing tracks and calculating efficiency for the DUTs. It was also used to reconstruct and analyse the acquired Kartel test beam data together with the silicon and diamond module as DUTs. A sample of the analysed data is shown in figures 4.11a and 4.11b.

##### 4.4.4 Summary of the QC

The results for the DBM QC are shown in section ???. All in all, 79 modules went through the QC procedure – 43 diamond modules and 36 silicon modules, 12 of the latter only for testing purposes. Figure 4.12 shows their production with time. 18 diamond modules and 6 silicon modules were in the end chosen to be integrated into DBM telescopes and installed into ATLAS.

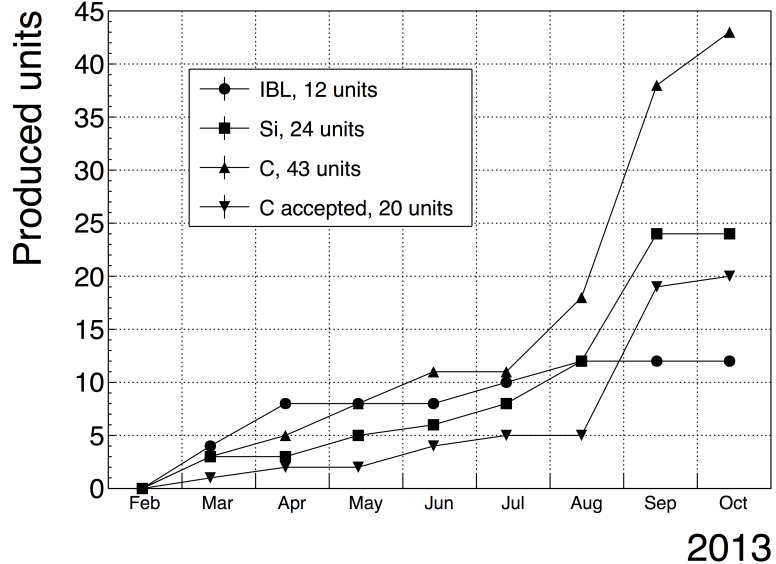


Figure 4.12: Module production with time.

## 4.5 Installation and commissioning

The DBM modules that passed the QC tests were assembled into telescopes – sets of three modules one behind the other with a spacing of 50 mm. Of the 18 diamond and 6 silicon modules, 6 diamond and 2 silicon telescopes were built. A special care was taken when choosing the sets of three diamonds. The modules with a similar pseudo-efficiency, leakage current, maximum stable high voltage and shape of disconnected regions were grouped together. After assembly into telescopes, the modules were tested for their connectivity. Then the high voltage was applied and the leakage current was observed. This was an important point to check because all three modules shared the same high voltage channel. Any instabilities on one of the modules would cause problems on the other two. This would for instance happen if one of the modules had a much lower breakdown voltage.

Due to time constraints, the telescopes were not built at the same time but instead the production was pipelined. As soon as two telescopes were ready, they were transported to Point 1 – the site where parts of the ATLAS detector were being put together. There they were prepared for installation onto the pixel detector structure that had been extracted from ATLAS due to pixel detector commissioning. The commissioning was nearing completion, so the technicians were preparing the detector for re-insertion. The cylindrical structure was being enclosed by four new service quarter-panels (nSQPs). This meant that with every day the access to the place of installation of the DBM was more difficult. The first two telescopes were still put into place when only one nSQP was in place. This allowed the installation process to be carried out from both sides. This proved to be helpful, because the process was lengthy and had to be done with great precision. It involved tightening several screws on both sides of the telescopes, adding thermal paste on the aluminium joints



Figure 4.13: This photo highlights four telescopes installed onto the nSQPs and around the pipe.

and removing the protective covers, revealing the fragile wire bonds. At the same time the surrounding electronics and cables had to be left untouched. The lessons learnt with the first part of the installation were helpful when installing the other telescopes. The last two were fitted onto the structure when three nSQPs were already in place, leaving only a narrow opening for access. The entire procedure was carried out blind. After every installation, the telescopes were tested again. First, the low voltage connectivity was checked and a set of tests was run on the FE-I4 front-end chips. An eye diagram was made to estimate the quality of the signal transmission. Then a  $^{90}\text{Sr}$  source was used to perform a source test on three modules at the same time. Leakage current was observed during the source test. The final test included running four telescopes (all on one side) at a time. All the tests were successful and the DBM was signed off.

#### 4.5.1 Positioning in ATLAS

The DBM is placed in the forward region of the ATLAS detector very close to the beam pipe, as shown in figure 4.14. Eight DBM telescopes reside approximately 1 m away from the collision region, four on each side. They are tilted with respect to the beam pipe for 10°. This is due to a specific phenomenon connected to erratic (dark) currents in diamond. Studies have shown [64] that the erratic leakage currents that gradually develop in diamond can be suppressed under certain conditions. For instance, if a strong magnetic field is applied perpendicular to the electric field lines in the diamond bulk, the leakage current stabilises. The DBM was designed to exploit this phenomenon. The magnetic field lines in the ATLAS experiment are parallel to the beam. Hence, an angular displacement of

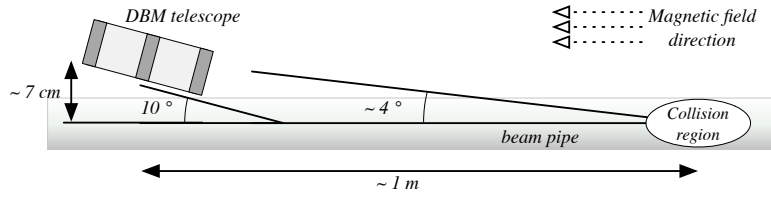


Figure 4.14: Position of the DBM in the ATLAS experiment.

the sensor with respect to the beam allows for the leakage current suppression. However, the DBM telescopes still need to be directed towards the interaction region. Taking these considerations into account, a 10° angle with respect to the beam pipe was chosen. The influence of the magnetic field on the particle tracks at this angle is very low as the field lines are almost parallel to the tracks. The tracks are therefore straight, which reduces the track reconstruction complexity.

## 4.6 Operation

The DBM has been commissioned in ATLAS and is now taking data. Several issues still need to be resolved regarding the readout system. Unfortunately, due to issues with the low voltage power supply regulators, six out of 24 modules were damaged during operation: four silicon and two diamond modules. The system configured the modules into an unsteady state whereby they drew twice as much current as the allowed maximum. This current most probably fused the wire bonds within minutes. This has left only five diamond telescopes fully operational. The preliminary data obtained using the remaining telescopes show that the background rejection could indeed work.

The first step of the system test was to take data during collisions and check the occupancy in the individual modules. The occupancies were plotted side by side for comparison. Figure 4.15 shows some of the occupancy values. At the time, the readout system was not yet configured to read out all telescopes in parallel.

The second step was to test the detector's capability of particle tracking. Only one telescope was used to take data with the beam. If all three planes of the telescope were hit during a bunch crossing, a linear line was fitted to the hits. This line represented the particle's trajectory. It was projected towards the interaction point. Two parameters were calculated where the line is the closest to the interaction point: the radial distance and the longitudinal distance between the line and the interaction point, as shown in figure 4.16. This was done for the events with two colliding bunches as well as for events with only one, non-colliding bunch. The tracks recorded during the events with two colliding bunches could either come from the collisions or could be background scattering. Tracks recorded during a non-colliding bunch, on the other hand, are definitely background particles since there are no collisions taking place.

#### 4.6. OPERATION

---

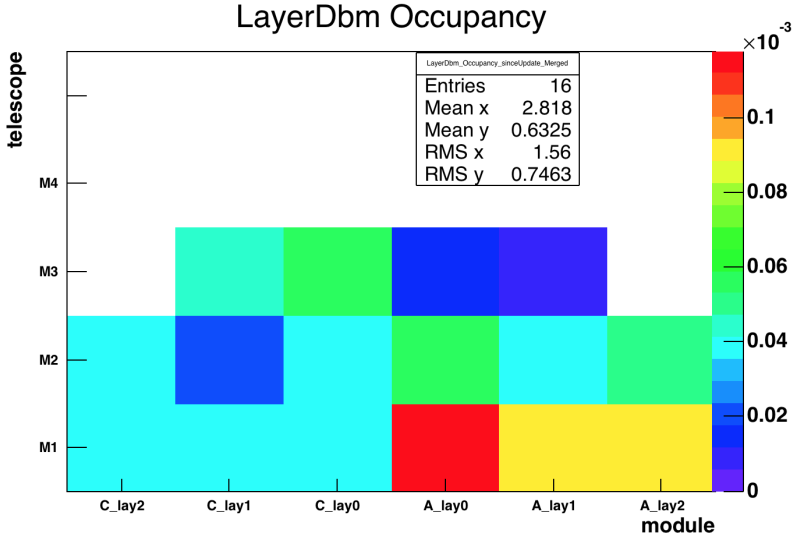


Figure 4.15: Occupancy of individual modules during collisions. Only 16 modules were taking data.

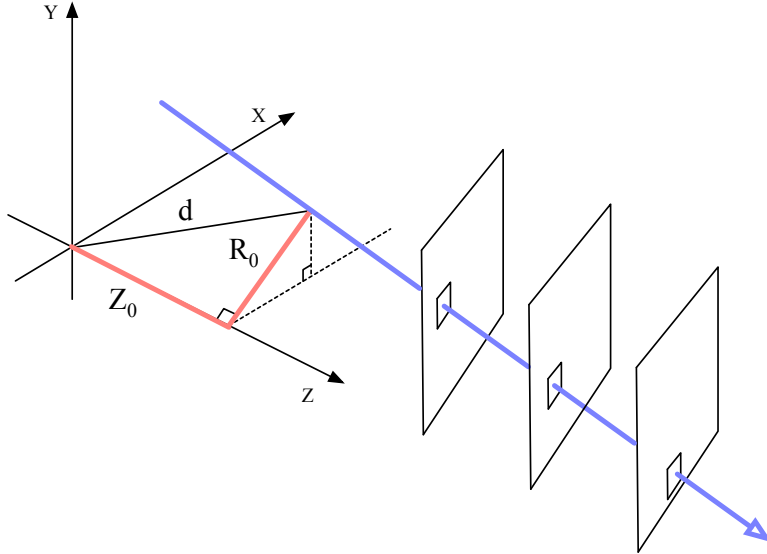


Figure 4.16: A diagram showing the radial distance  $R_0$  and longitudinal distance  $Z_0$  of the trajectory from the interaction point at the minimal distance  $d$ .  $Z$  is the axis along the beam line. Three module planes intercept a particle and reconstruct its trajectory.

A comparison of the data acquired and depicted in figures 4.17a and 4.17b shows that, for the colliding bunches, the majority of the reconstructed tracks had the origin in the interaction point, with a narrow spread in  $Z$  and  $R$ . For non-colliding bunches, the spread is wider. In the  $Z_0$  plot the distribution has one peak in the middle, which means that the empty RF buckets still held some particles which collided. The two peaks on the sides, however, show that a significant number of tracks had their origin at the radius of the beam

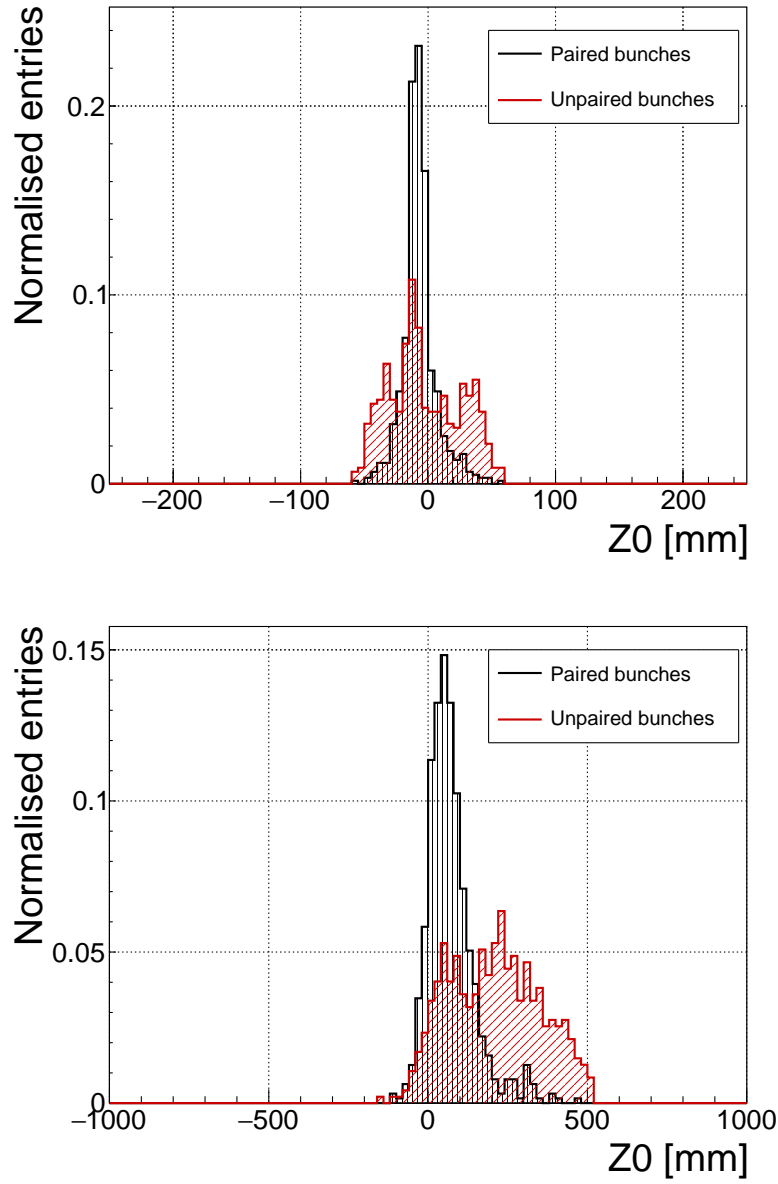


Figure 4.17: These two plots show two parameters of particle tracks recorded by one of the DBM telescopes: radial (a) and longitudinal (b) distance of the projected tracks from the interaction point.

pipe. Therefore these tracks were made by stray protons colliding with the beam pipe. These collisions are unwanted as they do not produce any meaningful physics while still damaging the ATLAS detector by means of the scattered radiation.

## 4.7 Conclusion

The Diamond Beam Monitor has been designed as an upgrade to the existing luminosity detectors in the ATLAS experiment. It is the first diamond pixel tracking detector installed in a high-energy physics experiment. The pixelated front-end electronic chips ensure precise spatial detection of the charged high-energy particles. The projective geometry allows for particle tracking and background rejection. The detector is placed in a high-radiation forward region of the experiment. Therefore, radiation hardness of the chosen pCVD diamond sensors is an important requirement. The tests carried out in the test beam and in the laboratory confirmed that enough detector-grade DBM modules have been built to be installed in the experiment. The DBM is now running in ATLAS during collisions. Further improvements have to be made on the readout firmware before it is included in the main readout stream.

# Chapter 5

## Current monitoring

### *Real-time particle identification*

Diamond sensors have a very fast signal response due to their low capacitance. The electrical signal created by drifting charge carriers retains its shape without significant distortion. When the sensor is used together with a fast current amplifier with a high broadband limit ( $\sim 2$  GHz) and a readout device with a similar limit, the information about the drifting charges is retained. For instance, a proton creates the free e-h pairs along its trajectory. The electrons and holes start drifting immediately. Those closest to the electrodes recombine quickly whereas those at the opposite side contribute to the induced signal for longer. The resulting signal is therefore a triangular pulse with a steep rising edge and a gentle falling edge. It is possible to determine the drift velocity of the charge carriers by measuring the width of the pulse, as was done in chapter 3. Furthermore, it is possible to determine with a certain probability what is the type of incident radiation, judging by the shape of the induced pulse. This, however, only applies to sCVD diamond material. Its uniform carbon lattice allows the ionisation profiles to retain their shape, unlike in pCVD material, laden with grain boundaries, or even in silicon where the shape is deformed due to p-n junction non-uniformities.

This chapter describes an application that carries out particle identification by means of the pulse shape analysis. It was developed for measuring activity of a neutron reactor. In this case the device has to be able to filter out the photon background with a rate several orders of magnitude higher than the neutron rate. Overall detected rate in a neutron reactor can easily exceed  $10^8$  particles  $\text{cm}^{-2}\text{s}^{-1}$ , depending on the distance of the detector from the reactor core. The device has to be able to cope with such high rates. It also needs to be dead time free or at least close to that, to minimise the counting error. At these rates, it still has to be able to identify the types of pulse. This type of online analysis cannot be done in software. It has to be implemented in an FPGA.

## 5.1 Motivation

Pulse shape analysis (PSA) is a common software tool for analysing sensor response to incident particles. It is usually done by means of software that runs over big amounts of data that have been acquired and saved to storage. This offline analysis can be repeated and improved. However, the saved data take up a lot of storage space. In addition, saving raw waveform data requires a system capable of a high data throughput and fast data storing. For instance, an oscilloscope can save up to 100 signal waveforms per second. This means that there is a high measurement dead time. To avoid the high dead times, the software algorithms can be ported to the FPGA where they analyse the incoming signal in real time. The signal is then discarded and only the analysis results are saved, decreasing the storage space significantly.

The offline pulse shape analysis has already been used for particle identification with a diamond sensor [67, 68]. An effort has been made to implement an online and real time application for this analysis by porting the algorithms into an FPGA. This section first describes the device specifications. Then it describes in detail the PSA algorithms and the structure of the code. Afterwards it discusses the performance results, which showcase the limitations of the device. Finally it describes the data acquired with radioactive sources and in neutron reactors.

## 5.2 Requirements

Chapter 3 shows that the shape is heavily dependent on several factors, such as environmental temperature and received irradiation dose. At temperatures lower than 150 K the signal from an  $\alpha$  starts deteriorating due to recombination of charges in the charge cloud. Sensor irradiation, on the other hand, introduces charge traps, which cause the signal to decay exponentially. These two factors are a significant limitation for particle identification. Priming can improve the charge collection and longterm stability of the pulse shapes. To improve the measurement further, a high bias voltage has to be applied, increasing the measurement SNR.

Factor	Operating range
Sensor material	sCVD diamond
Sensor thickness	500 $\mu\text{m}$
Temperature	150 K – 400 K
Radiation dose	$1 \times 10^{13}$ neq $\text{cm}^{-2}\text{s}^{-1}$
Charge carriers	holes
Bias voltage	$\sim 1 \text{ V } \mu\text{m}^{-1}$
Signal-to-noise	5

Table 5.1: Limitations to particle identification.

### 5.3 Device specifications

The ROSY box has a single BNC input with the termination  $50\ \Omega$  or  $1\ M\Omega$  with a DC or AC coupling. The analog chain has a 250 MHz bandwidth limit. The input range can be set from  $\pm 50\text{ mV}$  up to  $\pm 5\text{ V}$ . The signal offset can be set to any value within this range. The ADC samples this signal with an 8-bit precision at a rate of up to 5 GSPS. The PSA uses the highest sampling to achieve width measurement resolution of 0.2 ns. The spectroscopic application does not need such a fine timing resolution and therefore operates at a reduced sampling rate of 0.8 ns. The amplitude resolution depends on the chosen input range, but at 256 ADC counts per sample, it can be as low as  $0.39\text{ mV s}^{-1}$  at the range of  $\pm 50\text{ mV}$  and as high as  $39\text{ mV s}^{-1}$  at the range of  $\pm 5\text{ V}$ .

The logic structure of the PSA is designed using VHDL and runs on Xilinx Virtex 5. The PSA is capable of a maximum counting rate of  $1.56 \times 10^8$  pulses per second, yielding a 6.4 ns double pulse resolution. The analysis is more time consuming; the maximum throughput rate of the pulse shape analysis is  $\sim 5 \times 10^6$  pulses per second. This means that after every pulse, the device has a dead time of approximately  $(200 \pm 15)$  ns, depending on the width of the pulse being analysed. Any pulse arriving during the analysis of the previous one is counted, but not analysed. Any two pulses with the distance between the rising edges lower than 6.4 ns are counted as a single pulse.

The device is very sensitive to noise pick-up. Therefore the setup must be designed to minimise the pick-up by means of proper shielding, use of high-quality cables etc. The relatively low bandwidth limit filters out some high-frequency noise, but not the ringing or higher noise spikes. That is the task for the PSA.

### 5.4 Pulse parameters

A signal pulse on the input is parametrised during the analysis process. The PSA measures its amplitude, area, width and the slope of its falling edge, as shown in figure 5.1. The amplitude is the difference between the baseline and the highest sample in the pulse and is given in ADC counts as an 8-bit value. The area is defined as the sum of amplitudes of all samples between two defined boundaries within the pulse. The width is defined as the number of samples with a value higher than a set amplitude threshold. If the threshold is at half the maximum amplitude, the resulting width is *full width at half maximum* (FWHM). The falling slope is the maximum negative difference between values of two samples and is given in ADC counts per sample. These parameters can also be used as *qualifiers* for accepting or discarding a pulse. All four parameters limited by the low and high limit are called a *qualifier set*. For instance, a rectangular pulse by an  $\alpha$  particle always has the same FWHM and a very steep slope. In comparison, a photon has a lower falling slope value and a narrower FWHM. Therefore the low and high cut on these two qualifiers allow for a discrimination between the two pulses. Another qualifier is a *form factor* and is defined as the ratio between the measured area and the amplitude multiplied by the width. By

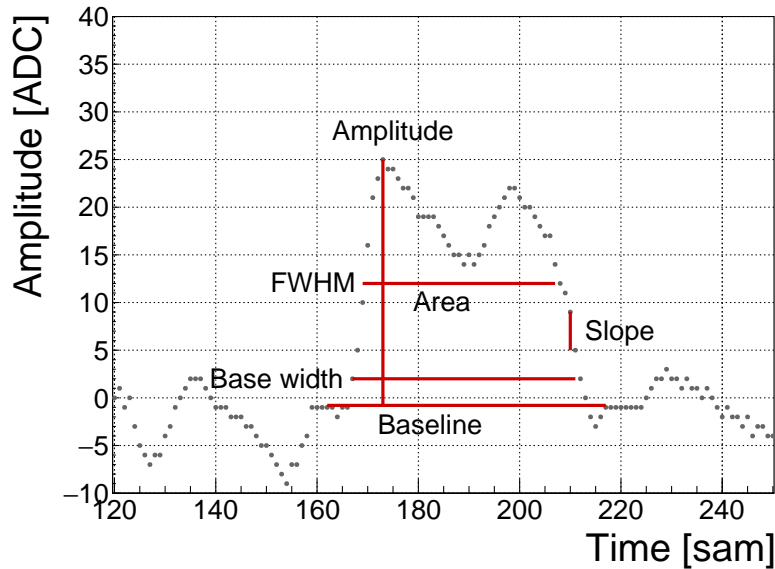


Figure 5.1: A pulse and its parameters.

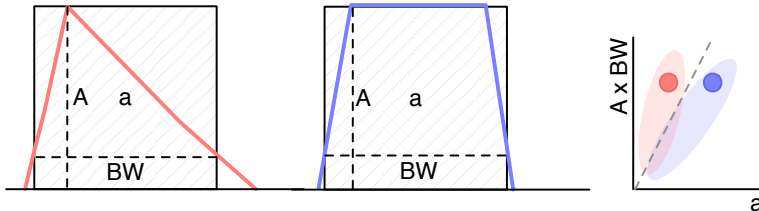


Figure 5.2: Form Factor is the ratio between the measured area ( $a$ ) and the calculated area ( $A \times BW$ ) of the pulse. The calculated area is significantly larger than the measured area for a triangular triangular pulse, but less so for the rectangular one. The red and blue dot in the right plot are the value entries of the two pulses shown. The red and blue oval shapes depict the regions for the values expected from triangular and rectangular pulses. By carefully choosing the linear qualifier (dashed line) and taking only the entries below the cut rectangular pulses can be identified.

comparing the measured and the calculated area the difference between a triangular and a rectangular pulse can be inferred, as shown in figure 5.2.

## 5.5 Applications

The FPGA firmware is designed for systems instrumented with CIVIDEC amplifiers and CIVIDEC sVCD diamond detectors. Three applications are available: *Spectroscopy*, *Pulse Shape Analysis* and *Counter*, each optimised for a specific task. Their capabilities are described below. The firmware runs in ROSY, a readout system produced by CIVIDEC.

**Spectroscopy** is a tool for measuring energy spectra of radioactive sources. It is used in combination with the CIVIDEC Cx spectroscopic charge amplifier. The signal from the

charge amplifier is analysed in real time. The FPGA measures the maximum amplitude of the signal. The amplitude value is ready at the end of the pulse and is stored in the amplitude histogram. Immediately after, the analysis is reset and the system is ready for a new acquisition. Upon request from the software, the histogram is read out, during which the analysis is paused. In addition to the histogram building, the firmware can also store raw pulse waveforms, which can be then read out by the software. The maximum allowed throughput is 1 million counts per second.

**Pulse Shape Analysis** is a tool for measuring energy spectra of radioactive sources, with an additional feature. It can identify the type of radiation detected by the diamond detector. By means of the pulse analysis it can subtract the background radiation and only measure the signals from the defined radiation source. It is used in combination with the CIVIDEC C2 fast current amplifier. The firmware receives a current pulse from the detector and digitises it. The pulse is then analysed and parametrised. The analysis module measures its maximum amplitude, full width at half maximum (FWHM), baseline amplitude, falling slope and its area. Then it compares the obtained pulse parameters with the qualifiers set by the software and determines what type of radiation hit the diamond detector. Depending on the qualifiers, the pulse can either be *accepted* or *rejected*. The firmware then stores the parameters of the analysed pulse into histograms. Two histograms exist for each parameter: one for all pulses and one for accepted pulses. In addition, there is one 2D histogram (a scatter plot), which can plot two parameters one with respect to the other. Upon request from the software, all histograms are read out, during which the analysis is paused. The maximum allowed throughput is 1 million counts per second.

**Counter** is a tool that measures the count rate and the mean time during counts. It is used in combination with the CIVIDEC Cx, C6 or C2 amplifier. It contains one histogram which holds the information about the mean time during counts. The counter is operational also during the readout of the histogram. The highest counting rate with enabled histogram writing is  $3 \times 10^7 \text{ s}^{-1}$ .

## 5.6 Description of the firmware

The applications are built on top of the Picotech platform. The base code handles the communication between the software and the hardware. Furthermore, it provides the interface to the ADC data, the input/output registers and the USB data transfer. The applications have a set of modules that handle the data input and output and a module for signal analysis, as shown in figure 5.3. The data handling modules are very similar in all the applications to ensure compatibility of the communication between software and firmware and the readout data format. The analysis module, however, is different from one application to the other. The data handling layer is the same for all applications and consists of the final state machine (FSM), the histogram builder, the raw signal handler, the USB FIFO buffer and the register array.

## 5.6. DESCRIPTION OF THE FIRMWARE

---

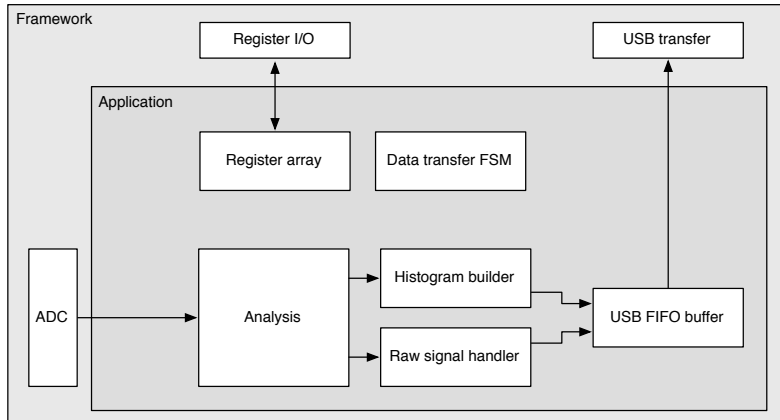


Figure 5.3: Firmware design structure.

The firmware is written entirely in VHDL. The diagram in figure 5.3 shows the module architecture. The ADC provides the module with 32 digitised signal samples every clock cycle (6.4 ns). The signal is routed directly to the pulse analyser and into the raw signal handler. The analyser outputs are connected to the I/O registers and to histogram buffers. Both the histogram buffers and raw signal buffers are connected to the USB FIFO through a multiplexor. The firmware communication to the controller is done via input/output (I/O) registers (control and status registers, counters) and serially via USB (histogram data, waveforms).

### 5.6.1 Design constraints

**Speed** The ADC provides 32 8-bit samples on every 6.4 ns clock cycle. It is not possible to e.g. sum all 32 values in a single cycle, because the summation takes too long to complete. This is why the summation has to be pipelined and carried out in three cycles. This adds up to the analysis duration, which in turn decreases the maximum pulse rate.

**Firmware size** The PSA application makes use of a number of FIFO and RAM buffers to store the pulse waveforms and histograms. 48 32k block RAM modules have been used for the implementation, maxing out the available block RAM memory space on this FPGA. The analysis algorithm also takes up a significant portion of the FPGA. Many of the operations are carried out on 256-bit long numbers received from the ADC, which quickly fills up the available logic. This is also why the place and route procedure takes a long time.

**Power consumption** The reduction of the power consumption is not crucial for the intended applications.

### 5.6.2 Analysis module

This module is different for different applications. The Pulse Shape Analysis (PSA) application has the most complex module design. The spectroscopy application only uses a

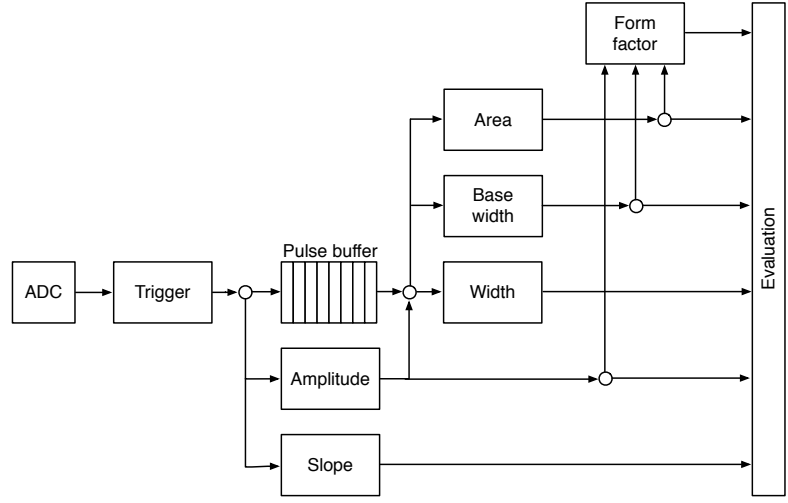


Figure 5.4: Code design plan.

small part of that design and the Counter application an even smaller one.

The analysis (or parametrisation) is carried out in several steps, as shown in figure 5.4. The triggering block starts the readout upon signal threshold crossing. The maximum slope of the falling edge is observed. The Amplitude block calculates the pulse height and retains the maximum amplitude while pushing the signal into the pulse buffer. Then the entire pulse is clocked out of the buffer while its FWHM, baseline width and area are measured. Finally, the Form factor is calculated. At the end the Evaluation block takes in all the parametrised information and classifies the pulse according to user-defined cuts.

**Triggering** module handles signal polarity swapping, triggering on threshold and defining the trigger window. The real-time processing algorithm allows for a positive or an inverted input signal. However, the PSA only handles positive-polarity pulses. Therefore a negative signal is swapped in the *triggering* block. Signal analysis and readout are then triggered when the signal crosses a user-defined threshold. In addition, the signal has to be over the threshold for a defined number of samples. This is to avoid triggering on noise spikes. A double clock cycle delay is used on the signal to make sure that the recorded signal window includes the rising edge of the pulse as well as some baseline before it. A *trigger active* signal marks a window that contains the entire pulse including some baseline signal before and after it. The trigger can be vetoed by three signals: if the pulse analysis is still taking place, if the input signal exceeds the maximum voltage range or if the data transfer FSM is pausing the analysis due to data transfer to the controller.

**Amplitude** block calculates the pulse height from the difference between the pulse and the baseline. It also finds the position of the maximum amplitude within the clock cycle. It receives 32 8-bit samples from the triggering block every clock cycle. Time delays in the logic prevent it to find the maximum value of the 32 samples within one clock cycle (6.4 ns).

## 5.6. DESCRIPTION OF THE FIRMWARE

---

Therefore the decision logic has been pipelined in three stages, which means that the final maximum value is ready three clock cycles after the end of the pulse.

**Pulse buffer** is a FIFO that stores the signal while its amplitude is being measured. At the end of the pulse the FIFO is read out so that the remaining measurements can take place.

**Width** block uses the maximum amplitude to determine the *half-maximum* and to measure the FWHM. To do so, it counts the samples that are above the half-maximum amplitude. However, this method might also count high enough noise spikes before or after the pulse. Hence an improved method, which “cleans” the measurement of unintentional additional noise, has been implemented. It is described in section 5.6.3.

**Baseline width** block is the same as the Width block, but it measures the width either at 50 %, 25 %, 12.5 % or 6.25 %, depending on the setting in the register. It also makes use of the special method described in 5.6.3 to avoid overestimations due to including noise in the measurement.

**Area** block measures the pulse area by summing up the amplitude values of the samples in the pulse. The boundaries of the summation are defined with the crossing of the amplitude above a certain threshold. Only the samples between those boundaries are summed up. The boundaries can be set at 50 %, 25 %, 12.5 % or 6.25 % of the maximum amplitude of the pulse. The area measurement makes use of the same routine as the FWHM and Baseline width block to remove the potential outlying samples.

**Falling slope** block measures the highest negative difference between amplitudes of two adjacent samples, thus getting the maximum negative slope of the pulse. It is an experimental routine, only used for academic purposes.

**Form factor** block is used as a special qualifier for particle identification. It compares the weighted measured area of the pulse with its weighted calculated “form”, which is defined as the multiplication of the measured amplitude and baseline width. The equation is as follows:

$$x \cdot a - y \cdot A \cdot BW \geq 0, \quad (5.1)$$

where  $a$  is the measured area,  $A$  is the amplitude,  $BW$  is the baseline width and  $x$  and  $y$  the weighting factors for the measured and calculated area, respectively. The output of the block is the boolean result of this equation.

**Evaluation** block takes in all the parameters from the analysis blocks and compares them against the user-defined qualifiers. If the parameters are within the bounds, the pulse is accepted, otherwise it is rejected. The corresponding counters within the block are incremented.

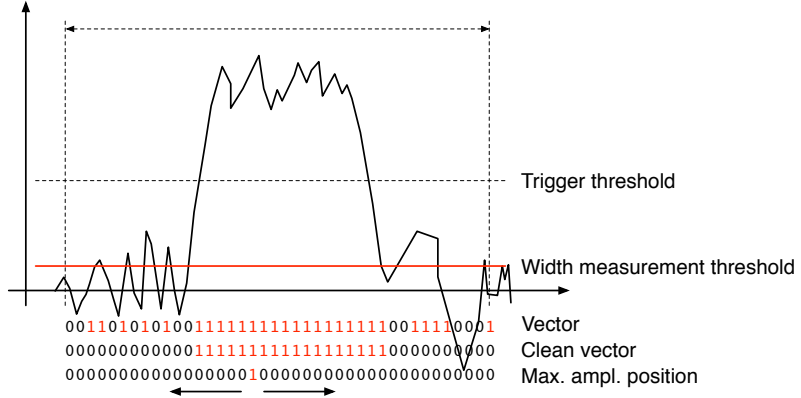


Figure 5.5: A sample pulse. The first vector shows which samples are above the width measurement height. The second vector is a clean vector. The third line shows the position of the maximum amplitude. The vector cleaning algorithm starts from the maximum amplitude and continues in both ways along the vector.

### 5.6.3 Area and width measurement

The routine for measuring pulse area and width must have a specific algorithm implemented to carry out the measurements correctly. The core point is that the routine precisely defines the edges of a pulse. It does so by means of *vector cleaning*, presented in figure 5.5. An important input, beside the ADC data and the measurement threshold, is the position of the sample with the highest amplitude.

The signal arrives from the ADC as a set of 32 8-bit samples every every clock cycle with a period of 6.4 ns. All 32 samples are compared against the width measurement threshold. If a sample value is equal or higher than this threshold, a binary 1 is set in a 32-bit *vector* on the position corresponding to the position of the sample in the incoming ADC data set. The resulting vector might also include some noise at the edges of the pulse, depending on the height of the width measurement threshold. The old routine simply counts the binary ones in this vector to get the pulse width. This works well for measuring the FWHM because the threshold was high. However, for width measurements at 25 %, 12.5 % or 6.25 % of the pulse height this might already become a problem, because the noise might be counted in as well. This is why the new routine cleans the outliers in this vector before counting the remaining ones in the clean vector.

The routine starts from the position of the maximum height. It follows the vector in both ways and finds the first falling edge (0 at this position and 1 at the previous one). From there on it rewrites any binary 1 with a binary 0. The resulting clean vector only has one bunched set of binary ones which are summed, yielding a precise pulse width. The area measurement is similar - it only integrates over the samples marked in the clean vector. Both measurement routines, for area and for width, are implemented separately so that the area routine can have a different threshold set.

This section explains how the algorithm is designed. First, the idea for it was tested

## 5.6. DESCRIPTION OF THE FIRMWARE

---

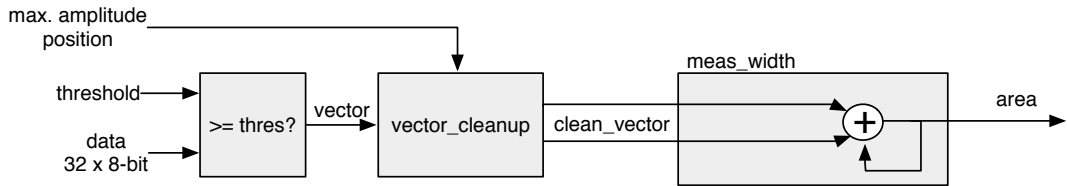


Figure 5.6: This block counts the remaining binary ones in the clean vectors and outputs this value as the pulse width.

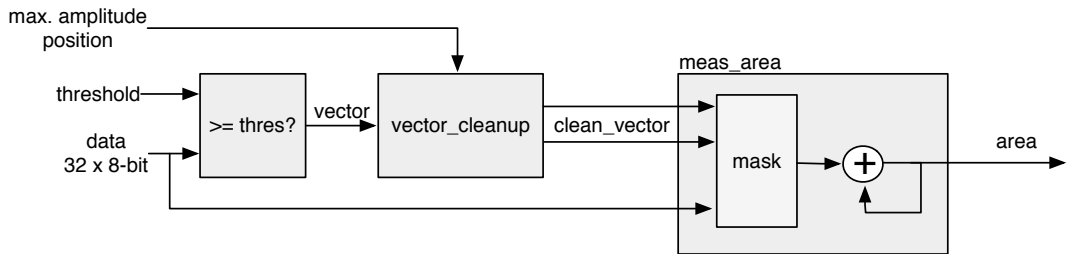


Figure 5.7: This block masks the input data with the clean vector and sums the remaining samples.

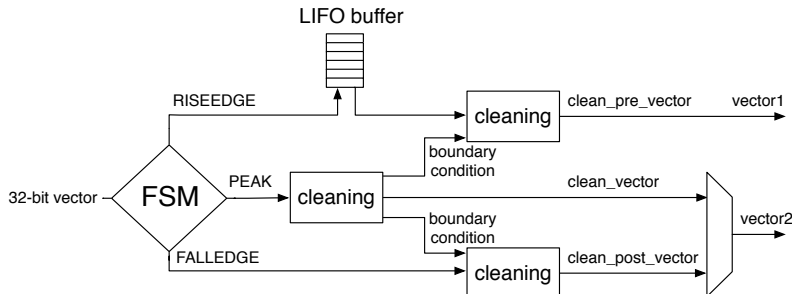


Figure 5.8: Vector cleaning routine outputs two vectors - one forward in time and one back in time from the peak of the pulse.

using Excel and was only afterwards ported to the VHDL. The underlying algorithm first cleans the vector. Then it passes the cleaned vector either to the width or area measurement, as shown in figures ?? and ???. The width measurement module only sums the ones in the vector whereas the area measurement module sums the data samples marked by the cleaned vector. Both modules issue a *valid* signal when they finish the measurement.

### 5.6.3.1 Vector cleaning

This is the most important block. Its inputs are: *vector*, *parsing active*, *position of the max. amplitude (PA)* and *its delay (DA)*. PA is a 32-bit binary number that shows the position of the sample with the maximum amplitude within the data block whereas the DA tells us how many clock cycles after the start of the parsing this PA block is. The

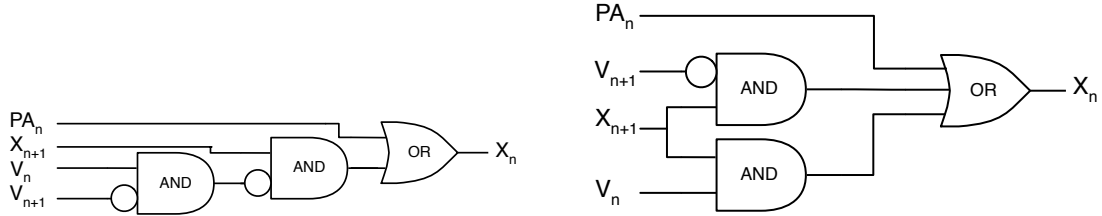


Figure 5.9: One logic step in the algorithm chain before and after Karnaugh minimisation.

vector cleaning module is designed as a final state machine (FSM) with the states IDLE, RISEEDGE, PEAK, FALLEDGE and READY. The FSM is idle until it receives the *active* signal from the external module, marking that the vector parsing has commenced. It switches to RISEEDGE, which starts two procedures: 1) it fills the vector of the pulse's rising edge into a last-in-first-out (LIFO) buffer and 2) counts down from the DA value. When this counter reaches 0, the FSM changes its state to PEAK because the current vector on the input is the one containing the maximum amplitude. This data block is sent through the *peak algorithm*, which cleans the vector. The FSM switches to FALLEDGE state. Now both the previously buffered vector of the rising edge and current vector of the falling edge go through the *pre- and post- algorithm* where they are cleaned, but they get their boundary conditions from the *peak algorithm*. The output of this module is therefore two cleaned vectors in parallel – one forward in time and the other backwards.

#### 5.6.3.2 Algorithm

The underlying algorithm is sequential - it carries out a logic operation on vector bit on position 0, uses the output of this operation for the operation on bit on position 1 and so on. This means that it has to carry out 32 logic operations per clock cycle. With each operation taking approximately 0.3 ns, the entire logic chain takes approximately 10 ns to complete. With only 6.4 ns per clock cycle, this means timing errors would occur. To fix the problem, a more complicated *decimated algorithm* has been designed. It consists of two parallel logic chains. Each of the two only takes every second bit into account (chain one: 0, 2, 4 ..., 30. Chain two: 1, 3, 5 ..., 31). This makes the chains effectively 16 bits long. The algorithm is run on the two chains and the results are merged together at the end as shown in figure 5.10. This effectively reduces the number of sequential logic operations to around 18, which is within the timing constraints.

## 5.7 Control and data interface

Communication between the device and the controller PC is done via the API functions provided by the producer. In addition, the API used by CIVIDEC has access to several extra functions. These allow the user to download a customised bitfile to the FPGA, access

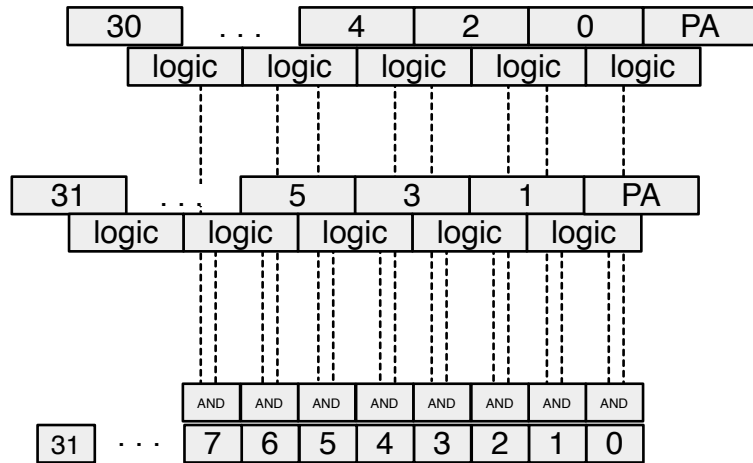


Figure 5.10: Vector is divided into two 16-bit logic chains. The algorithm logic is then run on the two chains separately. The results are then merged into one 32-bit clean vector by using a set of AND gates.

the I/O registers and use the USB data transfer.

### 5.7.1 Software

The software has been designed in C++ in several levels of abstraction. Figure 5.11 shows the structure of the classes. The classes Device, PSA and RawSignalHandler are there to make it easier to read and understand the controller code. In principle the PSfunctions can also be accessed directly by the controller, but for this the instruction sequences must be well known and understood.

### 5.7.2 Data readout

The device records the data in two forms - as signal waveforms and as histograms of analysed pulse parameters. Both are available upon request from the controller. Only one of the two can be transferred via the USB line at a time.

The waveforms are saved into a FIFO buffer, which can hold up to 64 pulses of the length of  $\sim 500$  samples. The data format for each pulse is such that it starts with a header containing the pulse timestamp and the sequential number, continues with the data samples and ends with a header containing all the measured parameters (width, amplitude, area, falling slope and form factor). When the FIFO is full, it issues a flag, which tells the controller that the data buffer is ready for readout.

The histograms are implemented into the FPGA's Block RAM. Their size ranges from 256 to 4096 bins (an 8-bit or a 12-bit histogram, respectively), depending on the required histogram resolution. For instance, the width parameter is measured with a 0.2 ns resolution; the expected maximum pulse width is less than 20 ns. This yields the maximum range

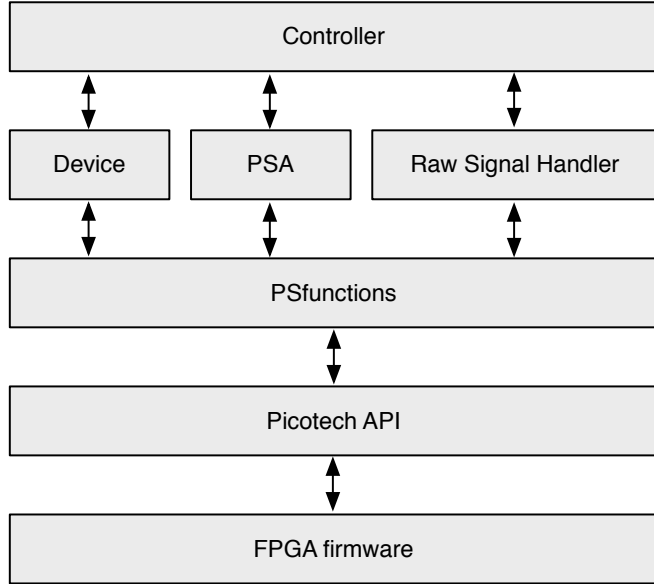


Figure 5.11: Abstraction levels of the controller software.

of 100 bins, making an 8-bit histogram sufficiently large. The same reasoning is applied to the amplitude measurement. In this case the maximum range is defined by the 8-bit resolution of the ADC. The area measurement, however, yields higher values and can therefore have a more refined binning (12-bit). Finally, a single 12-bit 2D histogram is included, with 6 bits for every axis. It is used as an online scatter plot for comparing one measured parameter to another. An example for it is a comparison of the width against the area, which can help the user determine the cuts that need to be applied to the measurement.

## 5.8 Performance results

The device has been tested in the lab using a pulse generator as well as several radioactive sources. The results show that: 1) the amplitude, area and width measurement are linear across all input ranges, 2) the highest rate of the PSA algorithm is  $\sim 5 \times 10^6$  pulses per second and 3) the lowest SNR where the algorithm still functions is  $\sim 5$ .

**Trigger rate** A pulse generator was used to verify the highest achievable rate at which the PSA still analyses every incoming pulse. The final state machine implemented in the pulse analysis module prevents the triggering block from issuing a trigger due to an incoming pulse if the previous analysis is still in ongoing. Given that all the pulses were of the same length, the analysis duration was always the same. When the time between the incoming pulses was shorter than the time of the analysis, the pulses were not analysed. Figure 5.12 shows the sharp decline in the percentage of the analysed pulses when reaching the rate of 5 MHz. Therefore the overall analysis duration for a 10 ns pulse is approximately 200 ns.

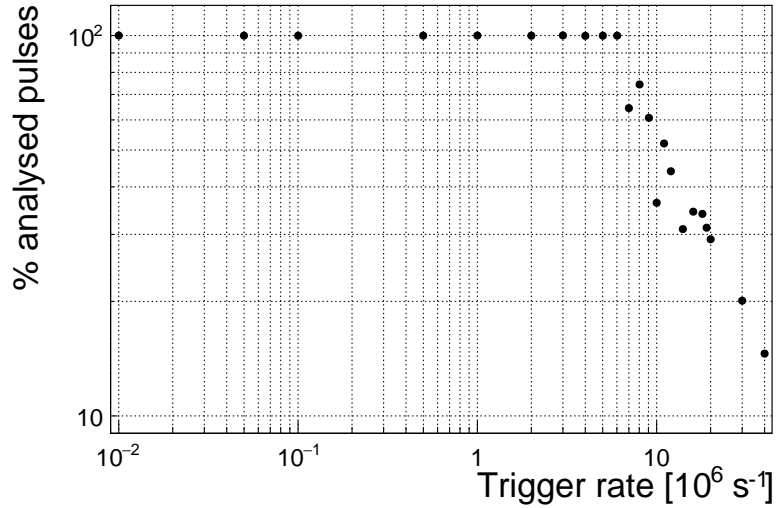


Figure 5.12: This figure shows the capability of the device to analyse all arriving pulses for a range of input frequencies. The highest achievable rate with zero lost pulses is  $5 \times 10^6 \text{ s}^{-1}$ .

**Linearity** A pulse generator was used to verify the linearity of the measurements across all input ranges. Pulse width and amplitude were varied and measured both with the oscilloscope and the PSA to check for non-linearities or inconsistencies in the PSA measurements. The resulting plots in figures ?? and 5.13c show that the PSA measurements agree well with those from the oscilloscope. The major inconsistency is observed in the lower range of the plots. It stems from the fact that the bandwidth limit of the PSA is lower than that of the oscilloscope, which affects the pulse shape. Effectively, the PSA cannot measure the rectangular pulses of the width smaller than 2 ns.

**Stability** The input pulse signal was superimposed with white noise generated by a noise generator with a variable gain. The mixed signal yielded pulses with an SNR ranging from 5 (very noisy) to 100 (noise negligible). The PSA then performed the pulse parametrisation at different SNRs. The resulting plots in figures 5.13b, 5.13d and 5.13e show that the pulse width measurement is stable even for low SNR whereas the amplitude measurement is affected significantly. This stems from the analysis taking the highest sample as the pulse's amplitude. The area measurement, being effectively the integrated amplitude across the pulse, is also affected by the faulty amplitude measurement. Nevertheless, the mean area remained the same. This means that the added noise only affects the resolution of the spectrum, not its position.

### 5.8.1 Comparison between the charge- and current-sensitive spectroscopy

The calibration was done using a  $^{148}\text{Gd}^{239}\text{Pu}^{241}\text{Am}^{244}\text{Cm}$  source which emits  $\alpha$  particles with four different energies. The PSA in combination with the current amplifier was compared against the 8-bit spectroscopic application in combination with the charge amplifier and a commercial 14-bit spectroscopic readout.

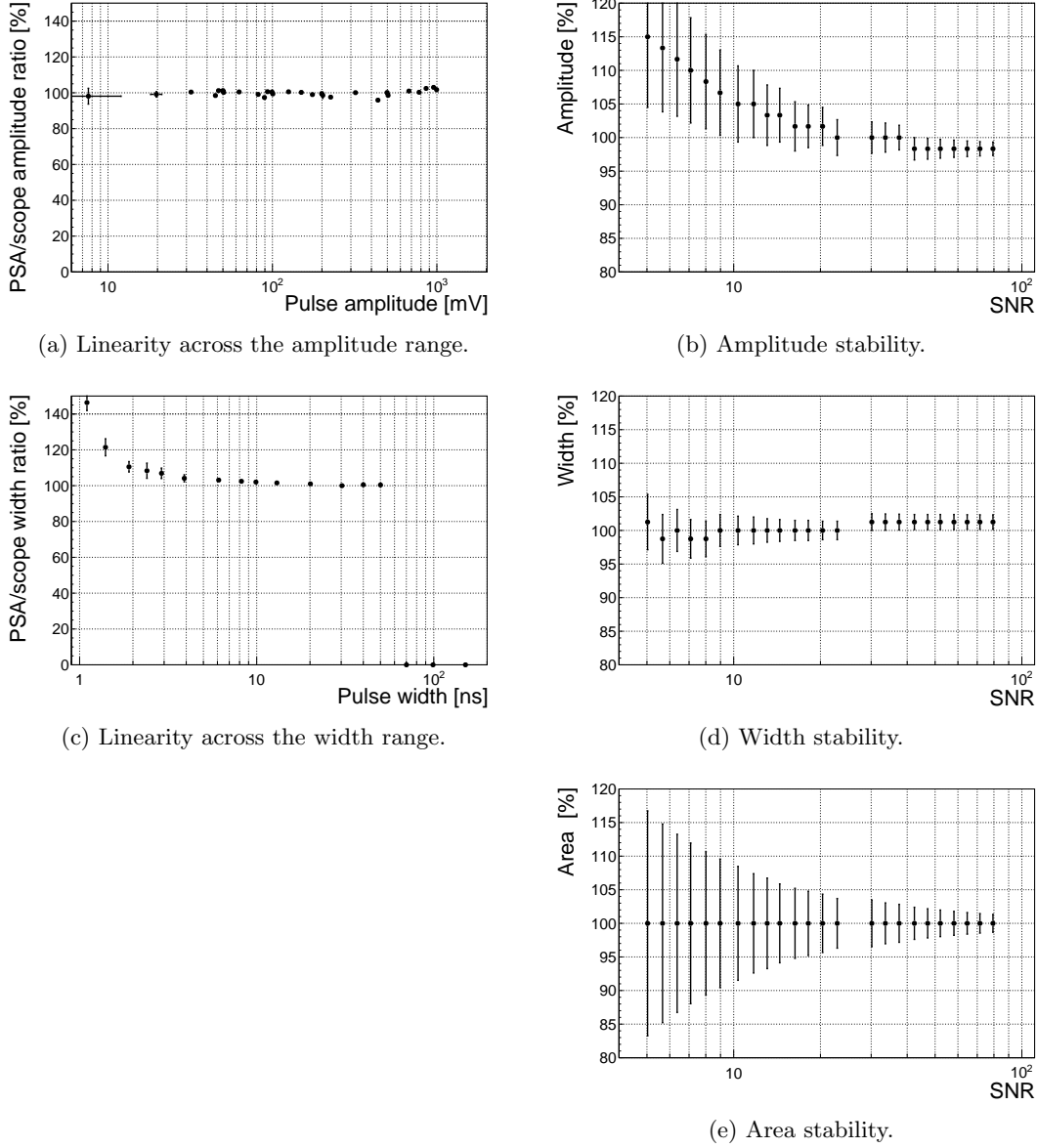


Figure 5.13: These diagrams show the linearity of the measurements and their stability with respect to analog noise.

The  $^{241}\text{Am}$  peak measured by the Cx amplifier has an RMS of 0.8 ADC, which corresponds to a 32 keV energy resolution. For comparison, the C2 amplifier measures this peak with an RMS of 1.9 ADC, which corresponds to a 75 keV energy resolution. Therefore the energy spectrum measured by the current amplifier has a lower energy resolution.

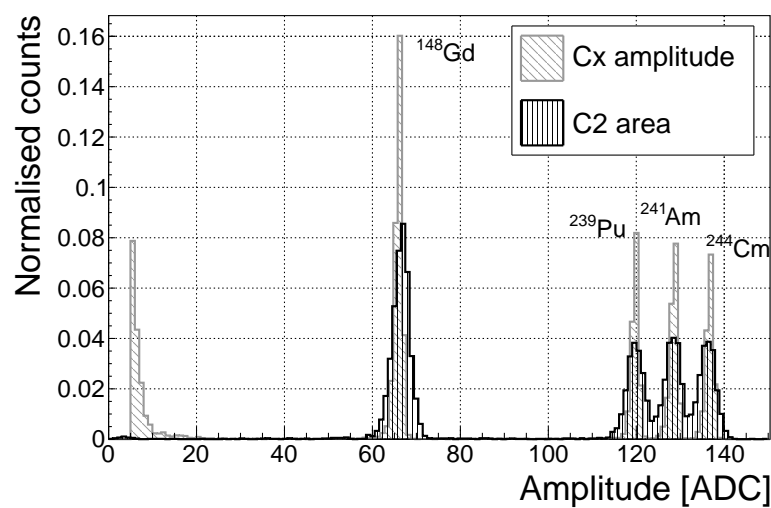


Figure 5.14: Spectrum of a  $^{148}\text{Gd}^{239}\text{Pu}^{241}\text{Am}^{244}\text{Cm}$  source using a Cx and a C2 amplifier.

## 5.9 Source calibration

The operation of the pulse shape analysis has been tested using several radioactive sources. In particular, an  $\alpha$ , a  $\beta$  and a  $\gamma$  source have been used. Each source has been placed on top of the diamond detector and left for a predefined time depending on its activity. Table 5.2 shows the sources used, the time of exposure and their rate during this time. The data for the  $\alpha$  source have been taken for both polarities. In addition, a long run with an  $\alpha$  source with a sheet of paper in between the source and the diamond has been taken. The paper stops the  $\alpha$  particles but lets through the photons, which helps to estimate the background photon radiation of the source.

Run	Source	Radiation	Energy [MeV]	Time [h]	Triggers	Rate [ $s^{-1}$ ]	Bias [V]
1	$^{241}\text{Am}^*$	$\alpha$	5.5	60	958	4.4e-3	500
2	$^{241}\text{Am}$	$\alpha$	5.5	17	10558	0.17	500
3	$^{241}\text{Am}$	$\alpha$	5.5	18	11454	0.18	-500
4	$^{90}\text{Sr}$	$\beta$	2.3	0.42	1.07e6	1000	500
5	$^{60}\text{Co}$	$\gamma$	1.3	0.28	1.34e6	3300	500
6	$^{239}\text{Pu Be}$	$n$	1-10	2.5	1.5e6	230	500

Table 5.2: Measurements carried out at Atominsttitut.

The pulses acquired during the data taking are shown in persistence plots in figures 5.15. Figure 5.15a showing the  $^{241}\text{Am}$  source background reveals that the diamond detector had been contaminated, probably with chipped-off grains of the unsealed source. This stems from the fact that  $\alpha$  pulses are recorded despite having a sheet of paper, which stops all the particles emitted by the source. However, the number of  $\alpha$  hits due to contamination is negligible - an estimated  $1\text{ h}^{-1}$ . Another point worth noting is the falling slope of the rectangular pulse in figure 5.15c. This stems from the space charge that had built up during the neutron irradiation and is discussed in section ???. Finally, figure 5.15f shows that the neutron source causes the widest variety of pulse shapes - triangular and rectangular as well as those in between. Pulse shapes caused by neutrons are described in detail in [69, 70].

## 5.9. SOURCE CALIBRATION

---

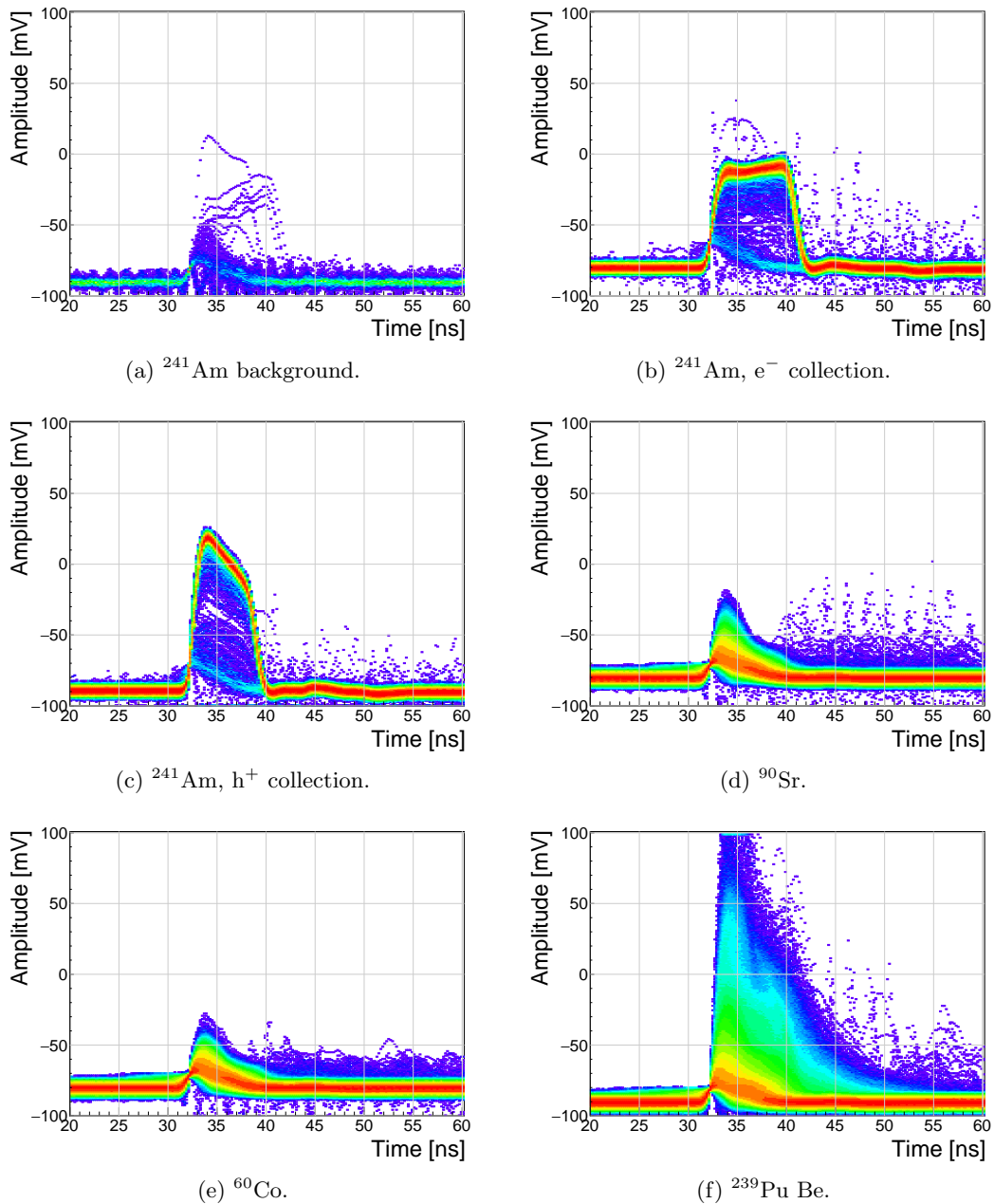


Figure 5.15: Accumulated pulses for all runs.

### 5.9.1 Source measurements – scatter plots

An online pulse shape analysis has been run on all the above mentioned data sets. The parameters of the pulses are plotted in 2D histograms - in form of scatter plots. The aim is to find a way to distinguish between the various types of radiation in order to only select the spectrum of a single type of particles from a spectrum of a mixed source. The energy spectrum is directly proportional to the measured area of the current pulses, therefore all the parameters are plotted against the pulse area. The parameters used are:

- FWHM
- Base width
- Amplitude
- Amplitude × Base width
- Base width – FWHM
- Falling slope

Every individual parameter can be attributed a set of qualifiers with which a certain part of the distribution can be rejected. There are two ways to apply the qualifiers. One is to set the minimum and maximum value for a specific parameter. The accepted pulses are those in between these two values. The minimum and the maximum qualifier are marked with a blue and a red line in the subsequent scatter plots. The second way is to apply a linear cut to the distribution in the scatter plot. The user can choose the slope of the line and to accept either the pulses above or below the line. The colour of the line is blue if the part above the line is accepted and red if opposite. Currently two scatter plots have this option implemented: area vs amplitude and area vs amplitude×base width. The latter represents the Form Factor, which is discussed in section 5.6.2.

The sets of plots in figures 5.16, 5.17, 5.19 and 5.20 show the above listed parameters plotted against the pulse area for  $^{241}\text{Am}$  background, electrons and holes,  $^{90}\text{Sr}$  and  $^{64}\text{Co}$  source, respectively. Any distinguishable difference between the plots of two sources would suggest that that particular parameter can be used to distinguish one type radiation from the other. For the most part the photons are considered the rejected pulses (greyscale colour palette) whereas  $\alpha$  particles or neutrons are accepted (yellow colour palette). In special cases only a certain types of neutron interactions are accepted, as depicted in section 5.10.

#### 5.9.1.1 $^{241}\text{Am}$ source

The source emits  $\alpha$  particles at  $\sim 5.5$  MeV and photons with a range of energies. Due to the losses in the air and the electrode the measured  $\alpha$  energy varies – between  $\sim 5$  MeV down to 1 MeV.

Figures 5.16 and 5.17 show the pulse area distribution with respect to the aforementioned parameters, for electrons and holes respectively. Focusing on the top left plot in figure 5.16,

## 5.9. SOURCE CALIBRATION

---

a distinctive horizontal stripe appears at a width of 9 ns, ranging from 100 up to 630 pVs. This is the aforementioned spread of  $\alpha$  energies. The shape of the pulse from this type of radiation retains the width even at smaller energies. Only its amplitude is decreased. This is because the free charge carriers in the diamond are traveling with the same speed in all cases, inducing rectangular pulses of the same widths.

The other cluster in the [area, FWHM] phase space comes from the background photons. The two clusters are far apart from one another with no overlap. It is therefore straightforward to define a cut in the FWHM to distinguish between the  $\alpha$  and  $\gamma$  entries. This is done by means of the minimum and maximum FWHM constant qualifier, which marked red and blue in the [area, FWHM] subfigure.

The [area, amplitude] subfigure also reveals two distinguishable clusters, which can be segregated using a linear qualifier. The angle of the  $\alpha$  stripes in the [area, amplitude] subplots is significantly smaller than that of the photon stripe. The separation is much less pronounced in the other subfigures.

There is a third barely distinguishable island visible in the top two plots, both area and width values close to zero. This island is formed by noise, which triggered the analysis.

The situation is similar when inverting the bias voltage and collecting holes, as shown in figure 5.17. Here, however, the two clusters are much closer together even in the [area, FWHM] subfigure. This makes it more difficult to define a clear border between the two. The other five qualifiers are in this case less important than the FWHM. Nevertheless, it can be deduced from the plots that the difference BW-FWHM must be below 4 ns.

The slope is dependent of the amplitude, which can be seen in the bottom right plot, making it an unreliable qualifier in the lower area range. The amplitude, scaling with area, makes a distinguishable straight line in the middle left subfigure.

The amplitude increase with area in the [area, amplitude] subfigure is similar for photons and  $\alpha$  particles. Therefore a linear qualifier can not be used to distinguish  $\alpha$  radiation from  $\gamma$  radiation when measuring holes.

Figures 5.18a and 5.18b show a one-dimensional area distribution of the acquired data for electron and hole collection. The blue histogram represents all collected data whereas the red one marks the data whereby the pulse parameters are within the qualifiers. In both figures the  $\alpha$  peak at 600 pVs is clearly visible, followed by a  $\gamma$  quasi-Landau distribution with an MPV of  $\sim$ 70 pVs and a noise peak at the very left of the area distribution. These two contributions have been rejected by the FWHM qualifier.

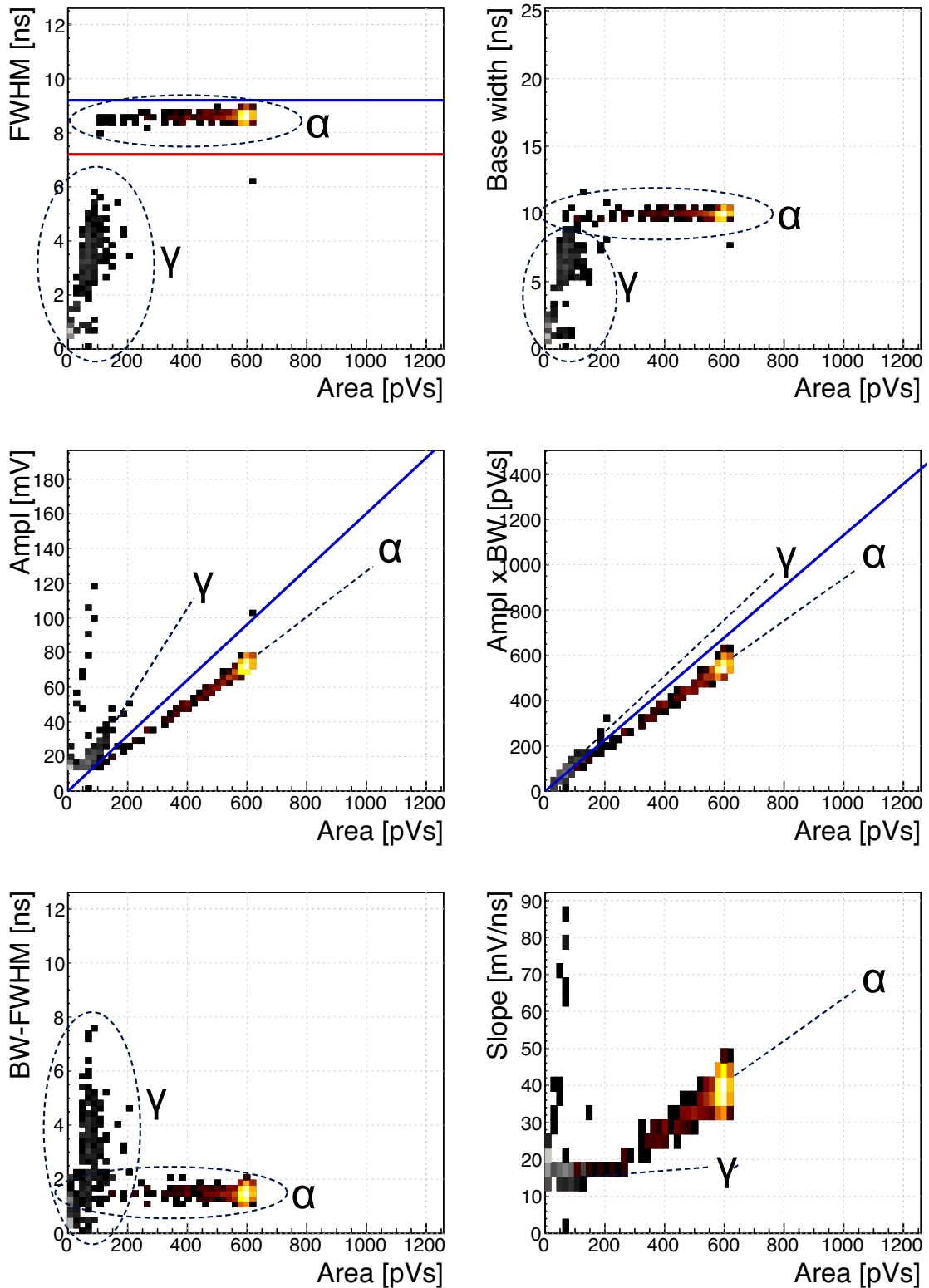


Figure 5.16:  $^{241}\text{Am}$ ,  $e^-$  collection. Qualifier: FWHM. Optional qualifiers: Amplitude, Form Factor.

## 5.9. SOURCE CALIBRATION

---

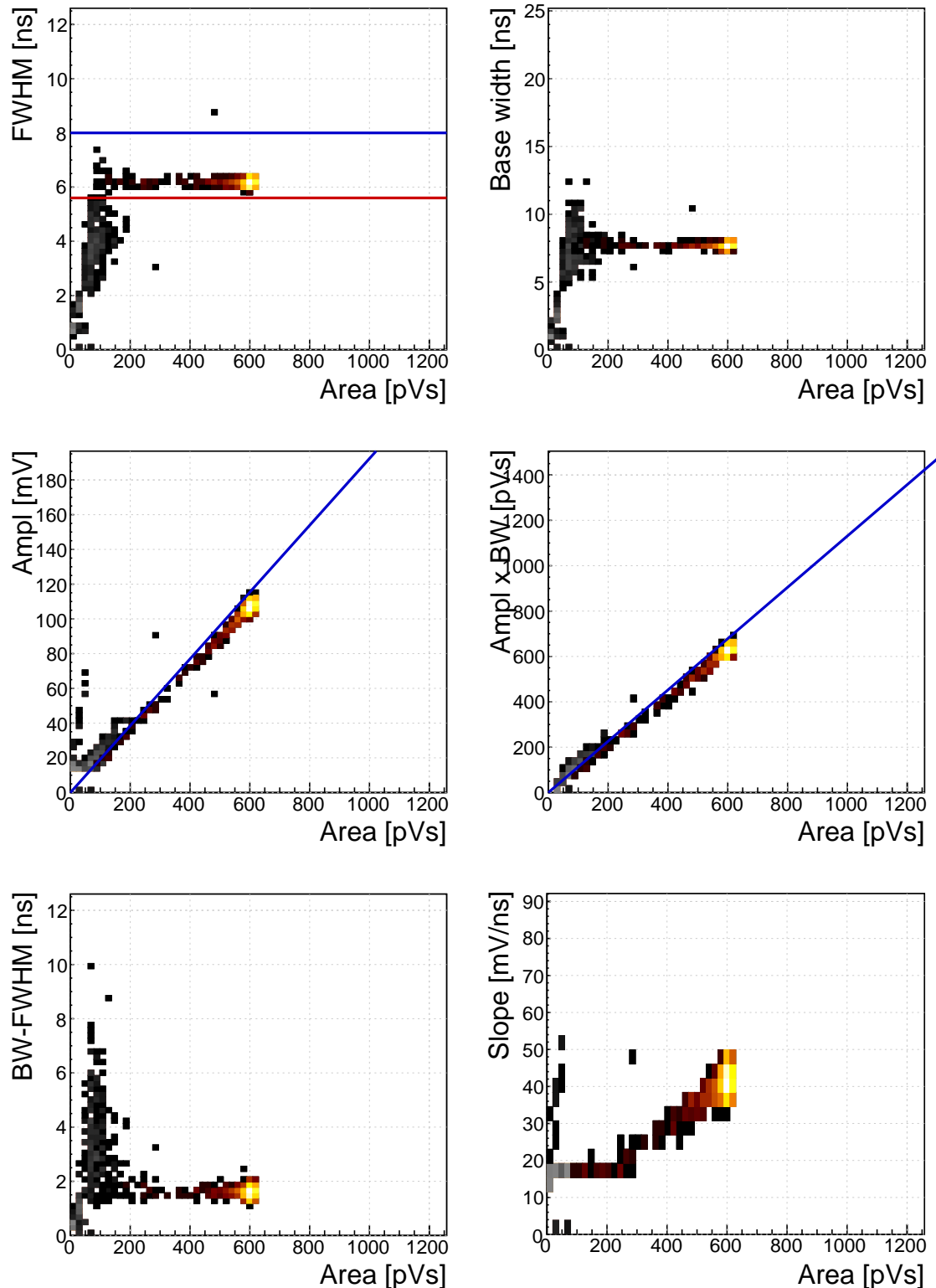
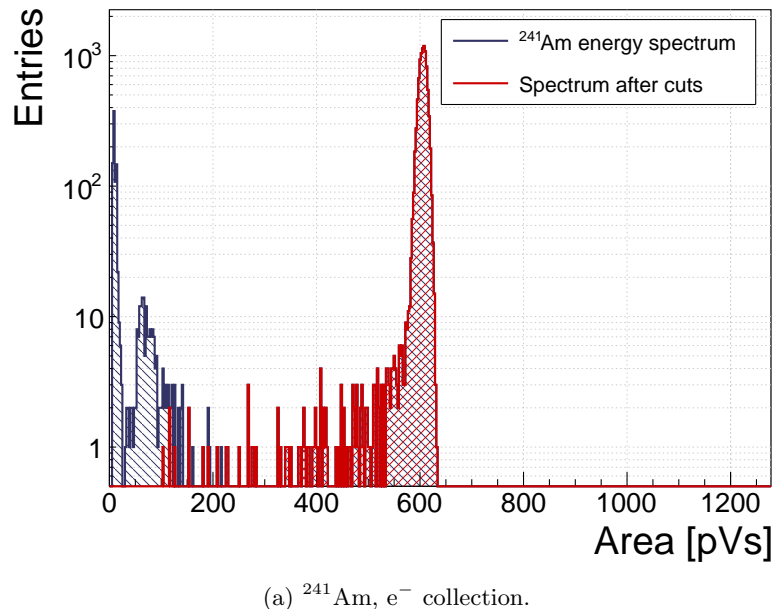
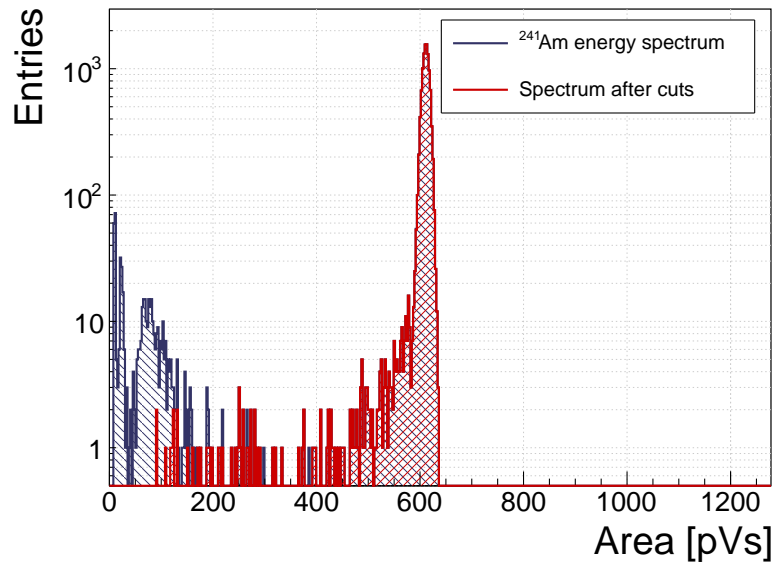


Figure 5.17:  $^{241}\text{Am}$ ,  $\text{h}^+$  collection. Qualifier: FWHM.



(a)  $^{241}\text{Am}, \text{e}^-$  collection.



(b)  $^{241}\text{Am}, \text{h}^+$  collection.

Figure 5.18:  $^{241}\text{Am}$  area histograms for electron and hole collection.

### 5.9.1.2 $^{90}\text{Sr}$ and $^{60}\text{Co}$ source

The phase space of the  $^{90}\text{Sr}$  source overlaps entirely with that of the  $^{60}\text{Co}$  source, as results from figures 5.19 and 5.20. This renders it virtually impossible to distinguish between photons and electrons (MIPs). Comparing the [area, FWHM] phase space of the photons and alphas and the high reach of the former, the electron collection of the alphas would need to be used to distinguish between the two types of particles.

The one-dimensional histograms in figure 5.21 show a quasi-Landau distribution with the MPV at  $\sim 70$  pVs, which is in agreement with the background  $\gamma$  radiation emitted by the  $^{241}\text{Am}$  source, as shown in figure 5.18 in the previous subsection. This is however not a pure Landau distribution. Relative to the 600 pVs  $\alpha$  peak, the expected MPV of MIPs would be  $\sim 30$  pVs, which is not the case in these distributions. This is because the PSA device is a self-triggering system, which cuts the lower energetic particles with the trigger threshold. The resulting distribution is therefore only the top portion of the real Landau distribution. Unfortunately this is the limitation of the device, governed by the analog noise of the current pre-amplifier.

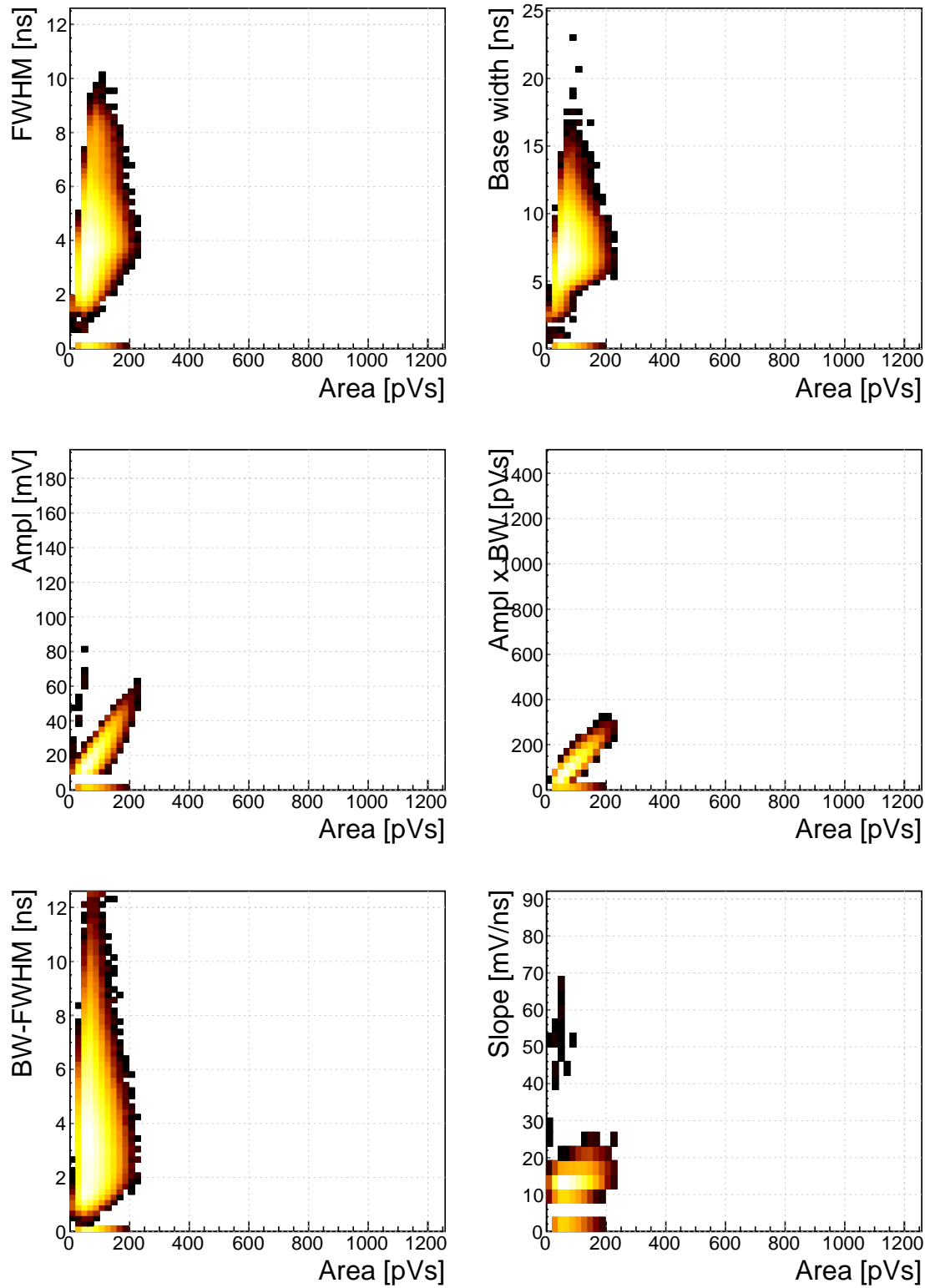


Figure 5.19:  $^{90}\text{Sr}$  scatter plots.

## 5.9. SOURCE CALIBRATION

---

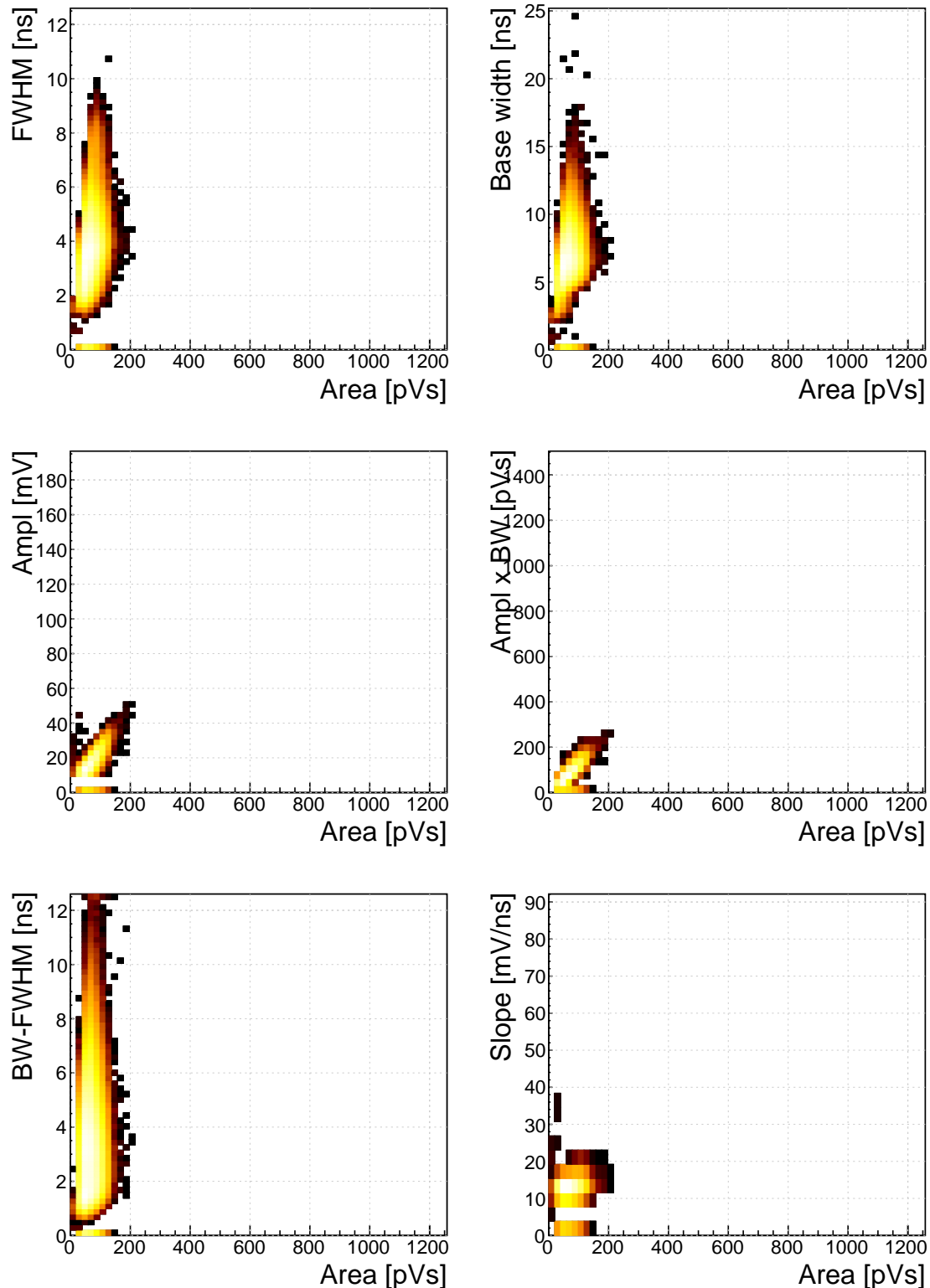
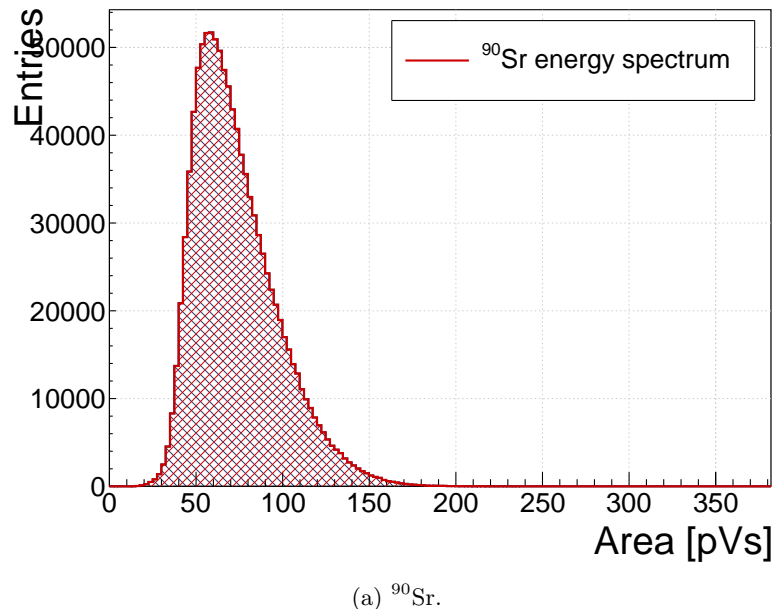
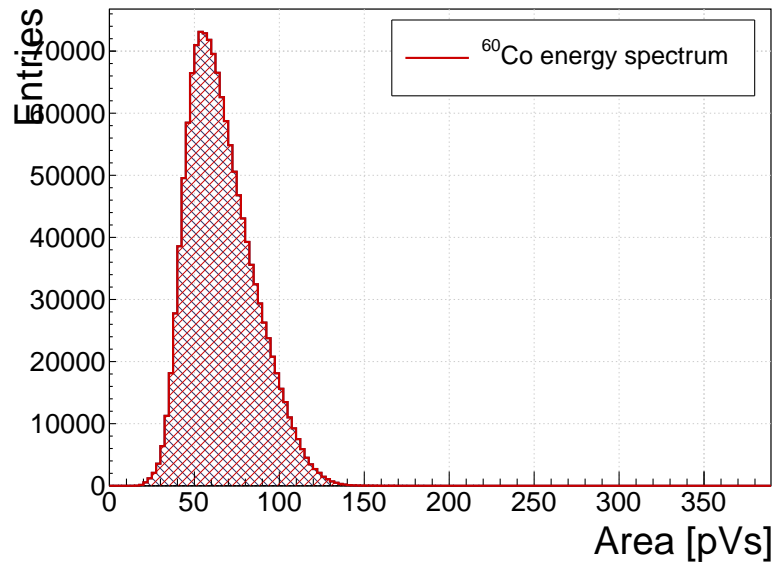


Figure 5.20:  $^{60}\text{Co}$  scatter plots.



(a)  $^{90}\text{Sr}$ .



(b)  $^{60}\text{Co}$ .

Figure 5.21: Energy distributions for  $\gamma$  and  $\beta$  particles.

## 5.10 Applications in neutron instrumentation

The real-time pulse shape analysis procedure can be applied to more complex systems. This section includes three applications where the PSA has been applied.

Semiconductor-based neutron detectors provide a compact technology for neutron detection. However, the cross section of a neutron with the diamond bulk is very low, since it only interacts with the core of the atom. Diamond is mainly used to detect charged particles and photons.

Research neutron reactors radiate a mix of particles, apart from neutrons also photons. The photons are considered a background radiation, concealing the neutron spectrum. When measured with diamond, the signal from neutrons is difficult to distinguish from the photon spectrum. In addition, low energy neutrons do not cause nuclear reactions in the bulk. All in all, the neutron measurements in a reactor present a challenge with diamond. However, by means of the PSA, the neutron signal can be discriminated from the photon background to some extent. The following two cases show how measurements of fast ( $n^+$ ) and thermal ( $n^-$ ) neutrons have been carried out by making use of the PSA.

Note the changing scale on the X axis in the figures.

### 5.10.1 Thermal neutron flux monitoring

Research neutron reactors like TRIGA MARK II [?] at Atominstitut [?] in Vienna are capable of emitting neutrons at a wide range of energies. The neutron flux is proportional to the current power of the reactor. It is therefore instrumental to monitor the neutron flux to make sure that the reactor operation is within the specified limits. However, the byproduct of the radioactive decays in the core is  $\gamma$  radiation, which has an energy range that overlaps with that of neutrons, making it difficult to measure the neutron flux. This is where PSA and diamond detectors come into play. This section describes the application of thermal neutron flux monitoring by means of the PSA.

Thermal neutrons do not interact with the diamond bulk due to their low kinetic energy (of the order of 0.012 eV). Hence a converter foil has to be added to produce second order effects. Incoming neutrons interact with the foil, producing a set of secondary particles. These can then be detected upon hitting the detector bulk. Common neutron interactions that are used in thermal neutron detection are  $^{10}\text{B}(n,\alpha)^7\text{Li}$  reaction and  $^6\text{Li}(n,\alpha)^3\text{H}$  reaction ( $\alpha$  stands for  $^4_2\text{He}$ , see equation 5.2). The focus in this section is on the latter. With a foil installed, there are several possibilities for neutrons to interact with the detector system. Each of these interactions ionises the diamond bulk in its own way, resulting in a specific shape of the current pulse. A neutron can: 1) interact with the foil, producing an  $\alpha$  and a  $^3\text{H}$ , 2) interact with a carbon atom in the lattice, producing an  $\alpha$  and a  $\gamma$  or even three  $\alpha$ . The thermal neutrons do not have enough kinetic energy to interact with the lattice, therefore the focus is on case (1). The equation for this reaction is the following:



The particles in the first case are produced outside the diamond and get stopped immediately upon hitting the sensor. The resulting pulses for both particles have a rectangular shape of the same width, because the carriers drift with the same speed in both cases. The difference is in the number of free carriers produced - the tritium creates more (proportional to the deposited energy), which in turn induces a higher pulse.

TRIGA MARK II neutron reactor emits large amounts of  $\gamma$  radiation in the energy range up to 3 MeV. This already affects the measurements of  $\alpha$  particles, the energy of which peaks at 2.05 MeV in the case of  $^6\text{Li}$  converter foil. However,  $\gamma$  background radiation can be suppressed by discriminating current pulses of photons from those induced by  $\alpha$  particles. This idea has already been implemented in offline analysis in [67, 68]. The results show that the background photons can be subtracted successfully. In order to make sure that every single incident thermal neutron has been accounted for, the algorithm has been ported to FPGA where it detects and analyses particles in real time.

#### **5.10.1.1 Measurements**

ROSY readout device with the implemented Pulse Shape Analysis was put to a test at Atominstut in Vienna. Their TRIGA neutron reactor is capable of delivering thermal neutrons with the energy 0.012 eV at a rate of  $10^3 \text{ n cm}^{-2} \text{ s}^{-1}$ , with a considerable  $\gamma$  background.

First, the device was calibrated using an unsealed monochromatic  $^{241}\text{Am}$  source with the emitted particle energy  $E_\alpha = 5.12\text{MeV}$  (taking into account the losses in the air). Then the diamond detector was exposed to the beam. Secondary reaction products ( $\alpha$  and  $^3\text{H}$  particles), created by neutrons hitting the converter foil, were detected by the diamond sensor, together with a significant photon background. Then the pulse identification algorithm was applied to discriminate between the reaction products and the photons.

The main parts of the detector are an sCVD diamond sensor sized  $4.7 \times 4.7 \text{ cm}^2$  and a  $1.8 \mu\text{m}$  thick LiF converter foil, both embedded in an RF-tight PCB. The diamond sensor is biased with a bias voltage of  $1 \text{ V}/\mu\text{m}$  and capacitively coupled to CIVIDEC's C2 40 dB wide bandwidth current preamplifier. A 5 m long BNC cable connects the preamplifier to CIVIDEC ROSY box. The detector assembly together with the preamplifier has to be placed in front of an exit hole of the reactor.

Note: this data set has been taken with an older version of the firmware, which only measured a limited number of pulse parameters.

#### **5.10.1.2 Results and discussion**

The data collected by the PSA show a high flux of photons, which covers a wide area range. The  $^3\text{He}$  peak is clearly visible and has almost no overlap with the photon cluster. The  $\alpha$  cluster has a much lower energy and is in the same energy range as the photons. However, if a FWHM parameter is observed, a distinction between the photons and the  $\alpha$  can be seen. By setting a qualifier to the right value, the photon background is cut away, leaving only

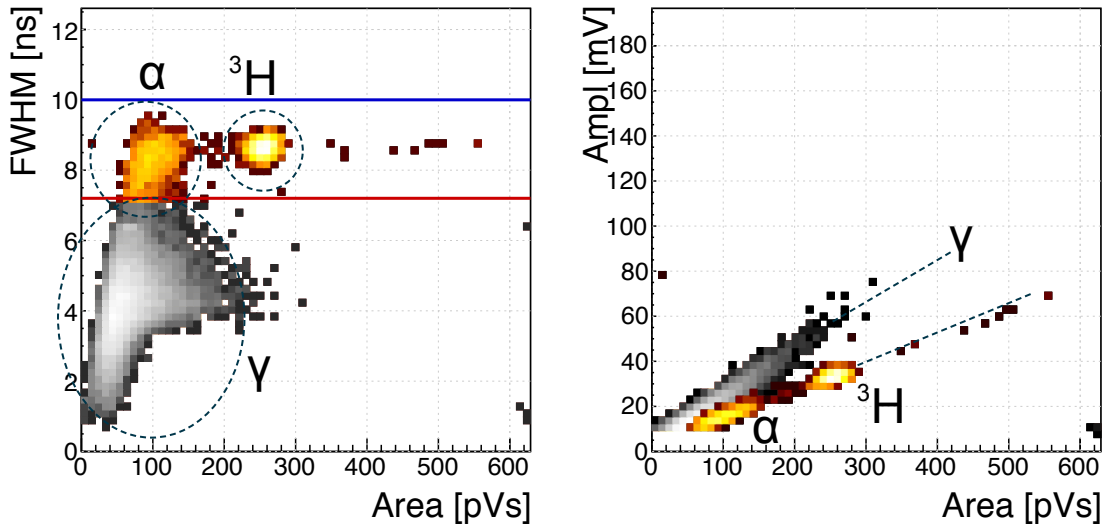
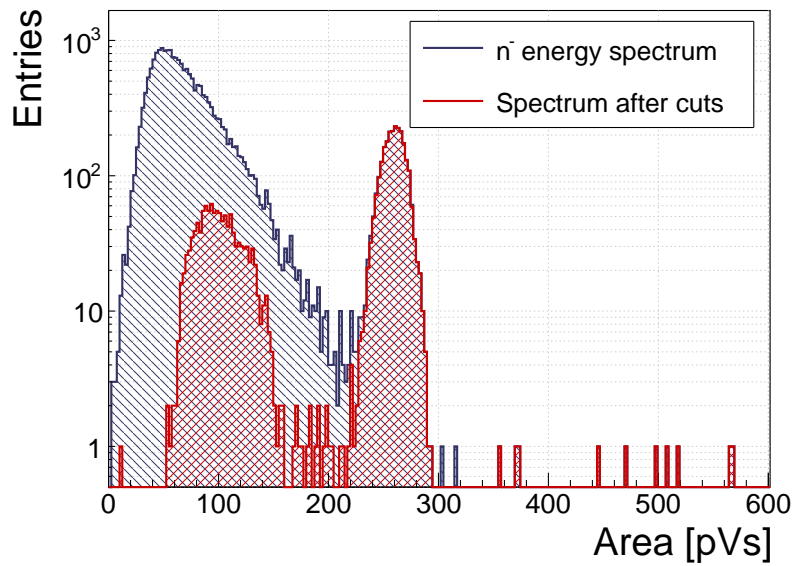


Figure 5.22: Thermal neutrons, photons. Qualifier: FWHM.


 Figure 5.23: Energy spectrum after applied qualifiers reveals the tritium and  $\alpha$  peak

the thermal neutron decay products in the data set, as shown in figure 5.22. The resulting one-dimensional area histogram before and after applied cuts is shown in figure 5.23. The blue distribution is the mixed field of background photons, tritium and  $\alpha$  particles. The latter are completely hidden in the  $\gamma$  energy distribution. After applied qualifiers the  $\alpha$  peak suddenly appears.

### 5.10.1.3 Conclusion

By applying the FWHM qualifier to the acquired data from the TRIGA neutron reactor, the  $\alpha$  and tritium particles can be identified and separated from the  $\gamma$  background. The resulting cleaned data can be used to correctly count the thermal neutrons detected by the diamond sensor.

### 5.10.2 Fusion power monitoring

Many research collaborations around the world are trying to develop a functional fusion reactor, which could provide a cleaner energy source. One of them is ITER [71], a research fusion reactor being built in France. The idea behind it is to harvest energy from the fusion of light atoms into a heavier one. For ITER the fuel chosen is a mixture of deuterium and tritium, which fuse into a helium atom at extremely high temperatures (plasma), emitting a highly energetic neutron as a byproduct. The equation is the following:



The  $\alpha$  particle immediately deposits its energy within the plasma. The neutron, due to its neutral charge, continues its way out of the system where it is stopped. The stopping power is converted into energy, which heats the water into steam, which in turn spins the turbines, generating electricity.

It is possible to monitor the activity of the reactor by measuring the flux of neutrons emitted. Neutron diagnostics such as neutron cameras, neutron spectrometers and neutron flux monitors therefore provide robust measurements of fusion power. A high  $\gamma$  background makes it difficult to accurately measure the neutron flux. This is a motivation to use a diamond based detector with a real-time PSA algorithm.

The neutrons emitted are 14 MeV mono-energetic fast neutrons. The most accurate and efficient way to detect them with a diamond detector is by means of a  $C_{12}(n,\alpha)$  reaction with a carbon atom in the ballistic centre [72]. In this region the positive and negative charge carriers created by  $\alpha$  that start drifting in the opposite directions need the same time to reach the opposite electrodes.

#### 5.10.2.1 Measurements

The  $^{239}\text{Pu Be}$  neutron source has been used to simulate the fusion reactor. It emits a mixed field of neutrons and photons with a wide range of energies. The neutrons are rarely detected with diamond – the interactions happen mostly in the electrodes on either side of the detector. The  $\alpha$  particles created by the interactions are detected by the diamond. Depending on the side of the interaction, the created pulse is either due to hole- or electron collection. These two interactions make the two distinct lines in the [area, FWHM] phase space at 9 ns and 6 ns, as shown in figure 5.24, top left plot.

A very interesting interaction point is the ballistic centre [?] of the diamond. A ballistic centre is the position from which it takes the holes and the electrons the same amount of

time to drift to the opposite electrodes. In this case the shortest possible pulse is created. Conversely, to conserve the collected charge and thus the pulse area, the pulse amplitude must be the highest at the ballistic centre. The entries in between are created by neutron interactions at random positions in the diamond, which produce pulses of various shapes.

### 5.10.2.2 Results and discussion

Coming back to the motivation, the most efficient way of counting the 14 MeV neutrons is through the measurement of the neutrons interacting in the ballistic centre [?]. To extract this type of interaction several qualifiers must be used. The first possibility is the FWHM set to 3–5 ns. However, this time the cuts on the [area, amplitude] and the [area, amplitude×base value] phase space are preferred. First, a minimum constant amplitude qualifier is set to 22 mV, as shown in figure 5.24, middle left plot. Then a linear amplitude qualifier is set such that only the pulses with the highest amplitude for every area value are taken. This ensures that the high pulses from the ballistic centre are chosen. Second, a maximum linear amplitude×base value qualifier is set such that only the pulses bearing the closest resemblance to a rectangle are chosen, as shown in figure 5.24, middle right plot. In this phase space the entries at the bottom of the distribution are bearing more resemblance to a rectangle whereas those at the top are more akin to triangles.

The resulting [area, FWHM] subfigure after applied qualifiers highlights the entries with a FWHM of 4 ns, which is the width of the pulses induced by neutrons interacting in the ballistic centre. This proves that these combined qualifiers indeed pinpoint these neutron interactions. The final one-dimensional area/energy distribution of the neutrons interacting in the ballistic centre is shown in figure 5.25.

The result could be further improved by further constraining the identification, e.g to define the minimum FWHM constant qualifier and the minimum slope constant qualifier.

### 5.10.2.3 Conclusion

By applying the appropriate qualifiers to the data, the neutron interactions in the ballistic centre can be identified.

## 5.10.3 Fast and thermal neutron monitoring

The CROCUS reactor at EPFL [73] is a research neutron reactor. The research group working on the reactor is interested in measuring neutrons with energies between 1–2 MeV, which is overlapping with the  $\gamma$  background energy range.

The highest output power of the CROCUS reactor is 100 W. Currently there are fission chambers that carry out the neutron counting, which is a measure of the activity of the reactor. The new goal is to measure both neutrons and photons, but separately. The pulse shape analysis is a good solution for this task. For this, a 400  $\mu\text{m}$  thick diamond detector with a specially designed casing was added to measure the activity. The LiF foil was added

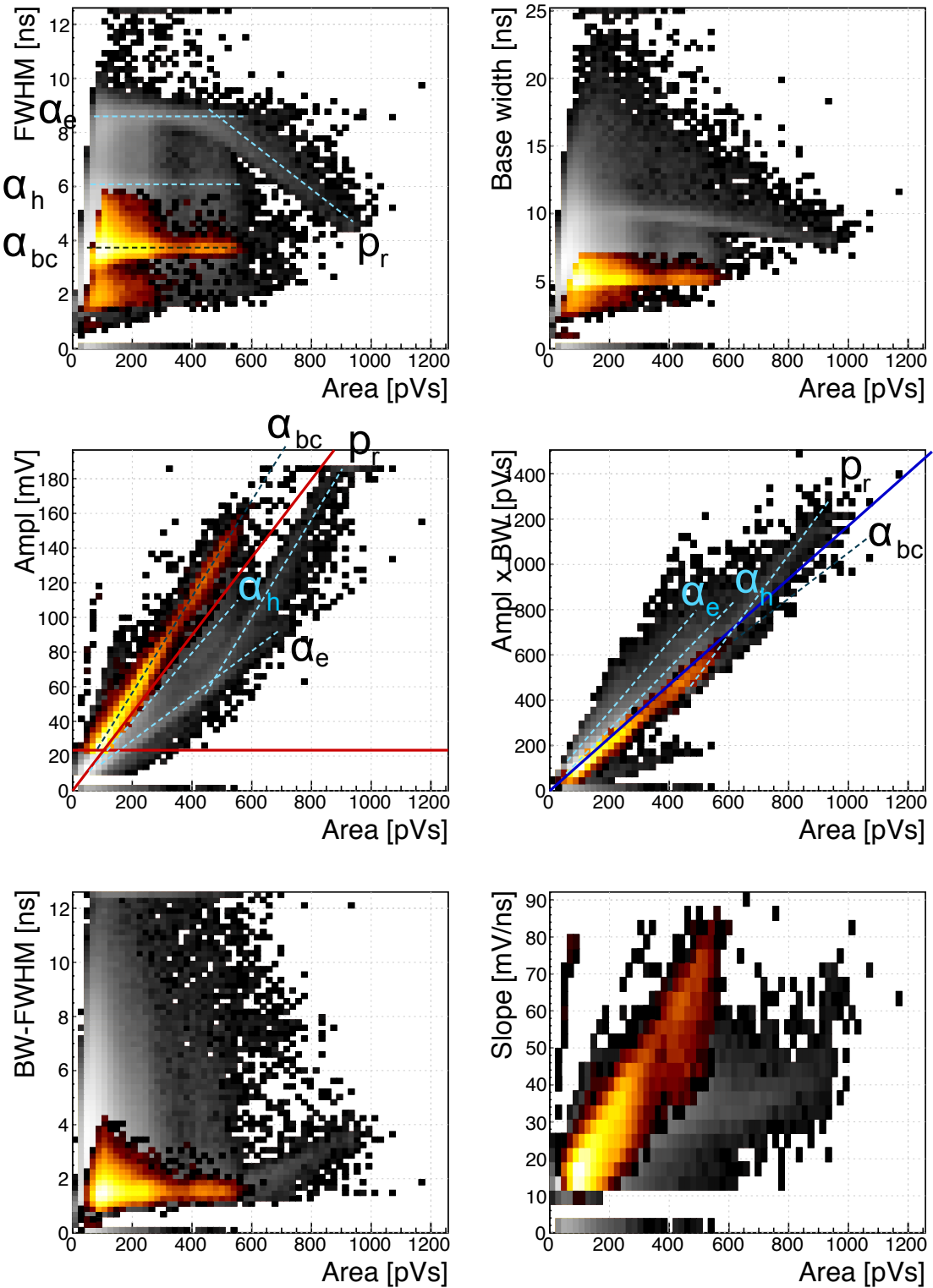


Figure 5.24:  $^{239}\text{Pu}$  Be. Qualifiers: BW-FWHM, FWHM, Form Factor

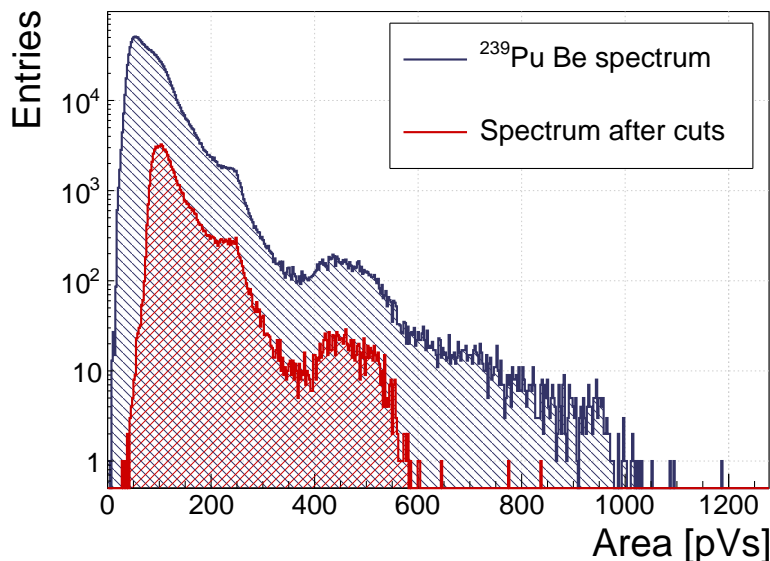


Figure 5.25:  $^{239}\text{Pu}$  Be, energy distribution of the neutrons interacting in the ballistic centre.

for conversion of thermal neutrons. The ROSY box with the integrated PSA routine was used for signal analysis.

#### 5.10.3.1 Measurements

At the highest reactor activity the system counts particles at a rate of  $\sim 1.5 \times 10^5 \text{ s}^{-1}$ . The results from a test run at 10 W output power are shown in figure 5.26. The data include a mixed field consisting of fast neutrons, photons and of  $\alpha$  and  $^3\text{H}$  particles as products of thermal neutron decay in the LiF foil in front of the detector. The energy deposited in the diamond is not as high as that from the  $^{239}\text{Pu}$  Be source. In addition, the analog noise during this measurement is higher than in the previous application. These conditions combined make particle identification at CROCUS a challenging task.

#### 5.10.3.2 Results and discussion

The aim of this exercise is to identify both thermal and fast neutrons. For this the main qualifier used is the Form Factor - the linear line in the [area, amplitude  $\times$  base value] phase space. Additional FWHM, FWHM-BW and slope constant qualifiers are used to clean the outlying entries. The resulting accepted entries in figure 5.26 have the distinctive three-line fast neutron signature in the [area, FWHM] subfigure with two superimposed islands by the  $\alpha$  and  $^3\text{H}$  cluster produced by thermal neutrons in the LiF foil. The  $\gamma$  background is sufficiently suppressed. The resulting one-dimensional histogram of the area/energy distribution is shown in figure 5.27.

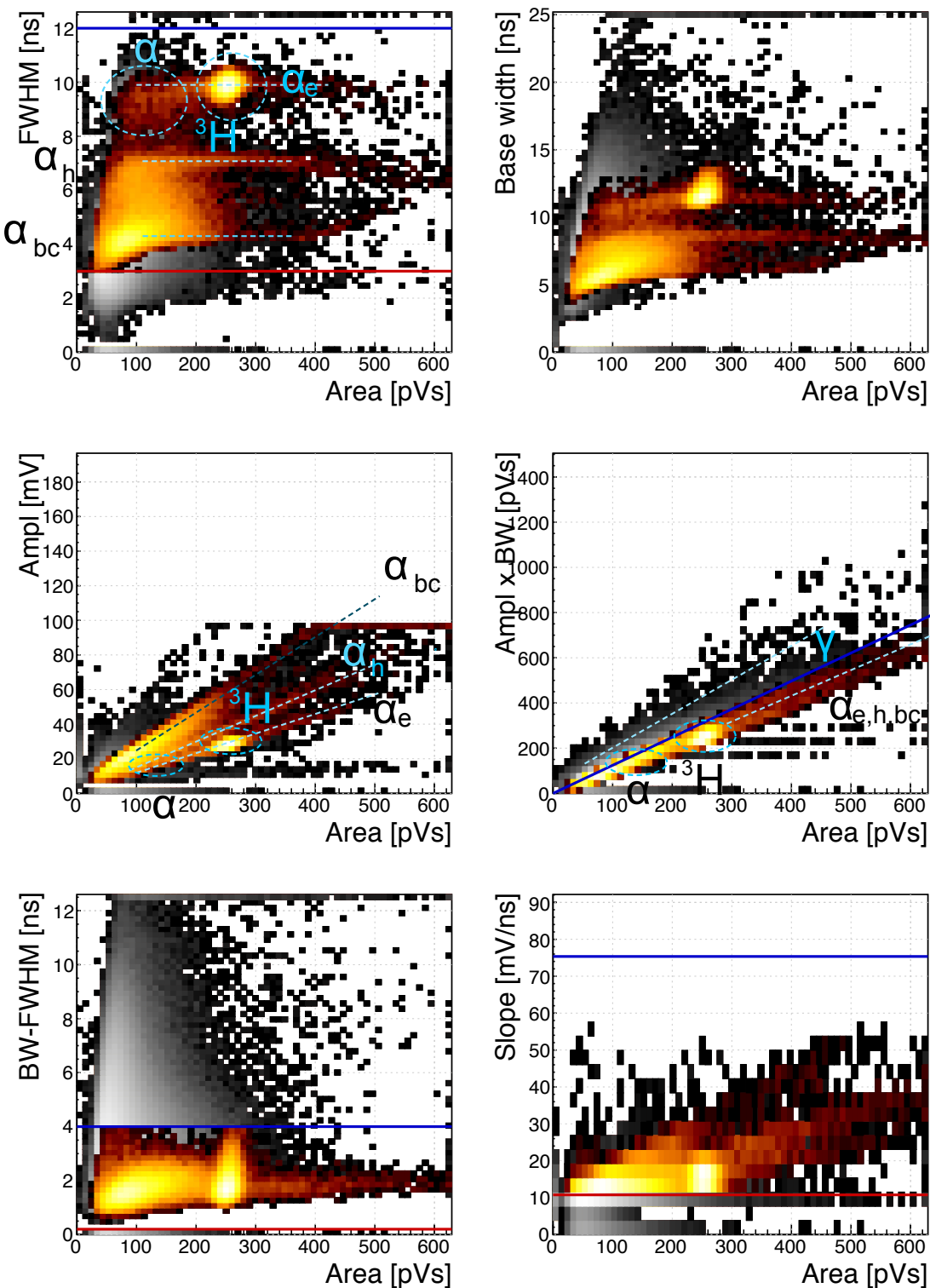


Figure 5.26: Fast neutrons, thermal neutrons, photons. Qualifiers: BW-FWHM, FWHM, Form factor, Slope.

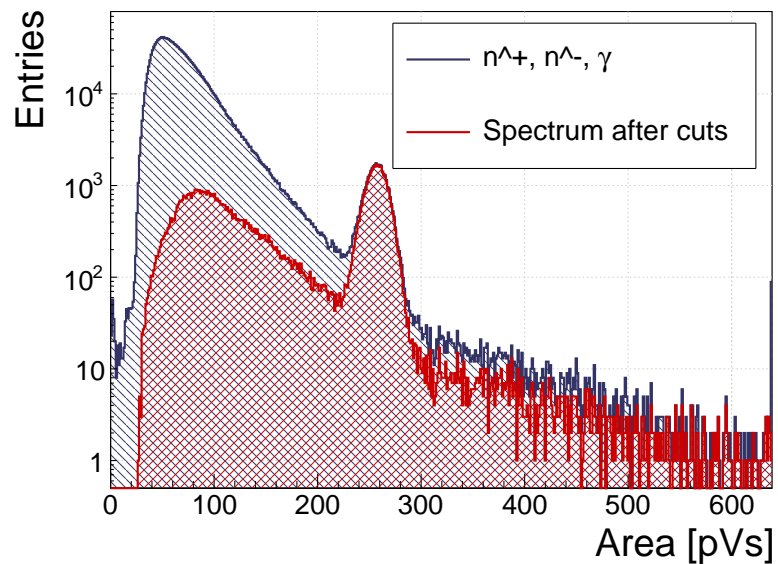


Figure 5.27: Energy spectrum in CROCUS before and after applied qualifiers

#### 5.10.3.3 Conclusion

By applying the Form Factor qualifier both fast and thermal neutrons can be identified, suppressing the  $\gamma$  background.

## **5.11 Conclusion**

This chapter describes a system that can identify the type of radiation in real time. The system is implemented on an FPGA in a CIVIDEC ROSY box and is used with diamond detectors. The signal from the diamond sensor is read in and analysed in the firmware. First the shape of the pulse is parametrised. Then the logic determines the type of particle according to the user defined cuts. Finally the parameters are written into a histogram, which is read out by the user. The firmware is designed to carry out the pulse shape analysis of a single pulse in  $\sim 200$  ns, yielding a maximum pulse rate of  $5 \times 10^6$  particles per second. The rate as well as the linearity the measurement stability with respect to noise have been verified using a pulse generator. Then several radioactive sources were used to calibrate the device. Finally the system has been set up in two neutron reactors to test the operation in a mixed field containing thermal neutrons, fast neutrons and photons. The identification can be optimised using a combination of qualifiers to achieve the desired effect.



# Bibliography

- [1] S. F. Novaes. *Standard model: An Introduction*. In *Particles and fields. Proceedings, 10th Jorge Andre Swieca Summer School, Sao Paulo, Brazil, February 6-12, 1999*, 1999.
- [2] Daniel Dominguez. *Standard Model. Le modele standard*. General Photo, Mar 2015.
- [3] E Rossi. *Measurements of the properties of the Higgs-like boson in the four leptons decay channel with the ATLAS detector using  $25\text{fb}^{-1}$  of proton-proton collision data*. *Nuovo Cimento C*, 037(01):217–221. 5 p, 2014.
- [4] European Centre for Nuclear Research, CERN. <http://home.cern>.
- [5] E Regenstreif. *The CERN proton synchrotron, 1. Ned. T. Natuurk.*, 25:117–132, 1959.
- [6] W P C Mills. *The present performance of the SPS*. *IEEE Trans. Nucl. Sci.*, 26(CERN-SPS-AOP-79-9):3176–3178. 3 p, Mar 1979.
- [7] Atominstutut, Technical University of Vienna, Austria. <http://ati.tuwien.ac.at/startpage/EN/>.
- [8] TRIGA MARK II neutron reactor. <http://ati.tuwien.ac.at/reactor/EN/>.
- [9] General Atomics. *View of the TRIGA reactor*. 2015.
- [10] Neutron Time-of-flight experiment. <https://ntof-exp.web.cern.ch/ntof-exp/>.
- [11] Maximilien Brice. *View of the nTOF detector*. Oct 2010.
- [12] Maximilien Brice. *LHC tunnel*. Jan 2011.
- [13] W Herr, B J Holzer, and B Muratori. *Design and Principles of Synchrotrons and Circular Colliders: Concept of Luminosity*. *Landolt-Bornstein*, 21C:6.4–1 – 6.4–7, 2013.
- [14] I Bejar Alonso and L Rossi. *HiLumi LHC Technical Design Report: Deliverable: D1.10*. Technical Report CERN-ACC-2015-0140, CERN, Geneva, Nov 2015.
- [15] Peter Jenni. *The experiments: ATLAS*. page 16 p, 2009.
- [16] Joao Pequenao. *Computer generated image of the whole ATLAS detector*. Mar 2008.

## BIBLIOGRAPHY

---

- [17] E. A. Ekimov, V. A. Sidorov, E. D. Bauer, N. N. Mel'nik, N. J. Curro, J. D. Thompson, and S. M. Stishov. *Superconductivity in diamond*. *Nature*, 428(6982):542–545, 04 2004.
- [18] 1951 Park, Jong-Hee, 1955 Sudarshan, T. S., and Inc ebrary. Chemical vapor deposition. Materials Park, Ohio : ASM International, 2001. Includes bibliographical references.
- [19] CIVIDEC Instrumentation GmbH. *sCVD diamond sensor*. <http://www.cividec.at>, 2015.
- [20] Heinz Pernegger. *The Pixel Detector of the ATLAS Experiment for LHC Run-2*. Technical Report ATL-INDET-PROC-2015-001, CERN, Geneva, Feb 2015.
- [21] Claudia Marcelloni De Oliveira. *IBL installation into the inner detector of the ATLAS Experiment side C*. General Photo, May 2014.
- [22] *Bremsstrahlung*. 2016.
- [23] Yoshihiko Hatano, Yosuke Katsumura, and A. Mozumder. Charged Particle and Photon Interactions with Matter: Recent Advances, Applications, and Interfaces. CRC Press, 2010.
- [24] S. Sze and K. N. Kwok. Physics of Semiconductor Devices, 3rd ed. Wiley, Hoboken, NJ, 2007.
- [25] W. Blum, W. Riegler, and L. Rolandi. Particle Detection with Drift Chambers, volume 2 of 2. Springer-Verlag, Berlin Heidelberg, 2008.
- [26] W. Shockley. *Currents to Conductors Induced by a Moving Point Charge*. *Journal of applied Physics*, 9:635, 1938.
- [27] S. Ramo. *Currents Induced by Electron Motion*. *Proceedings of the IRE*, 27:584–585, 1939.
- [28] Hendrik Jansen, Norbert Wermes, and Heinz Pernegger. Chemical Vapour Deposition Diamond - Charge Carrier Movement at Low Temperatures and Use in Time-Critical Applications. PhD thesis, Bonn U., Sep 2013. Presented 10 Dec 2013.
- [29] Hendrik Jansen, Daniel Dobos, Thomas Eisel, Heinz Pernegger, Vladimir Eremin, and Norbert Wermes. *Temperature dependence of charge carrier mobility in single-crystal chemical vapour deposition diamond*. *Journal of Applied Physics*, 113(17), 2013.
- [30] Z. Li and H. Kraner. *Modeling and simulation of charge collection properties for neutron irradiated silicon detectors*. *Nuclear Physics B - Proceedings Supplements* 32, (32):398–409, 1993.

## BIBLIOGRAPHY

---

- [31] Peter Sigmund. Particle Penetration and Radiation Effects Volume 2 - General Aspects and Stopping of Swift Point Charges, volume 151 of *Springer Series in Solid-State Sciences*. Springer-Verlag Berlin Heidelberg, 2006.
- [32] U. Fano. *Ionization Yield of Radiations. II. The Fluctuations of the Number of Ions*. *Physical Review*, 72:26–29, July 1947.
- [33] R. C. Alig, S. Bloom, and C. W. Struck. *Scattering by ionization and phonon emission in semiconductors*. 22:5565–5582, December 1980.
- [34] Claude A. Klein. *Radiation-Induced Energy Levels in Silicon*. *Journal of Applied Physics*, 30(8):1222–1231, 1959.
- [35] Marco Marinelli, E. Milani, M. E. Morgada, G. Pucella, G. Rodriguez, A. Tucciarone, G. Verona-Rinati, M. Angelone, and M. Pillon. *Thermal detrapping analysis of pumping-related defects in diamond*. *Applied Physics Letters*, 83(18):3707–3709, 2003.
- [36] M. Huhtinen. *Simulation of non-ionising energy loss and defect formation in silicon*. *Nuclear Instruments and Methods in Physics Research A*, 491:194–215, September 2002.
- [37] Moritz Guthoff, Wim de Boer, and Steffen Mller. *Simulation of beam induced lattice defects of diamond detectors using {FLUKA}* . *Nuclear Instruments and Methods in Physics Research Section A: Accelerators, Spectrometers, Detectors and Associated Equipment*, 735:223 – 228, 2014.
- [38] Determination of operational dose equivalent quantities for neutrons. ICRU, Washington, DC, 2001.
- [39] RD42 collaboration. <http://rd42.web.cern.ch/rd42/>.
- [40] M. Mikuž. *Diamond sensors for high energy radiation and particle detection*. TIPP, 2011.
- [41] J. L. Yarnell, J. L. Warren, and R. G. Wenzel. *Lattice Vibrations in Diamond*. *Phys. Rev. Lett.*, 13:13–15, Jul 1964.
- [42] W. Y. Liang. *Excitons*. *Physics Education*, 5:226–228, July 1970.
- [43] J. B. Johnson. *Thermal Agitation of Electricity in Conductors*. *Phys. Rev.*, 32:97–109, Jul 1928.
- [44] H. Nyquist. *Thermal Agitation of Electric Charge in Conductors*. *Phys. Rev.*, 32:110–113, Jul 1928.
- [45] Xilinx Virtex 5 FPGA. <http://www.hdl.co.jp/XCM-109/top.560.jpg>.
- [46] M. Garcia-Sciveres. *ATLAS Experiment Pixel Detector Upgrades*. 2011.

## BIBLIOGRAPHY

---

- [47] *Element Six*. <http://www.e6.com>.
- [48] *IHa Technologies Pte. Ltd.* <https://www.2atechnologies.com>.
- [49] M. Červ, P. Sarin, H. Pernegger, P. Vageeswaran, and E. Griesmayer. *Diamond detector for beam profile monitoring in COMET experiment at J-PARC*. *Journal of Instrumentation*, 10(06):C06016, 2015.
- [50] *DRS4*. <https://www.psi.ch/drs/evaluation-board>.
- [51] *Paul Scherrer Institute*. <https://www.psi.ch/>.
- [52] Giorgio Brianti. SPS North Experimental Area. Technical Report CERN-SPSC-T-73-8. LabII-EA-Note-73-4, CERN, Geneva, 1973.
- [53] H. Bethe and J. Ashkin. *Experimental Nuclear Physics*, ed. E. Segre, page 253, 1953.
- [54] V. Sarin. Comprehensive Hard Materials. Elsevier Science, 2014. p. 411.
- [55] E. Griesmayer and B. Dehning. *Diamonds for Beam Instrumentation. Physics Procedia*, 37:1997 – 2004, 2012. Proceedings of the 2nd International Conference on Technology and Instrumentation in Particle Physics (TIPP 2011).
- [56] Gregor Kramberger, V. Cindro, A. Gorisek, I. Mandic, M. Mikuz, and M. Zavrtanik. *Effects of bias voltage during priming on operation of diamond detectors*. *PoS*, Vertex2012:013, 2013.
- [57] Matevž Červ. *The ATLAS Diamond Beam Monitor*. Technical Report ATL-INDET-PROC-2013-021, CERN, Geneva, Nov 2013.
- [58] A Gorišek, V Cindro, I Dolenc, H Frais-Klbl, E Griesmayer, H Kagan, S Korpar, G Kramberger, I Mandic, M Meyer, M Mikuz, H Pernegger, S Smith, W Trischuk, P Weilhammer, and M Zavrtanik. *ATLAS diamond Beam Condition Monitor*. *Nucl. Instrum. Methods Phys. Res., A*, 572(1):67–69, 2007.
- [59] *Measurement of the Rate of Collisions from Satellite Bunches for the April-May 2010 LHC Luminosity Calibration*. Technical Report ATLAS-CONF-2010-102, CERN, Geneva, Dec 2010.
- [60] *CiS Forschungsinstitut fuer Mikrosensorik GmbH*. <http://www.cismst.org/>.
- [61] J et al. Albert. *Prototype ATLAS IBL Modules using the FE-I4A Front-End Readout Chip*. *J. Instrum.*, 7(arXiv:1209.1906):P11010. 45 p, Sep 2012. Comments: 45 pages, 30 figures, submitted to JINST.
- [62] Fabian Huegging. *The ATLAS Pixel Insertable B-Layer (IBL)*. *Nucl. Instrum. Methods Phys. Res., A*, 650(arXiv:1012.2742):45–49. 7 p, Dec 2010. Comments: 7 pages, 5 figures, 4 tables, accepted by Nuclear Instruments and Methods A for publication.

## BIBLIOGRAPHY

---

- [63] Richard Claus. *A New ATLAS Muon CSC Readout System with System on Chip Technology on ATCA Platform*. Jun 2015.
- [64] S Mueller, W deBoer, M Schneider, A Sabellek, M Schmanau, C Ruehle, T Schneider, and R Hall-Wilton. *Study of leakage currents in pCVD diamonds as function of the magnetic field*. *Phys. Status Solidi, A*, 206(arXiv:0905.0403):2091–2097. 6 p, May 2009. Comments: 6 pages, 16 figures, poster at Hasselt Diamond Workshop, Mar 2009.
- [65] Garrin McGoldrick, Matevž Červ, and Andrej Gorišek. *Synchronized analysis of test-beam data with the Judith software*. *Nucl. Instrum. Methods Phys. Res., A*, 765:140–145, 2014.
- [66] *EUDET ACONITE telescope*. <https://telescopes.desy.de>.
- [67] P. Kavrigin, P. Finocchiaro, E. Griesmayer, E. Jericha, A. Pappalardo, and C. Weiss. *Pulse-shape analysis for gamma background rejection in thermal neutron radiation using CVD diamond detectors*. *Nuclear Instruments and Methods in Physics Research A*, (795), 2015.
- [68] E. Griesmayer, R. Bergmann, H. Böck, M. Cagnazzo, P. Kavrigin, B. Morgenbesser, and M. Villa. *A Novel Neutron Flux Monitor Based On Diamond Detectors at the Vienna TRIGA Mark II Reactor*. submitted to the proceedings of ICRR 2015, 2015.
- [69] C. Weiss, H. Frais-Kölbl, E. Griesmayer, and P. Kavrigin. *Ionization signals of diamond detectors in fast neutron fields*. publication in preparation, 2016.
- [70] C. Weiss. A CVD diamond detector for  $(n,\alpha)$  cross-section measurements. PhD thesis, TU Wien, Vienna, 2014.
- [71] *ITER fusion reactor*. <https://www.iter.org/>.
- [72] P. Kavrigin, E. Griesmayer, F. Belloni, A.J.M. Plompen, P. Schillebeeckx, and C. Weiss.  *$^{13}C(n,\alpha_0)^{10}Be$  cross section measurement with sCVD diamond detector*. submitted to EPJA, 2016.
- [73] *CROCUS neutron reactor*. <http://lrs.epfl.ch/page-55655-en.html>.